



***FIELD EMISSION OF THERMALLY GROWN CARBON NANOSTRUCTURES ON  
SILICON CARBIDE***

THESIS

Jonathon M. Campbell, Captain, USAF

AFIT/GE/ENG/12-06

**DEPARTMENT OF THE AIR FORCE  
AIR UNIVERSITY**

**AIR FORCE INSTITUTE OF TECHNOLOGY**

**Wright-Patterson Air Force Base, Ohio**

APPROVED FOR PUBLIC RELEASE; DISTRIBUTION UNLIMITED

The views expressed in this thesis are those of the author and do not reflect the official policy or position of the United States Air Force, Department of Defense, or the United States Government. This material is declared a work of the U.S. Government and is not subject to copyright protection in the United States.

AFIT/GE/ENG/12-06

***FIELD EMISSION OF THERMALLY GROWN CARBON NANOSTRUCTURES ON  
SILICON CARBIDE***

THESIS

Presented to the Faculty

Department of Electrical and Computer Engineering

Graduate School of Engineering and Management

Air Force Institute of Technology

Air University

Air Education and Training Command

In Partial Fulfillment of the Requirements for the  
Degree of Master of Science in Electrical Engineering

Jonathon M. Campbell, BS

Captain, USAF

March 2012

APPROVED FOR PUBLIC RELEASE; DISTRIBUTION UNLIMITED

AFIT/GE/ENG/12-06

***FIELD EMISSION OF THERMALLY GROWN CARBON NANOSTRUCTURES ON  
SILICON CARBIDE***

Jonathon M. Campbell, BS

Captain, USAF

Approved:

/signed/

\_\_\_\_\_  
Michael C. Pochet, Maj, USAF (Chairman)

28 Feb 2012

\_\_\_\_\_  
Date

/signed/

\_\_\_\_\_  
Dr. John J. Boeckl (Member)

28 Feb 2012

\_\_\_\_\_  
Date

/signed/

\_\_\_\_\_  
Dr. Ronald A. Coutu, Jr. (Member)

28 Feb 2012

\_\_\_\_\_  
Date

### **Abstract**

CNT are known to be excellent field emitter due to their unique physical and electrical properties. Because of their semi-metallic nature, CNT do not suffer the thermal runaway found in metallic emitters, and their near one-dimension shape make them an ideal emission sources.

CNT growth by thermal decomposition of silicon carbide does not utilize a catalyst, therefore relatively defect free. One drawback to this method, however is that the CNT grow in a very dense carpet. This very dense CNT carpet comes under the affect of field emission screening effects which dampen the field emission. In this thesis, silicon carbide samples are patterned to create elevated emission sites in an attempt to minimize the field emission screening effect. Patterning is accomplished by using standard photolithography methods to implement a masking nickel layer on the silicon carbide. Pillars are created by etching the unmasked area of the silicon carbide in a reactive ion etcher. CNT growth is accomplished in a thermal furnace of varying times based on the selected face of the silicon carbide. Field emission testing to obtain turn-on voltage, field enhancement factor, and current densities is accomplished using a standard vacuum tube diode test configuration, while selected samples are subjected to stability testing over varying times.

Although the samples tested did not conclusively demonstrate improved field emission characteristics when compared to values found in the literature for other bundled or pillared CNT, the data collected from similar samples in this work shows that

a patterned CNT film can outperform a non-patterned film. From the measured CNT data, the lowest turn-on electric field is found to be  $2.5 \text{ V}/\mu\text{m}$  (taken at  $1 \mu\text{A}/\text{cm}^2$ ), and the highest field enhancement factor is of 8007. The variability in performance between samples can be attributed to differences in the emission surfaces as the result of: sample processing; the presence of impurities or amorphous carbon; and damage to the emitter surface due to microarcing.

## **Acknowledgments**

I would like to express my sincere appreciation to my faculty advisor, Major Michael Pochet for his guidance and support throughout the course of this thesis effort. I would also like to thank Dr. Ron Coutu and Dr. John Boeckl for their insight. Thanks is also given to the AFIT Cleanroom technicians Mr. Rich Johnston and Mr. Tom Stevenson for their help with the getting my samples prepped. I am also grateful to Major Nate Glauvitz, for his random thoughts on CNTs and letting me pick his brain about what I was doing.

Finally, I would like to thank my wife who has shown 1/0 patience with me during the last 2 years.

Jonathon M. Campbell

## Table of Contents

	Page
Abstract .....	iv
Table of Contents .....	vii
List of Figures .....	xi
List of Tables .....	xxi
Chapter I: Introduction.....	1
1.1. General Issue .....	1
1.2. Summary of Current Knowledge.....	4
1.2.1. Carbon Nanotubes.....	4
1.2.2. Field Electron Emission from CNTs.....	5
1.3. Research Problem.....	6
1.4. Assumptions and Limitations.....	7
1.5. Approach and Methods.....	7
1.6. Thesis Structure .....	7
Chapter II: Literature & Theory Review .....	8
2.1. Chapter Overview.....	8
2.2. CNT Background.....	8
2.2.1. CNT Structure.....	8
2.2.2. Properties .....	10
2.3. CNT Growth by Thermal Decomposition.....	12
2.3.1. Formation of Carbon Nanocaps .....	14
2.3.2. Effects of CNT Growth Parameter .....	20
2.4. Field Emission Process.....	22
2.4.1. Fowler-Nordheim Field Emission.....	23

2.4.2. Field Enhancement Factor .....	26
2.4.3. Deviation for Nanoscale Tips .....	28
2.4.4. CNT Field Emission and Issues .....	29
2.4.4.1. Early Field Emission Tests.....	30
2.4.4.2. Field Emission Screening.....	35
2.5. Patterning of SiC .....	45
2.5.1. Silicon Carbide Properties .....	45
2.5.2. Silicon Carbide Etching .....	46
Chapter III: Process Development and Experimental Methodology .....	48
3.1. Pre-CNT Growth Sample Preparation.....	48
3.1.1. Pre-RIE Process .....	48
3.1.2. RIE Process.....	50
3.2. CNT Growth Procedures .....	58
3.3. Field Emission Testing.....	62
3.3.1. Data Collection .....	62
3.3.2. Data Processing.....	65
3.4. Chapter Summary.....	67
Chapter IV: Results and Analysis .....	68
4.1. Introduction .....	68
4.2. Sample Set Surface and Process Analysis.....	68
4.2.1. Sample Set J.....	68
4.2.2. Sample Set K.....	70
4.2.3. Sample Set L.....	73
4.2.4. Sample Set H.....	74

4.3. SiC Decomposition of Samples.....	77
4.3.1. Sample Set J.....	77
4.3.2. Sample Set K.....	80
4.3.3. Sample Set L.....	82
4.3.4. Sample Set H.....	84
4.4. Field Emission Results and Analysis .....	86
4.4.1. Sample Set J – Field Emission.....	87
4.4.1.1. Sample J1 – Field Emission .....	87
4.4.1.2. Sample J2 – Field Emission .....	91
4.4.2. Sample Set K – Field Emission .....	97
4.4.2.1. Sample K1 – Field Emission .....	98
4.4.2.2. Sample K2 – Field Emission.....	102
4.4.2.3. Sample K3 – Field Emission.....	106
4.4.3. Sample Set L – Field Emission.....	109
4.4.3.1. Sample L1 – Field Emission .....	109
4.4.3.2. Sample L2 – Field Emission .....	113
4.4.4. Sample Set H – Field Emission .....	117
4.4.4.1. Sample H1: All RIE Surface – Field Emission .....	117
4.4.4.2. Sample H2: Patterned Surface – Field Emission.....	120
4.4.4.3. Sample H3: Patterned Surface – Field Emission.....	123
4.4.4.4. Sample H4: Unpatterned Surface – Field Emission .....	126
4.4.5. Field Emission Results Comparison.....	129
4.4.5.1. Sample Sets J through L.....	129

4.4.5.2. Sample Set H Comparisons .....	130
4.4.6. Field Emission Stability Results .....	132
4.5. Chapter Summary .....	134
Chapter V: Conclusions and Recommendations.....	136
5.1. Thesis Summary .....	136
5.2. Recommendation for Further Work .....	138
Appendices.....	140
Appendix A: CNT Synthesis Processes .....	140
Appendix B: Silicon Carbide Structure .....	147
Appendix C: SiC Decomposition Procedure.....	150
Appendix D: Field Emission Chamber Procedures.....	152
References.....	154

## List of Figures

	Page
Figure 1 – Diagram of Utsumi’s ideal cathode configuration with a figure a merit defined as $f_i = (I_i/I_0)*(V_i/V_0)^{-1}*(L_i/L_0)^{-1}$ where $I_i$ , $V_i$ , and $L_i$ are emission current, gate voltage, and linear device dimension of the $i$ th field emitter and $I_0$ , $V_0$ , and $L_0$ are the parameters from an ideal field emitter. [8] .....	3
Figure 2 – TEM images of Iijima's CNT discovery showing the structure of single-walled and multi-walled CNTs [9].....	4
Figure 3 – Field screening effect for emitters (left-to-right) single emitter, one-to-one emitter spacing, and close packed emitters [12].....	6
Figure 4 – CNTs are derived from rolled up graphene sheet cut along one of three axis creating either (n,n) armchair, (n,0) zigzag, or a general chiral CNTs. [13] .....	9
Figure 5 – Examples of (top) armchair (n,n) = (5,5), (middle) zigzag (n,m) = (9,0), and (bottom) Chiral (n,m) = (10,5) [14].....	9
Figure 6 – One dimensional density of states for different nanotube configurations. The armchair nanotube (5, 5) is metallic due to symmetry; the chiral nanotube (7, 1) displays a tiny gap due to curvature effects, but acts metallic at room temperature; and the zigzag nanotube (8, 0) is a large-gap semiconductor. [16] .....	11
Figure 7 – TEM image of CNT growth on Si-face of SiC, top layer is a platinum coating used to protect the CNT layer during preparation [19].....	12
Figure 8 – Flow diagram of CNT growth using thermal decomposition showing CNTs densely packed CNTs growing into the surface as time increases .....	13
Figure 9 – Schematic showing the side(a) and top(b) view of C-face SiC, the dangling bonds at the top of the side view form the basis for the zigzag CNT (c)[22] .....	14

Figure 10 –	Carbon nanocaps formation model proposed by Wantabee <i>et al.</i> . The model show (a) the formation of amorphous carbon on the surface, (b) crystallization of carbon into a graphite sheet, (c) lifting of the graphite sheet to form nanocaps, (d) growth of nanocaps by a movement of heptagons in opposite direction of growth, (e) formation of additional graphite layers with increased temperature, and (f) beginning formation of MWCNT [23].....	15
Figure 11 –	Comparison of XPS measurements (a) before heating and (b) after heating. The intensity ratio is shown as a function of temperature with the intensity of carbon increasing as the sample is heated [22].....	16
Figure 12 –	(a) Observations of nanocap formation on SiC using STM; (b) profile measurements of nanocaps showing heights of 1-3 nm and diameters of 3-5 nm [25].....	17
Figure 13 –	Observation by Bang <i>et al</i> of pentagon and hexagon formations in the nanocaps showing that the nanocaps have crystallized before forming on the surface [25].....	18
Figure 14 –	Nanocap formation proposed by Maruyama <i>et al.</i> (a) accumulation of carbon nanoclusters; (b) clustering of nanoparticles; (c) coalescence of nanoparticles; (d) crystallization of nanoclusters utilizing dangling bonds; (e) crystallization into beginning of nanocap; (f) at 1250 °C nanocaps form [22].....	19
Figure 15 –	Model of CNT growth proposed by Kusunoki <i>et al</i> , showing CNT growing into the surface by the diffusion of carbon atoms within a distance of a CNTs cross-sectional radius [24].....	19
Figure 16 –	Oxygen pressure phase diagram, showing regions 1 and 2 as the active oxidation regions and region 3 as the passive oxidation region [27].....	21
Figure 17 –	IV curve of a field emitter. The linear F-N plot, in the inset, indicates the electron emission is from field emission .....	26
Figure 18 –	Comparison of tip features and resulting field enhancement factor with respect to the emitter’s aspect ratio [37].....	27
Figure 19 –	Comparison between Fursey <i>et al</i> ’s numerical solution to the F-N equation compared to the traditional F-N criteria for emitter tip radii of 40 and 80 Å [39].....	29

Figure 20 –	de Heer <i>et al</i> electron source consisting of a purified CNT film formed by an arc discharge method and pressed on a PTFE sheet, and a perforated mica sheet bonded to the CNT film and covered with a copper grid [41].....	30
Figure 21 –	IV curve and F-N plot of data collected by de Heer from the setup described by Figure 20.....	31
Figure 22 –	(a) SWCNTs deposited on copper or brass platelets at a density of $\sim 10^8 \text{ cm}^{-2}$ ; (b) Field emission measurement setup [42] .....	32
Figure 23 –	IV curves and F-N plot from emission testing of SWNT films by Bonard <i>et al</i> [42] .....	32
Figure 24 –	(a) MWNTs attached to a 250 nm gold tip, (b) MWNTs deposited on copper plate, (c) measurement setup of single MWNT, and (d) setup for MWNT film [43] .....	33
Figure 25 –	Experimental IV curves for (a) single MWNT and (b) MWNT films, insets show F-N plot [43] .....	34
Figure 26 –	SEM image of Nilsson <i>et al</i> patterned CNTs, (inset) field emission intensity shown on a phosphor screen [44].....	36
Figure 27 –	FE scans of different density of CNTs showing medium density with the best results [44] .....	36
Figure 28 –	Electrostatic calculations on inter-emitter spacing showing the effects of spacing on current density and field enhancement [44].....	37
Figure 29 –	(a) and (b) Current density and F-N plots for various CNT heights and diameters of 38 and 19 nm; (c) Field enhancement factors against a variable heights of CNTs at constant spacing of 104 and 65 nm [45].....	38
Figure 30 –	Simulated current density against the intertube density for varying applied fields and SWCNT lengths: (a) $L = 0.75 \text{ }\mu\text{m}$ , $F_{\text{app}} = 12.0 \text{ V}/\mu\text{m}$ ; (b) $L = 1.00 \text{ }\mu\text{m}$ , $F_{\text{app}} = 12.0 \text{ V}/\mu\text{m}$ ; and (c) $L = 1.00 \text{ }\mu\text{m}$ , $F_{\text{app}} = 10.0 \text{ V}/\mu\text{m}$ [12] .....	40
Figure 31 –	Using a defined screening factor $\alpha$ , (a) and (b) show that variations in $L$ , $d$ , and $F_{\text{appl}}$ have little effect on the curves and hence $\alpha$ .....	41
Figure 32 –	Basic 2D model for Smith <i>et al</i> simulations of CNT arrays; the vertically aligned CNTs of uniform height $h$ and radius $r$ are placed on a grounded cathode with separation $S$ and anode-cathode distance $D$ [46].....	42

Figure 33 –	Contour plot from a nine CNT array with spacing $S$ of 3 $\mu\text{m}$ , height $h$ of 3 $\mu\text{m}$ , radius of 50 nm, and anode-cathode spacing of 80 $\mu\text{m}$ with a positive 100V potential showing a drop of approximately 15% between the center emitters and the emitters on the edge [46] .....	43
Figure 34 –	Simulations on arrays of 3x3, 7x7, and 11x11 with constant heights and radius with a varied spacing ranging from $S=0.3h$ to $S=5.3$ , showing for the assumed optimal spacing of $S=2h$ a decrease of 11% for the center CNT [46] .....	43
Figure 35 –	Current density as a function of the ratio between intertube separation an height, showing from simulations the optimal current density is obtain when $S=3h$ [46] .....	45
Figure 36 –	SEM image of SiC test sample masked with SU-8.....	51
Figure 37 –	SEM of SiC sample after $\text{O}_2$ RIE showing no change in surface texture .....	52
Figure 38 -	SEM of SiC sample after $\text{O}_2$ RIE and 10 minute soak in 110 C 1165 stripper showing no change in surface texture.....	53
Figure 39 -	SEM of SiC sample after $\text{O}_2$ RIE, 10 minute soak in 110 C 1165 stripper and 10 minutes in plasma asher showing no change in surface texture.....	53
Figure 40 –	SEM image of SiC test piece RIE etched at a flow rate of 30:1 $\text{CF}_4:\text{O}_2$ at 250mW for 30 minutes.....	54
Figure 41 -	SEM image of SiC test piece etched at a flow rate of 30:1 $\text{CF}_4:\text{O}_2$ at 250mW for 60 minutes .....	54
Figure 42 -	SEM image of SiC test piece etched at a flow rate of 30:1 $\text{CF}_4:\text{O}_2$ at 250mW for 90 minutes .....	55
Figure 43 –	SEM image of test sample 2 after a 25 min RIE at a flow rate of 13:5 sccm $\text{CF}_4:\text{O}_2$ at 250mW prior to nickel mask removal.....	57
Figure 44 –	SEM image of test sample 2 after a 25 min RIE at a flow rate of 13:5 sccm $\text{CF}_4:\text{O}_2$ at 250mW after nickel mask removal .....	57
Figure 45 –	SiC temperature and heating profiled for initial sample heating and carbon nanocap formation.....	58
Figure 46 –	SiC temperature and heating profile between 1250 C and 1700 C.....	59

Figure 47 –	Pre-anneal heating cycle between 1250 C and 1700 at a constant 37% power, showing a heat rate of approximately 54.5 degrees/minute .....	59
Figure 48 –	C-face SiC sample annealed for 60 minutes at 1700 C, inset shows an approximate growth of 250 nm .....	60
Figure 49 –	Si-face SiC sample annealed for 3 hours at 1700 C, inset shows an approximate growth of 200-225 nm .....	61
Figure 50 –	45 degree surface view of Si-face SiC sample annealed for 3 hours at 1700 C, showing CNT caps and amorphous carbon .....	61
Figure 51 –	Alice with airgap (AA) test setup with a 215 $\mu\text{m}$ anode-sample gap .....	62
Figure 52 –	LICE with Teflon <sup>®</sup> space (AT) with an emission area of .0186 $\text{cm}^2$ and 100 $\mu\text{m}$ anode-sample gap .....	63
Figure 53 –	Pochet setup with Teflon <sup>®</sup> space (MP) with an emission area of .0186 $\text{cm}^2$ and 100 $\mu\text{m}$ anode-sample gap (Pochet 2006).....	63
Figure 54 –	AFIT field emission vacuum chamber setup .....	64
Figure 55 –	Field emission measurement setup, current was derived from voltages measured across 1k $\Omega$ resistors .....	65
Figure 56 –	SEM image of sample J1 after 20 min RIE and prior to nickel mask removal, (left) planar view of surface at 13k magnification, (right) 45 degree view taken at 13k magnification .....	69
Figure 57 –	SEM image of sample J2 after 20 min RIE and prior to nickel mask removal, (left) planar view of surface at 13k magnification, (right) 45 degree view taken at 15k magnification .....	69
Figure 58 –	SEM image of sample set J after 20 min RIE and prior to nickel mask removal showing the inter-pillar spacing, (left) J1, (right) J2.....	70
Figure 59 –	SEM image of sample set J after 20 min RIE and after nickel mask removal, (left) J1, (Right) J1 .....	70
Figure 60 –	SEM image of the wave pattern created by UV light refraction on the during the photolithography process.....	71
Figure 61 –	SEM image of sample K1 after 20 min RIE and after nickel mask removal, (left) planar view of surface at 13k magnification, (right) 45 degree view taken at 15k magnification .....	72

Figure 62 –	SEM image of sample K2 after 20 min RIE and after nickel mask removal, (left) planar view of surface at 13k magnification, (right) 45 degree view taken at 15k magnification .....	72
Figure 63 –	SEM image of sample K3 after 20 min RIE and after to nickel mask removal, (left) planar view of surface at 13k magnification, (right) 45 degree view taken at 15k magnification .....	73
Figure 64 –	SEM image of sample set K after 20 min RIE and after nickel mask removal showing the inter-pillar spacing, (left to right) K1, K2, and K3 .....	73
Figure 65 –	Comparison of sample set L after 20 min RIE and prior to nickel mask removal taken at 45 ° and 15K magnifications, (left) L1 had the PR removed prior to RIE(right) L2 had PR remaining prior to RIE .....	74
Figure 66 –	Comparison of sample set L after 20 min RIE and after nickel mask removal taken at 45° and 15K imaginations, (left) L1 had the PR removed prior to RIE(right) L2 had PR remaining prior to RIE .....	74
Figure 67 –	SEM image of etched nickel on a H sample, showing the lack of thorough Ni etching and spider web Ni pattern on unmasked region.....	75
Figure 68 –	SEM images taken at 45 ° of sample set H after 20 min RIE and after to nickel mask removal, showing the results of a defined nickel mask (left) H2 at 20k magnification, (right) H3 at 20k magnification .....	76
Figure 69 –	SEM image of the etch portion of the SiC, (left) prior to Ni removal, (right) after Ni removal.....	76
Figure 70 –	SEM image taken at 20k magnification of sample J2 showing the growth of CNTs on the pillars after 15 minute softbake, 30 minute nanocap formation and 3 hour CNT growth.....	78
Figure 71 –	SEM image taken at 200k magnification of CNT film found on top of structure found on sample J2 in figure ().....	78
Figure 72 –	SEM image taken at 100k magnification of vertically and horizontally grown CNTs found on pillar of sample J2, 15 minute softbake, 30 minute nanocap formation and 3 hour CNT growth .....	79
Figure 73 –	SEM image taken at 70k magnification of etched surface of sample J2 showing probable CNT growth, 15 minute softbake, 30 minute nanocap formation and 3 hour CNT growth.....	80

Figure 74 –	SEM image taken at 9k magnification of CNT growth on pillar of from sample set K, 30 minute nanocap formation and 3 hour CNT growth .....	81
Figure 75 –	SEM image taken at 50k magnification of CNT growth on pillar of from sample set K showing the CNT carpet structure and the surface morphology, 30 minute nanocap formation and 3 hour CNT growth .....	81
Figure 76 –	SEM image taken at 130k magnification of probable CNT growth on a pillar from sample L1, 30 minute nanocap formation and 4.5 hour CNT growth.....	82
Figure 77 –	SEM image taken at 50k magnification of probable CNT growth region shown in previous figure on a pillar from sample L1, 30 minute nanocap formation and 4.5 hour CNT growth.....	83
Figure 78 –	SEM image taken at approximately 90 degrees and 3.5k magnification showing the pillar structure found on sample L1 .....	83
Figure 79 –	SEM images taken at 90 degrees of sample H2, (right) landscape view showing the pillar and spacing, (left) cleaved pillar structure at 11k magnification with CNT growth; C-face SiC with 30 min nanocap formation and 1 hour growth.....	84
Figure 80 –	SEM image at 150k magnification of CNT growth on top of pillar on sample H2, showing 270-280 nm of growth after 30 min nanocap formation and 1 hour growth.....	85
Figure 81 –	SEM image taken of etched surface of sample H2 showing probable CNT growth for 30 min nanocap formation and 1 hour growth, (left) 50k magnification, (right) 100k magnification.....	85
Figure 82 –	SEM image takes at 11k magnification of inter-region boundary between etched region and unetched region, unetched region showing CNT carpet growth.....	86
Figure 83 –	Field emission testing current density (J-E) curves for sample J1, AT setup runs 1, 2, and 5 .....	88
Figure 84 –	Field emission testing Fowler-Nordheim plots for sample J1, AT setup runs 1, 2, and 5 .....	89
Figure 85 –	Field emission testing current density (J-E) curves for sample J1, MP setup runs 1 and 2.....	90

Figure 86 –	Field emission testing Fowler-Nordheim plots for sample J1, MP setup runs 1 and 2 .....	91
Figure 87 –	Field emission testing current (IV) curves for sample J2, AA setup runs 1-4 and 6.....	92
Figure 88 –	Field emission testing Fowler-Nordheim plots for sample J2, AA setup runs 1-4 and 6 .....	93
Figure 89 –	Field emission testing current density (J-E) curves for sample J2, AT setup runs 4-6.....	94
Figure 90 –	Field emission testing Fowler-Nordheim plots for sample J2, AT setup runs 4-6.....	95
Figure 91 -	Field emission testing current density (J-E) curves for sample J2, MP setup runs 2, 3 and 6.....	96
Figure 92 –	Field emission testing Fowler-Nordheim plots for sample J2, MP setup runs 2, 3, and 6 .....	97
Figure 93 –	Field emission testing current (IV) curves for sample K1, AA setup runs 1, 2, and 4.....	99
Figure 94 –	Field emission testing Fowler-Nordheim plots for sample K1, AA setup runs 1, 2 and 4 .....	99
Figure 95 –	Field emission testing current density (J-E) curves for sample K1, MP setup runs 2-4, 7, and 11 .....	101
Figure 96 –	Field emission testing Fowler-Nordheim plots for sample K1, MP setup runs 2-4, 7, and 11 .....	102
Figure 97 –	Field emission testing current density (J-E) curves for sample K2, AT setup runs 2-6.....	103
Figure 98 –	Field emission testing Fowler-Nordheim plots for sample K2, AT setup runs 2-6.....	103
Figure 99 –	Field emission testing current density (J-E) curves for sample K2, MP setup runs 1-3 and 5-8.....	105
Figure 100 –	Field emission testing Fowler-Nordheim plots for sample K2, MP setup runs 1-3 and 5-8.....	106
Figure 101 –	Field emission testing current density (J-E) curves for sample K3, MP setup runs (left) 1, 2, 4, and 5 (right) runs 9-11 .....	108

Figure 102 – Field emission testing Fowler-Nordheim plots for sample K3, MP setup (left) 1, 2, 4, and 5 (right) runs 9-11 .....	109
Figure 103 – Field emission testing current (IV) curves for sample L1, AA setup runs 3, 4, 6, and 7 .....	110
Figure 104 – Field emission testing Fowler-Nordheim plots for sample L1, AA setup runs 3, 4, 6, and 7 .....	111
Figure 105 – Field emission testing current density (J-E) curves for sample L1, MP setup runs 1, 2, 3, and 5.....	112
Figure 106 – Field emission testing Fowler-Nordheim plots for sample L1, MP setup runs 1, 2, 3, and 5 .....	113
Figure 107 – Field emission testing current density (J-E) curves for sample L2, AT setup runs 1-3.....	115
Figure 108 – Field emission testing Fowler-Nordheim plots for sample L2, AT setup runs 1-3.....	115
Figure 109 – Field emission testing current density (J-E) curves for sample L1, MP setup (left) runs 1-2 with filter, (right) runs 1-2 using raw data .....	116
Figure 110 – Field emission testing Fowler-Nordheim plots for sample L1, MP setup runs (left) runs 1-2 with filter, (right) runs 1-2 using raw data .....	117
Figure 111 – Field emission testing current density (J-E) curves for sample H1, MP setup runs 6-8 and 15 .....	119
Figure 112 – Field emission testing Fowler-Nordheim plots for sample H1, MP setup runs 6-8 and 15 .....	120
Figure 113 – Field emission testing current density (J-E) curves for sample H2, MP setup runs 8-9.1, 11, 15, 16, and 18 .....	122
Figure 114 – Field emission testing Fowler-Nordheim plots for sample H2, MP setup runs 8-9.1, 11, 15, 16, and 18 .....	123
Figure 115 – Field emission testing current density (J-E) curves for sample H3, MP setup runs 6-8, 12, 14, and 15 .....	125
Figure 116 – Field emission testing Fowler-Nordheim plots for sample H3, MP setup runs 6-8, 12, 14, and 15 .....	126
Figure 117 – Field emission testing current density (J-E) curves for sample H4, MP setup runs (left) 11-13, (right) 16-19.....	128

Figure 118 – Field emission testing Fowler-Nordheim plots for sample H4, MP setup runs (left) 11-13, (right) 16-19 .....	129
Figure 119 – Field emission testing current density (J-E) curves comparing sample H1 run 12, sample H2 run 16, sample H3 run 9, and sample H4 run 18 .....	131
Figure 120 – Field emission testing Fowler-Nordheim plots comparing sample H1 run 12, sample H2 run 16, sample H3 run 9, and sample H4 run 18.....	132
Figure 121 – Current stability plots for sample K1 MP run 8.....	133
Figure 122 – Current stability plots for sample J1 AA runs (left) 5 and (right) 7 .....	134
Figure 123 – Current stability plots for (left) sample H2 MP Run 11 and (right) sample H2 MP Run 14.....	134
Figure 124 – Arc Discharge Chamber [55].....	141
Figure 125 – Laser Ablation Process [55].....	142
Figure 126 – CVD CNT Growth with Catalyst [57].....	143
Figure 127 – CVD Grown CNT with Varied Catalyst Thickness [57].....	144
Figure 128 – CNT Density, Length, Diameter Catalyst Dependence [57] .....	144
Figure 129 – Thermal CVD Furnace [58] .....	145
Figure 130 – PE-CVD Chamber. ....	146
Figure 131 – Planar view of stacking sequence of SiC.....	147
Figure 132 – Stacking sequence of 3C, 4H, and 6H SiC [49].....	148

## List of Tables

	Page
Table 1 – Electrical and Mechanical Properties of CNTs and Other Material .....	10
Table 2 – Semiconductor properties of SiC with other semiconductors [48].....	46
Table 3 – Etch Rate Study Parameters using TRION RIE .....	56
Table 4 – Summary of Etch Rate Step-height analysis.....	56
Table 5 – Sample J1 AT Setup Run Parameters .....	87
Table 6 – Sample J1 MP Setup Run Parameters.....	89
Table 7 – Sample J2 AA Setup Run Parameters.....	91
Table 8 – Sample J2 AT Setup Run Parameters .....	94
Table 9 – Sample J2 MP Setup Parameters .....	96
Table 10 – Sample K1 AA Setup Run Parameters .....	98
Table 11 – Sample K1 MP Setup Parameters.....	100
Table 12 - Sample K2 AT Setup Run Parameters .....	102
Table 13 – Sample K2 MP Setup Parameters .....	104
Table 14 – Sample K3 MP Setup Parameters .....	107
Table 15 – Sample L1 AA Setup Run Parameters.....	109
Table 16 – Sample L1 MP Setup Parameters .....	111
Table 17 – Sample L2 AT Setup Run Parameters .....	114
Table 18 – Sample L2 MP Setup Parameters .....	116
Table 19 – Sample H1 MP Setup Run Parameters .....	118
Table 20 – Sample H2 MP Setup Run Parameters .....	121
Table 21 – Sample H3 MP Setup Run Parameters .....	124

Table 22 – Sample H4 MP Setup Run Parameters .....	127
Table 23 – Sample to Sample Comparison of Performance Factors .....	130
Table 24 - Sample to Sample Comparison for Sample Set H.....	131
Table 25 – Current Stability Testing Results .....	133
Table 26 – Summary of RIE on SiC polytypes [50].....	149

# ***FIELD EMISSION OF THERMALLY GROWN CARBON NANOSTRUCTURES ON SILICON CARBIDE***

## **Chapter I: Introduction**

### **1.1. General Issue**

Researchers have investigated the ideal high power microwave (HPM) source for nearly five decades [1, 2]. Obtaining high-quality electron beams is one of the key problems in the field of pulsed power and HPM systems [3]. The electron beams in these systems are produced by one of three primary sources, depending on the application including explosive field emission, thermionic cathodes, and field electron emission [4]. Field emission in general relies on electrons overcoming the potential barrier between the cathode and the environment.

Explosive electron emission occurs when a large electric field is applied to a field emission cathode [5]. The induced field emission current heats up the cathode material and any absorbed gases. As the cathode material and gases continue to heat, they eventually explode, creating a plasma in the system. The generated plasma acts as the source of electrons because it continues to interact with the cathode surface inducing both thermionic and field emission. This explosively formed plasma is also a shortfall of the thermionic cathode systems, because as the plasma moves across the surface it causes a change in device impedance and eventual pulse shortening. Pulse shortening is commonly defined as the voltage and current pulses exceeding the emitted microwave pulse width by at least 50% [2].

Thermionic emission research, first discussed by British physicist Owen Richardson, has been conducted since the early twentieth century [6]. In thermionic

emission, the cathode is heated to give its electrons sufficient energy to overcome the work function barrier. The emission current depends on the operating temperature and the work function of the cathode. The current density for thermionic emission is commonly given by the Richardson-Laue-Dushman relation [6]. Modern, commercially available thermionic cathodes operate at temperatures ranging from 1050-1350 K and have effective work functions between 1.8-2.0 eV. One problem that arises in thermionic cathodes is the degradation of the cathode material due to the high operating temperatures. The degradation both depletes the cathode material and causes arcing due to unintended coating of cathode material on the anode.

Field electron emission research, like thermionic emission research, began in the early 20<sup>th</sup> century. For field electron emission, or cold cathodes, a large electric field is applied normal to the cathode surface. This field distorts the shape of the potential barrier between the cathode surface and the vacuum. As a result, the barrier is reduced allowing some electrons to quantum-mechanically tunnel through the potential barrier. This phenomenon is frequently identified by the use of the Fowler-Nordheim criteria published in 1928 [7]. The Fowler-Nordheim criteria show that the emission current density depends on the magnitude of the electric field and the cathode work function. Until recently, field electron emission sources have suffered from a lack of stable cathode materials. Even though field electron emission occurs through quantum mechanical tunneling, the process causes the devices and cathode material to heat and thermally breakdown.

Research on the ideal cathode has been going on for more than half a century. Dr. John R. Pierce, a researcher at Bell Labs and inventor of the Pierce Electron Gun, gave the primary characteristics of an ideal cathode in which the cathode [4]:

1. Emits electrons freely, without any form of persuasion such as heating or bombardment (electrons would leak off from it into vacuum as easily as they pass from one metal to another);
2. Emits copiously, supplying an unlimited current density;
3. Lasts forever, its electron emission continuing unimpaired as long as it is needed;
4. Emits electrons uniformly, traveling at practically zero velocity

Takao Utsumi stated that as the ratio between height and width of the emitting structure increased the field emission would also increase. He concluded that the field emitter would have a rounded whisker shape as shown in Figure 1 [8][7]. The discovery of carbon nanotubes (CNTs) and their unique properties, have nearly solved both Pierce's and Utsumi's idea for the ideal cathode.

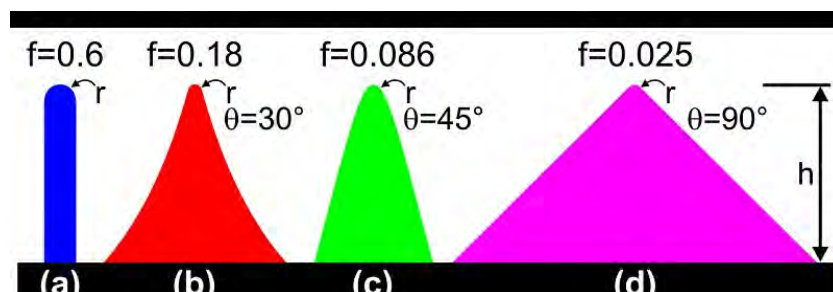


**Figure 1 – Diagram of Utsumi's ideal cathode configuration with a figure a merit defined as  $f_i = (I_i/I_0)*(V_i/V_0)^{-1}*(L_i/L_0)^{-1}$  where  $I_i$ ,  $V_i$ , and  $L_i$  are emission current, gate voltage, and linear device dimension of the  $i$ th field emitter and  $I_0$ ,  $V_0$ , and  $L_0$  are the parameters from an ideal field emitter. [8]**

## 1.2. Summary of Current Knowledge

### 1.2.1. Carbon Nanotubes

Iijima published the first finding on carbon nanotubes (CNTs) in 1991 while investigating the soot of an arc-discharge experiment to create spherical carbon structure called buckyballs or fullerenes [9]. Using transmission electron microscope images of the soot, Iijima discovered what he believed to be concentric graphitic based tubes in the arc-discharge, shown by the TEM image in Figure 2.

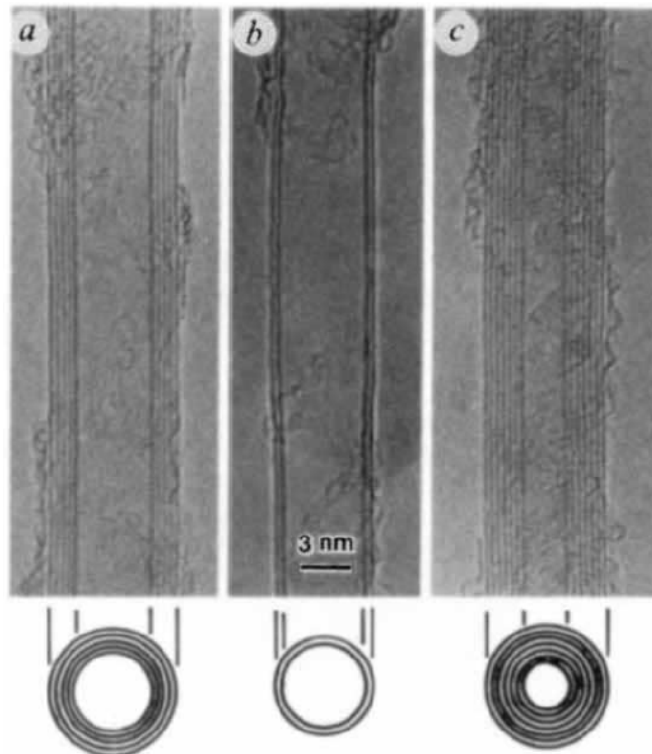


**Figure 2 – TEM images of Iijima's CNT discovery showing the structure of single-walled and multi-walled CNTs [9]**

Over the course of the next four year researchers continued to refine the arc-discharge process enough to synthesize sufficiently pure material to enable the creation and analysis of CNT-based devices. [10].

Many of the CNT's properties stem from their large ratio between height and diameter ( $h/d$ ). This ratio makes them quasi-one-dimensional in terms of quantum mechanics. CNTs also have carbon bonds similar to those found in other robust carbon materials such as diamonds. Due to their strong bond strength, CNTs exhibit many of the same mechanical and chemical properties of diamonds, including a large Young's modulus and near chemical inertness. CNTs can be either metallic or semiconducting depending on their diameter and have an electrical conduction near zero.

Carbon nanotube fabrication involves three primary methods including: arc discharge synthesis, laser ablation synthesis, and thermal synthesis. In the first two, the CNTs produced are deposited on a secondary surface. A primary problem with these techniques is the large quantity of soot, or amorphous carbon, deposited with the CNTs. The CNTs must be cleaned of the soot before being used in devices. One method of thermal synthesis, chemical vapor deposition, requires the use of a metallic catalyst which must be removed during post processing. Many of the post processing methods have the potential to damage the CNTs or devices. A second method of thermal synthesis involves the thermal decomposition of carbide substrate such as silicon carbide to produce CNTs. Because no catalyst is used in this process little to no post processing of the CNTs is involved. A drawback, however is that the CNT layer on the substrate is very dense.

### **1.2.2. Field Electron Emission from CNTs**

As discussed previously, the principle of field electron emission is based on the application of a very high electric field to extract electrons from a metal. The same process can also be applied to highly doped semiconducting surfaces [11]. The applied

field can be reduced by creating elevated structures on the cathode surface. The physical whisker-like high aspect ratio structure of a CNT makes them ideal structures for cathodes. However as the density of emitting structures, such as CNTs, increases the field emission has been shown to decrease. This is caused by a phenomenon referred to as field emission screening [11, 12]. This effect is illustrated in Figure 3. To decrease the effects of screening, research has shown that the ideal separation between CNTs is between one and three times the CNTs' length [11, 12]. Experimentally the creation of CNT arrays has been shown possible by CNTs synthesis using metal catalyst [12].

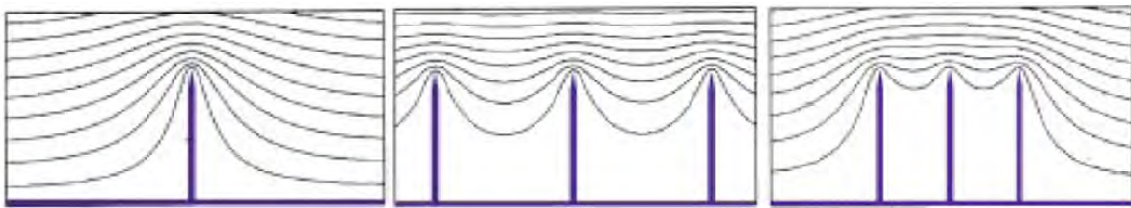


**Figure 3 – Field screening effect for emitters (left-to-right) single emitter, one-to-one emitter spacing, and close packed emitters [12]**

### 1.3. Research Problem

The current problem with the non-catalytic thermal decomposition process is field screening caused by the densely packed uniform CNTs. To overcome this problem, a method of patterning must be developed that can withstand the high temperatures required for CNT synthesis, and determine whether or not the patterning of the CNT film can increase the field enhancement factor of the CNTs. When a patterning process is found, how does the spacing affect the field emission? The research conducted for this thesis will focus on the field emission characterization of patterned CNT pillars synthesized by thermal decomposition of silicon carbide.

#### **1.4. Assumptions and Limitations**

Current known limitations for this effort include the inability to use a photolithographic process to achieve minimum features accurately below one micron. The impact of this problem is a result of the CNT's small diameter (5-20nm). The relatively large feature size would result in tufts of CNTs rather than individual CNTs probably causing localized screening effects. A possible solution to this problem is the use of an electron beam system patterning where it may be possible to achieve sub micron feature sizes.

#### **1.5. Approach and Methods**

The patterned CNT's field emission properties will be characterized through the use of experimental vacuum test fixtures. Field emission data will be analyzed to determine if patterned CNT field emission shows decreased turn-on voltages, decreased threshold voltages, higher maximum current densities, and Fowler-Nordheim field emission. Non-field emission analysis will include the use of standard material characterization techniques including scanning electron microscopy (SEM).

#### **1.6. Thesis Structure**

The structure of this thesis will include chapters on literature and theory review, experimental methodology, results and analysis, and conclusion and recommendations.

## Chapter II: Literature & Theory Review

### 2.1. Chapter Overview

The purpose of this chapter is to discuss the background and synthesis of CNTs, field emission process, current CNT field emission issues, and patterning of silicon carbide (SiC).

### 2.2. CNT Background

#### 2.2.1. CNT Structure

CNT's basic structure is derived from single layer graphite or graphene rolled into a cylinder. Graphene has basis vectors of  $\vec{a}_1 = (\sqrt{3}, 0)$  and  $\vec{a}_2 = (\sqrt{3}/2, 3/2)$  with an atomic distance  $a=0.142$  angstroms. To form the CNT, a graphene layer like that in Figure 4 is cut into rectangular strips with a circumferential vector  $C_h = n * \vec{a}_1 + m * \vec{a}_2$ . This circumferential vector yields the CNT's radius in (2.1).

$$R = \frac{C}{2} \pi = \frac{(\sqrt{3})}{(2\pi)} a \sqrt{n^2 + m^2 + nm} \quad (2.1)$$

Several types of CNTs based on their circumferential vectors shown in Figure 5. The 'zigzag' CNT has a circumferential vector only along one of the basis vectors. The 'armchair' CNT has a circumferential vector exactly between the two basis vectors or when  $n=m$ . CNTs, where  $n \neq m$  and not 'zigzag' or 'armchair' are considered to be chiral meaning that the CNT lack internal symmetry. Also when the graphene is rolled into the CNT the carbon-to-carbon (C-C) bonds are no longer identical. For example, in a zigzag with  $n=m$  (armchair) the non-axial bonds are identical, but differ from the axial bonds.

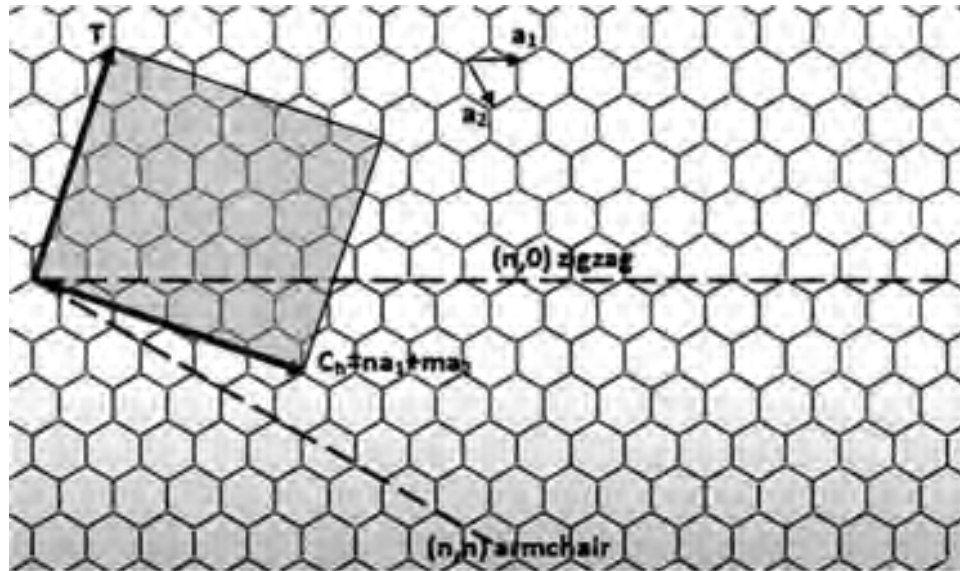


Figure 4 – CNTs are derived from rolled up graphene sheet cut along one of three axis creating either  $(n,n)$  armchair,  $(n,0)$  zigzag, or a general chiral CNTs. [13]

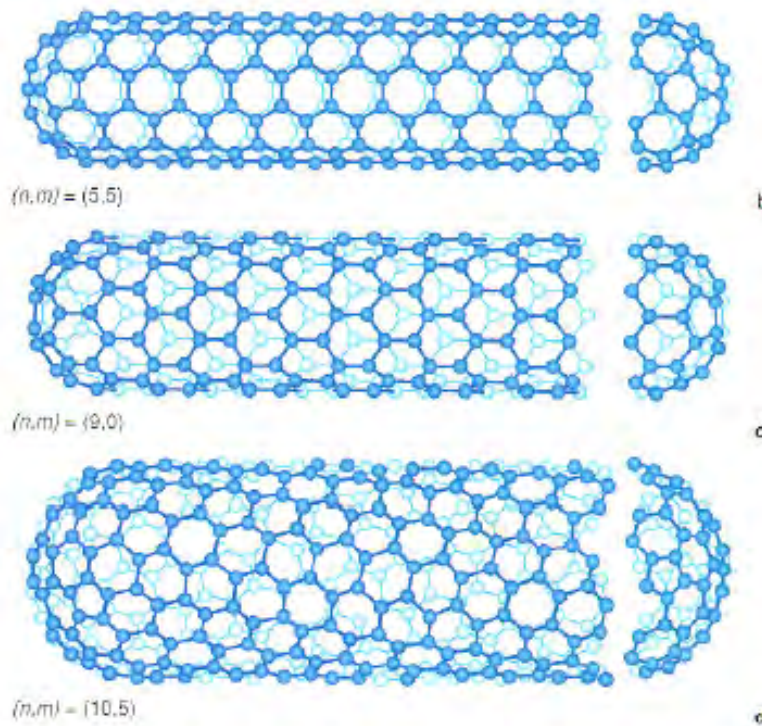


Figure 5 – Examples of (top) armchair  $(n,n) = (5,5)$ , (middle) zigzag  $(n,m) = (9,0)$ , and (bottom) Chiral  $(n,m) = (10,5)$  [14]

### 2.2.2. Properties

General electrical and mechanical properties of CNTs and other materials are given in Table 1. The electronic properties of CNTs, however, are of particular interest in field emission work. Early calculations showed that the electronic properties of CNTs are sensitive to their geometric structure [15]. Conductivity of SWCNTs generally follows the following rules: armchair  $(n, n)$  tubes are metallic, zigzag tubes  $(n, m)$  with  $n - m = 3j$ , where  $j$  is a non-zero integer, are very tiny-gap semiconductors; and all others are large-gap semiconductors [15]. The electronic density of states (DOS) for various tube chirality is shown in Figure 6. For all cases, the CNTs operate in one-dimensional DOS similar to quantum wires. In Figure 6 the armchair nanotube is metallic due to symmetry; the chiral nanotube displays a tiny gap due to curvature effects, but acts metallic at room temperature; and the zigzag nanotube is a large-gap semiconductor [16].

**Table 1 – Electrical and Mechanical Properties of CNTs and Other Material**

Property	CNT	Other Material
Electrical Conductivity	Metallic or Semiconducting	
Electrical Transport	Ballistic, no scattering	
Resistivity	$5.8 \times 10^{-6} \Omega \text{ cm}$	Graphite ( $1.375 \Omega \text{ cm}$ )
Energy Gap (semiconductor)	$E_g [\text{eV}] \sim 1/d$	Graphite (5.0 eV)
Maximum Current Density	$\sim 10^{10} \text{ A/cm}^2$	Copper ( $4 \text{ A/mm}^2$ )
Thermal Conductivity	6000 W/Km	Copper (401 W/Km) Diamond (2320 W/Km)
Mechanical	E-Modulus - 1000+ GPa Tensile Strength – 11-63k MPA	Steel (200 GPa) Steel (760 MPA)

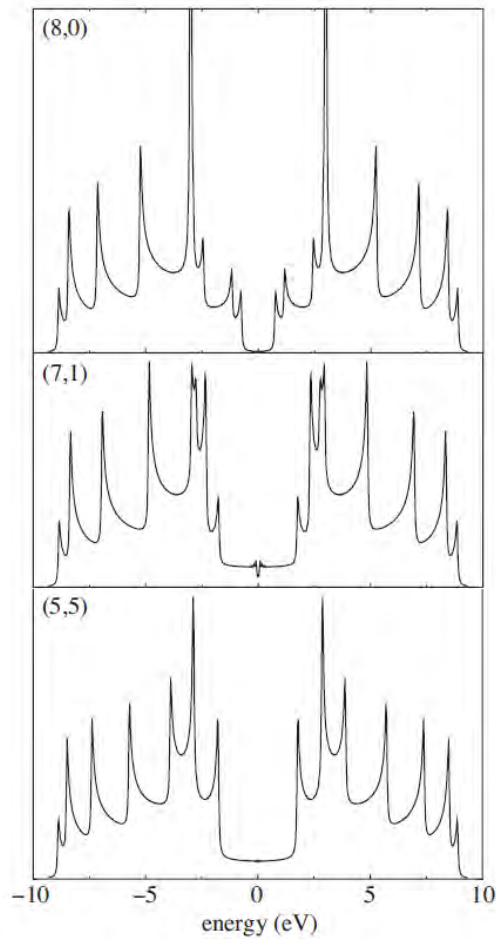


**Figure 6 – One dimensional density of states for different nanotube configurations. The armchair nanotube (5, 5) is metallic due to symmetry; the chiral nanotube (7, 1) displays a tiny gap due to curvature effects, but acts metallic at room temperature; and the zigzag nanotube (8, 0) is a large-gap semiconductor. [16]**

For CNTs with semiconductor properties the band gap is inversely proportional to the diameter of the tube with a value of 0.8 eV for a 1 nm diameter tube. Because MWCNTs are formed from layers of smaller CNTs, they have larger diameters and as such are always metallic. The typical diameters for SWCNT and MWCNT are 0.7 nm and 10-20 nm, respectively. CNTs, because of their shape and limited number of states, have the ability to transport electrical charge ballistically. Ballistic transport infers that there is little electron scattering for distances up to several microns resulting in a

decreased resistivity. In comparison, undoped gallium arsenide, with an electron mobility of  $8800 \text{ cm}^2/\text{V}\cdot\text{s}$ , has a mean free path between collisions of approximately 35 nm. The decreased resistivity, large conductivity, and high thermal stabilities allow current densities of  $10^{10} \text{ A/cm}^2$  [2]. The physical properties come from the double bonds. These bonds are stronger than the bonds found in diamonds resulting in high mechanical strengths and thermal transport characteristics.

### 2.3. CNT Growth by Thermal Decomposition

Surface decomposition of SiC was first reported by Kusunoki *et al* in 1997 [17]. In that discovery, they found, during TEM observation, that CNTs formed on the carbon surface of 3C-SiC after heating the surface to  $1700 \text{ }^\circ\text{C}$  using a YAG laser [17]. Using a vacuum electric furnace Kusunoki *et al* were able to grow CNTs into the carbon face of a 6H-SiC wafer [18]. Future work performed by Mitchel *et al* observed the growth of CNTs into both Si and C-face of SiC under similar growth conditions as Kusunoki *et al* [19]. The CNT layer formed on the Si-face of SiC is shown in Figure 7.

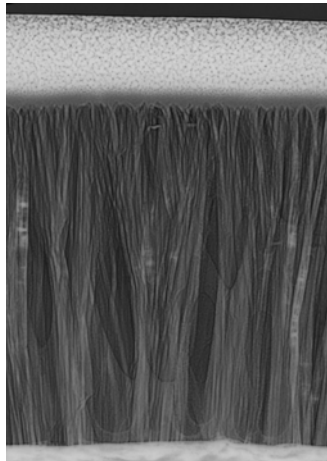


**Figure 7 – TEM image of CNT growth on Si-face of SiC, top layer is a platinum coating used to protect the CNT layer during preparation [19]**

The thermal decomposition process involves placing SiC wafers with either polished C faces or Si faces in a furnace at high temperatures (1250 to 1700 °C) and low pressure ( $10^{-4}$  Torr) for a short period of time [18, 20, 21]. In contrast to catalyst grown CNTs, CNTs grown by thermal decomposition grow perpendicularly and self aligned into the SiC substrate as diagramed in Figure 8. A drawback to this method is that the CNT layer is densely packed as observed in Figure 7.

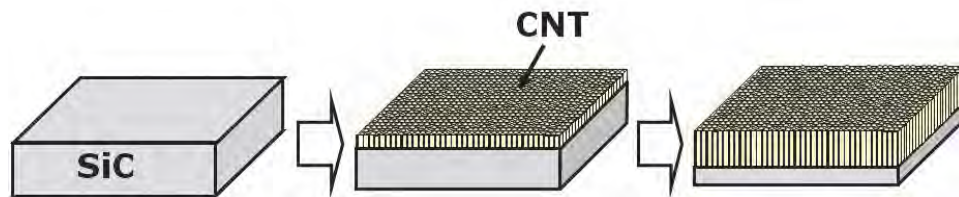


**Figure 8 – Flow diagram of CNT growth using thermal decomposition showing CNTs densely packed CNTs growing into the surface as time increases**

Kusunoki *et al* found through TEM images that CNTs grown using thermal decomposition had distinct characteristics including: two to five layered MWCNTs with diameters of 25 nm; perpendicular growth; higher density growth; CNTs atomically bond to the SiC substrate; and a selective zigzag configuration [18]. Maruyama *et al* concluded that the selective chirality is a result of the dangling bond found on the surface of the SiC substrate during decomposition [22]. Figure 9 shows a schematic side (a) and top (b) view of 6H-SiC. The dangling bonds from the carbon atoms are shown in the side view. Those dangling bond form the basis for the zigzag CNT (c), as the nanocaps are formed and then the CNT.

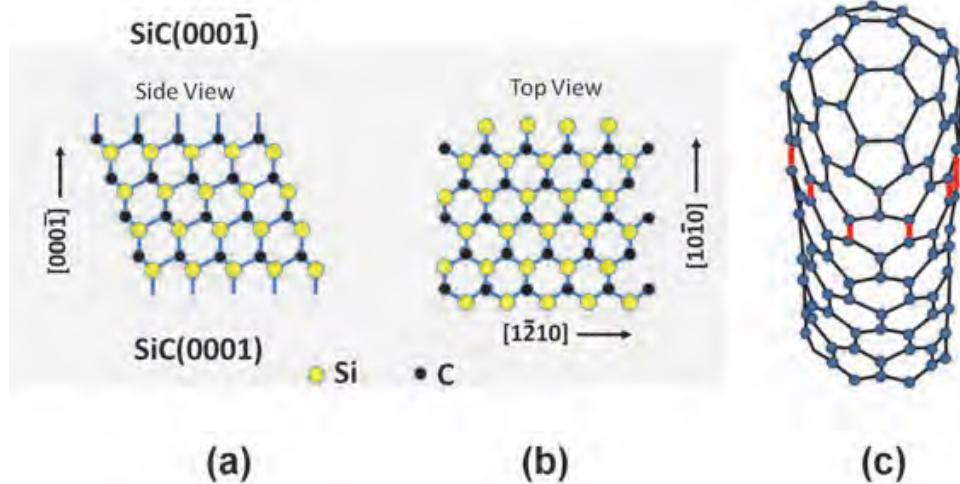


**Figure 9 – Schematic showing the side(a) and top(b) view of C-face SiC, the dangling bonds at the top of the side view form the basis for the zigzag CNT (c)[22]**

### 2.3.1. Formation of Carbon Nanocaps

It is commonly believed that the formation of CNTs from SiC decomposition starts with the formation of carbon nanocaps [18, 22, 23]. Kusunoki *et al* identified the formation of small carbon nanocaps 5 nm in diameter and 1-2 nm in height after annealing at 1250 °C for 30 mins and through TEM measurements determined that the diameter of CNTs grown by thermal decomposition is dependent on the size of the nanocaps [21, 24]. Subsequent heating to 1300 °C resulted in two to three layered nanocaps 3-5 nm in diameter and 3-5 nm in height [18]. During the final annealing process, CNTs formed beneath the nanocaps into the SiC substrate. Through the observation of nanocap formation using TEM and STM, Watanbee *et al* proposed an early model for nanocap formation. Their model is illustrated in Figure 10.

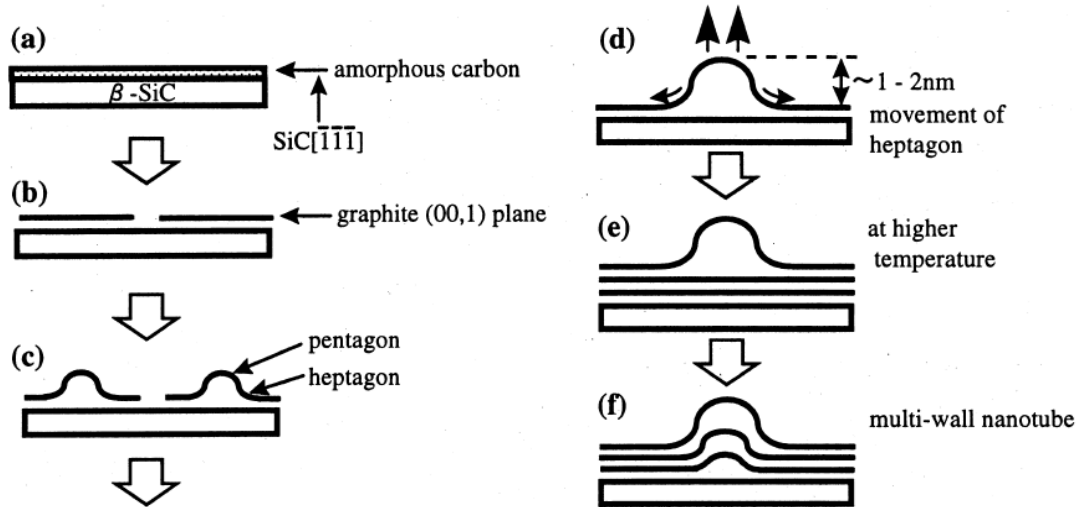


**Figure 10 – Carbon nanocaps formation model proposed by Wantabee *et al.* The model show (a) the formation of amorphous carbon on the surface, (b) crystallization of carbon into a graphite sheet, (c) lifting of the graphite sheet to form nanocaps, (d) growth of nanocaps by a movement of heptagons in opposite direction of growth, (e) formation of additional graphite layers with increased temperature, and (f) beginning formation of MWCNT [23]**

This model involves (a) the formation of amorphous carbon on the SiC surface; (b) the crystallization of the amorphous carbon into a graphene sheet; (c) formation of carbon nanocaps by the lifting of a part of the graphene layer by a generation of pentagons and heptagons in the hexagonally structured graphene; (d) the growth of nanocaps by a movement of heptagons in the opposite direction against the growth direction; (e) at higher temperatures additional graphite layers are formed below the nanotubes; (f) allowing for MWNT to be formed by a lift of the graphite layers [23].

The experimental data gathered by Kusunoki *et al.*, shows that the formation of nanocaps and subsequent nanotubes should maintain a constant diameter during growth, however the model presented by Watanbee *et al* suggests the nanocaps and nanotubes would increase in diameter. To investigate the formation of nanocaps during the thermal decomposition of SiC, Maruyama *et al* investigated nanocap formation using various

experimental techniques [22]. XPS measurements, shown in Figure 11, made before and after heating the SiC surface to 1100 °C show a difference in the quantity of elementary carbon present on the surface [22].

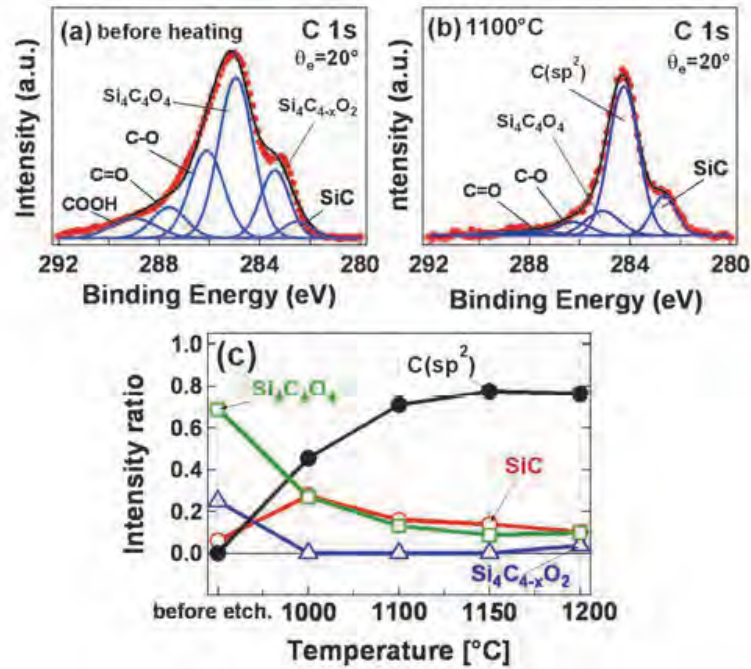


**Figure 11 – Comparison of XPS measurements (a) before heating and (b) after heating. The intensity ratio is shown as a function of temperature with the intensity of carbon increasing as the sample is heated [22].**

Prior to heating, no elemental carbon was observed; however after heating elemental carbon derived from *sp*<sup>2</sup> bonding became dominant in the XPS plots. Both XPS measurements showed the presence of SiC, which indicates that, the formed carbon layers are only a few nanometers thick. The temperature dependence plot shows the presence of carbon starting at 1000 °C with an increasing intensity. The same plot also shows a decrease in both the oxide layer and SiC intensity as the temperature increases to 1200 °C. This accumulation of carbon on the SiC surface leads to nanocap formation. In Figure 12, observations of nanocaps formed at 1250 °C by Bang *et al* are illustrated [25].

Profile measurement of the nanocaps by Bang *et al* shows nanocaps with heights of 1-3 nm and diameters of 3-5 nm [25].

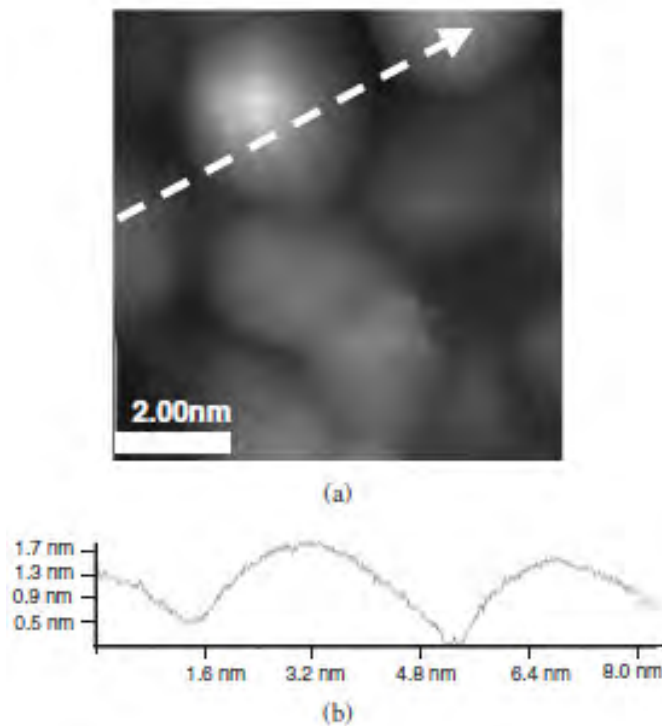


**Figure 12 – (a) Observations of nanocap formation on SiC using STM; (b) profile measurements of nanocaps showing heights of 1-3 nm and diameters of 3-5 nm [25].**

Bang *et al* also reported through the magnification of the STM images shown in Figure 13 the location of both pentagon and hexagon formations in the nanocaps which show that nanocaps have crystallized by the time they form on the SiC surface.

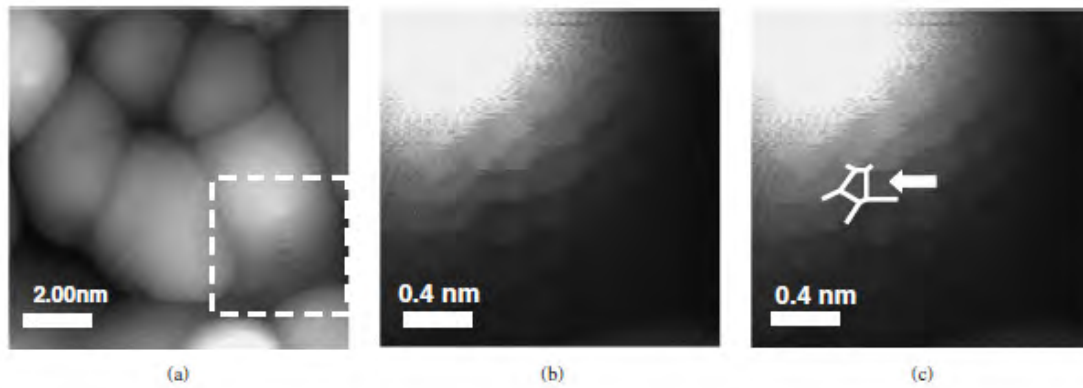


**Figure 13 – Observation by Bang *et al* of pentagon and hexagon formations in the nanocaps showing that the nanocaps have crystallized before forming on the surface [25].**

Using the observation by Bang *et al* along with measurements, Maruyama *et al* observed the crystallization of nanocaps at 1250 °C, while at 1190 °C they observed a mixture of ordered graphene layers and amorphous carbon [22]. Maruyama *et al* claim that carbon nanoparticles accumulate on the SiC and then assemble and coalesce as the temperature is increased until a carbon nanocap is formed [22]. From their observations on the formation of nanocaps, Maruyama *et al* proposed a counter nanocap formation model to Watanabe *et al*'s model previously shown in Figure 10. The proposed model, shown in Figure 14, begins with the accumulation of carbon nanoparticles as Si atoms are desorbed from the surface. As heating continues, carbon particles begin to cluster on the SiC surface to reduce the surface energy. The nanoparticle clusters begin to redistribute the carbon atoms, and the nanoparticles begin to coalesce. Near 1200 °C, the crystallization of the coalesced nanoclusters begins utilizing dangling bonds. As the crystallization continues, the nanocap begins to form. Near 1250 °C the final nanocaps are formed.

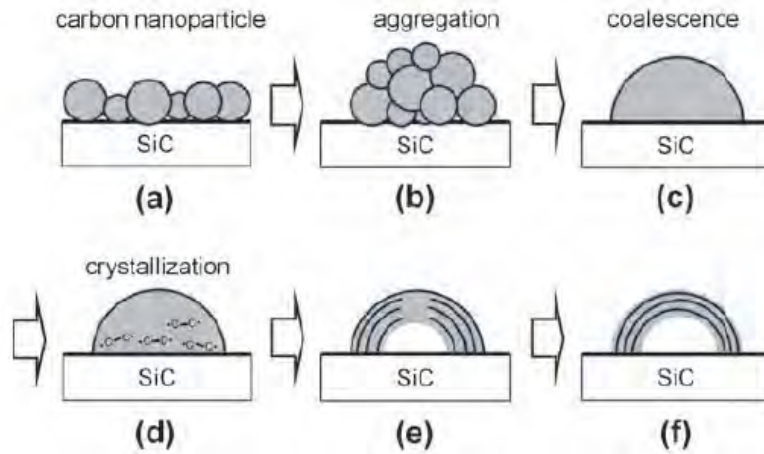


**Figure 14 – Nanocap formation proposed by Maruyama *et al.* (a) accumulation of carbon nanoclusters; (b) clustering of nanoparticles; (c) coalescence of nanoparticles; (d) crystallization of nanoclusters utilizing dangling bonds; (e) crystallization into beginning of nanocap; (f) at 1250 °C nanocaps form [22]**

Kusunoki *et al* conclude that after the formation of the nanocaps, CNTs are synthesized by the diffusion of carbon atoms within a distance of a CNT cross-sectional radius on the SiC surface. [21][24]. This synthesis is shown in the model in Figure 15.

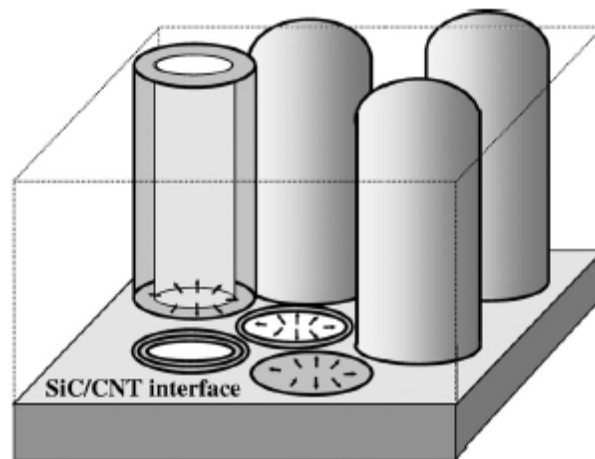


**Figure 15 – Model of CNT growth proposed by Kusunoki *et al*, showing CNT growing into the surface by the diffusion of carbon atoms within a distance of a CNTs cross-sectional radius [24]**

### 2.3.2. Effects of CNT Growth Parameter

Several parameters affect the synthesis of CNTs by the thermal decomposition of SiC. These parameters include the temperature, time, heating rate, and oxygen. Mitchel *et al* investigated the affects of temperature and growth times on CNT grown on SiC [19]. In their investigation, they varied the decomposition time from 30-300 minutes at 1700 °C and analyzed the resultant CNT layer thickness. They found that the growth rates on both the carbon and silicon surfaces were linear, and the rate of growth on the C-face was three times that of the Si-face. Yamauchi *et al* published that by varying the heating rate during growth, the resultant surface morphology changed [26]. Yamauchi *et al*'s investigation involved pre-annealing SiC samples at 1250 °C and annealing the samples at 1700 °C while varying the time required to reach the annealing temperature [26]. At a heating rate of 100 °C/min with a 1250 °C pre-anneal in ultra-high vacuum (UHV) and 1700 °C anneal in low vacuum, the surface included only CNT layers. Conversely, with a heating rate of 400 °C/min and identical vacuum conditions, CNT and amorphous carbon layers were found on the surface. By pre-annealing and annealing the sample in a low vacuum, the 100 °C/min and 400 °C/min heating rates resulted in only CNT layers [26]. From these experiments, they postulated that the surface decomposition rate exceeded the CNT formation rate during the early stages of growth [26].

Kusunoki *et al* proposed an early chemical reaction, (2.2), for the formation of CNT on SiC. Their early methods for thermal decomposition involved annealing in a low vacuum, which could still have residual gases, including oxygen, present during the decomposition process [17]. Maruyama *et al* found through the use of XPS spectra that

the ratio between the peak intensity of SiC component to the carbon *sp*<sup>2</sup> component decreased as the oxygen partial pressure increased, which supports (2.2) [22].

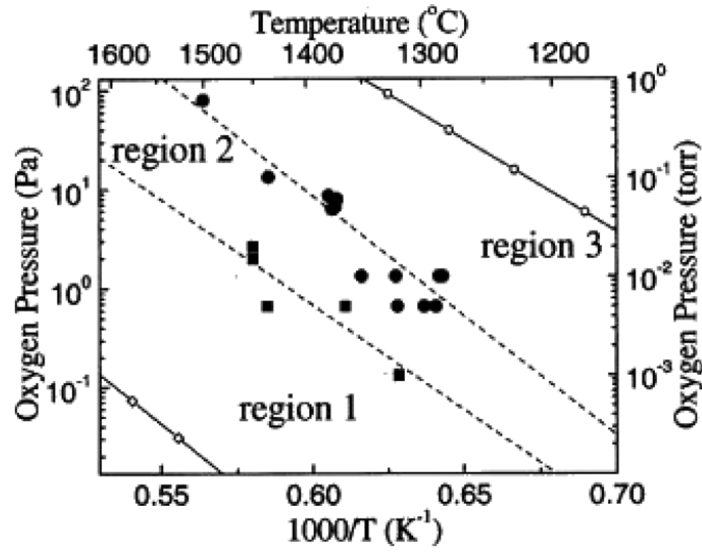
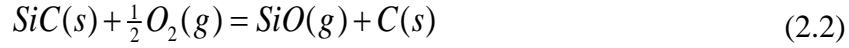
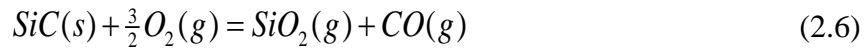
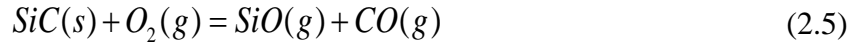
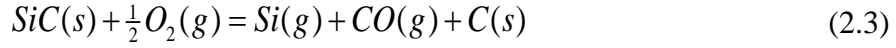


**Figure 16 – Oxygen pressure phase diagram, showing regions 1 and 2 as the active oxidation regions and region 3 as the passive oxidation region [27]**

Using the phase diagram proposed by Song and Smith in Figure 16, the reaction of oxygen and the SiC surface can be delineated into three distinct layers[27], an active oxidation zone in regions 1 and 2 and a passive oxidation zone in region 3 [27]. In region 1 at low pressures and high temperatures the SiC decomposes into SiO according to the reaction equations (2.3) and (2.4) and produces carbon based structures. As temperature decreases or pressure increases and the decomposition process moves through region 2 and 3, Si based oxides and CO are produced as governed by equations (2.5) and (2.6). The oxide layer formed in the passive oxidation zone, equation (2.6), effectively shutting

down any further oxidation. To prevent this, the oxygen pressure must remain in the active oxidation zone.



#### 2.4. Field Emission Process

The predominant and ideal source of electron emission from carbon nanostructures (CNTs) is field emission. Depending on the application, field emission is referenced differently. As discussed previously, field emission in high power microwaves is generally referred to as cold cathode emission, while in other literature it is referred to a cold field electron emission or field electron emission [28, 29]. The common part of these monikers is the use of cold, which refers to the lack of applied heat to the emitting surface unlike that of thermionic emission. In field emission, contrary to thermionic emission, electrons are forced through the potential barrier rather than over the potential barrier. The movement of electrons through a narrowed potential barrier is also referred to as ‘Fowler-Nordheim Tunnelling’ [30]. The name references the 1928 paper published by R. H. Fowler and L. W. Nordheim, which described the tunneling of electron through a roughly triangular barrier and their resulting equation relating the emitted current density to the applied electric field [7]. This paper resulted in subsequent refinements in field emission including work by E.L. Murphy and R.H. Good [31], and R. D. Young [32, 33].

Modern micro and nano-electronics, rather than vacuum tubes of the original works, has reenergized field emission theory research. G. N. Fursey and Forbes have enhanced the standard F-N theory [28, 29, 34]. Forbes' work specifically has been focused on modernizing and simplifying the F-N theory by separating the physical and mathematical descriptions of the standard theory. Forbes' intended result is to create a theory that can be easily generalized for different potential barriers, while Fursey's published work focuses on deviations of the F-N theory for atomically pointed surfaces.

#### 2.4.1. Fowler-Nordheim Field Emission

Derivations of the field emission theory begin with the calculation of the escape probability  $D$  of an electron approaching the emitter surface in a given electronic state. The final result, the current density  $J$ , is the summation over all occupied states. Forbes *et al's* treatment of field emission theory presented here starts with four assumptions: first, atomic structures are ignored and a Sommerfeld free-electron model is assumed; second, electron distribution is in thermodynamic equilibrium and obeys Fermi-Dirac statistics; third, temperature is zero; and fourth, the planar emitter surface is flat and has a constant uniform local work function with a uniform electric field on the outside [29]. The escape probability  $D$  is given by (2.7).

$$D \approx \exp[-G] \quad (2.7)$$

Where  $G$  is the Jefferies-Wentzel-Kramers-Brillouin (JWKB) integral found in (2.8).

$$G \equiv g_e \int M^{1/2} dz \quad (2.8)$$

In (2.8),  $g_e$  is the JWKB constant and  $z$  is the distance from the emitter's surface.  $M(z)$  defines the barrier shape and is referred to as the motive energy. Integration about the zeros of  $M(z)$  yields a quantity for  $G$  found in equation (2.9).

$$G \equiv \nu \frac{bh^{3/2}}{F} \quad (2.9)$$

Where  $\nu$  is a physical tunneling-exponent correction,  $b$  is the second F-N constant,  $h$  is the unreduced barrier height, and  $F$  is the barrier field at the emitter surface. For an elementary triangular barrier, where  $M(z) = h - eFz$ , the JKWB constant in equation (2.10) can be found.

$$G_{el} \equiv \frac{bh^{3/2}}{F} \quad (2.10)$$

This allows other barriers to be derived from the elementary barrier by applying the tunneling-exponent correction. A decay rate factor  $\tau$  can be defined by a partial derivative, equation (2.11) at a constant barrier field  $F$ .

$$\left( \frac{\delta G}{\delta h} \right)_F \equiv \tau \left( \frac{\delta G_{el}}{\delta h} \right)_F \quad (2.11)$$

From which  $\tau$  can be shown as (2.12)

$$\tau = \nu + \left( \frac{2}{3} \right) h \left( \frac{\delta \nu}{\delta h} \right)_F \quad (2.12)$$

By summing over all states on a spherical constant total energy surface and integrating with respect to total electron energy Forbes (Forbes 2004) was able to show the current density in (2.13)

$$J = [\tau_F^{-2} a \phi^{-1} F^2] \exp[-\nu_F b \phi^{3/2} / F] \quad (2.13)$$

Where  $\tau_F$  and  $V_F$  represent the values of  $\tau$  and  $v$  that apply to  $h=\phi$ , where  $\phi$  is the metal work function, and  $a$  is the first F-N constant. To achieve the F-N equation for an elementary triangle barrier, the correction factors  $\tau_F$  and  $V_F$  are set to unity, and the current density  $J$  is converted to current  $I$  by multiplying both sides to by the area  $A$  resulting in (2.14).

$$I = [Aa\phi^{-1}F^2] \exp[b\phi^{3/2} / F] \quad (2.14)$$

Equation (2.15) can be found by dividing by the applied electric field  $F$  and taking the natural log of both sides.

$$\ln(I / F^2) = (-b\phi^{3/2} / F) + \ln(Aa\phi^{-1}) \quad (2.15)$$

An alternative expression of (2.15) is obtained by utilizing the equation for the electric field,  $F=V/d$ , which results in (2.16).

$$\ln(I / V^2) = (-b\phi^{3/2}d / V) + \ln(Aa\phi^{-1}d^{-2}) \quad (2.16)$$

The expression in (2.16) is the common representation of the F-N equations. The resultant plot from (2.16), like that found in the inset of Figure 17 [35], is commonly referred to as the F-N plot, and is a convenient way to analyze collected experimental data [35]. A directly proportional dependence between the logarithm of a ratio  $I/V^2$  and the inverse of the applied field of voltage  $I/V$  indicates the mechanism of the electron emission as it relates to field emission [36]. For qualitative analysis of the F-N plot, a linear relationship indicates field emission, while non-linear indicates thermionic emission. The F-N plot is also useful in calculating the field enhancement factor.

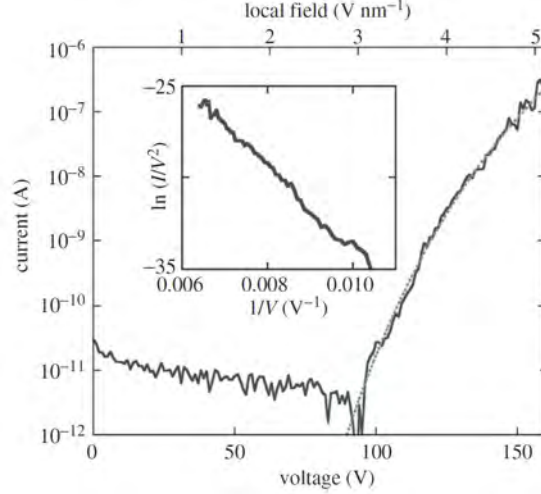


**Figure 17 – IV curve of a field emitter. The linear F-N plot, in the inset, indicates the electron emission is from field emission**

#### 2.4.2. Field Enhancement Factor

The field enhancement factor  $\beta$  in (2.17) is the ratio between the local electric field  $F$  at the tip of an emitter to the applied electric field  $F_0$  [36].

$$\beta = \frac{F}{F_0} = \frac{Fd}{V} \quad (2.17)$$

Field enhancement is caused by micro or nanoprotusions out of an emitting surface. CNTs in particular, have an electric field strength  $F$  at the tip is many times higher than that of the applied field  $F_0$  [36]. An expression for the relationship between the height  $h$  and base radius  $R$  to field enhancement factor is given in (2.18) [36].

$$\beta = \frac{h}{d} \left( 1 + \frac{d}{D} \right) \quad (2.18)$$

Both (2.17) and (2.18) correspond only to models of a hemisphere on a cylinder which is ideal for a CNT with a smooth hemispherical cap. A change in tip configuration can also change  $\beta$ . This effect can be seen by the comparison of different tip configurations in

Figure 18. The comparison shows that the smaller the radius of the tip the better the field enhancement factor [37].

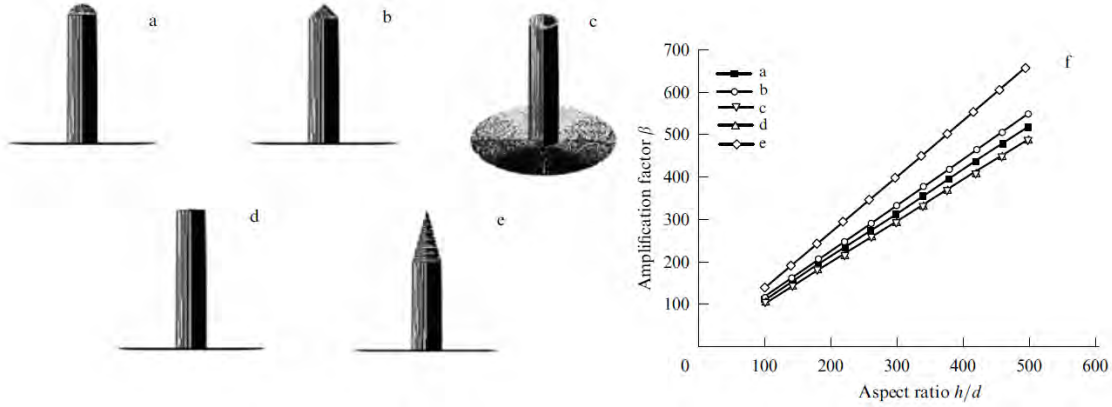


**Figure 18 – Comparison of tip features and resulting field enhancement factor with respect to the emitter's aspect ratio [37]**

The field enhancement factor  $\beta$  is determined first by substituting (2.17) into (2.16) to yield the F-N equation in terms of  $\beta$  in (2.19).

$$\ln(I/V^2) = \left( \frac{-b\phi^{3/2}d}{\beta V} \right) + \ln\left( \frac{Aa\beta^2}{\phi d^2} \right) \quad (2.19)$$

As discussed previously, the relationship between  $\ln(I/V^2)$  and  $I/V$  is linear for field emission. An examination of (2.19) reveals the equation in slope-intercept form or  $y = Mx+B$ . The slope and intercept can then be defined as equation (2.20) and (2.21).

$$M = \frac{-b\phi^{3/2}d}{\beta} \quad (2.20)$$

$$B = \ln\left( \frac{Aa\beta^2}{\phi d^2} \right) \quad (2.21)$$

The first and second F-N constants,  $a$  and  $b$ , are determined by the universal constants in equations (2.22) and (2.23), where  $e$  is the elementary positive charge,  $m_e$  is the electron mass, and  $h_p$  is Planck's constant.

$$a = \frac{e^3}{8\pi h_p} = 1.54 \times 10^{-6} \text{ A eV V}^{-2} \quad (2.22)$$

$$b = \frac{(8\pi/3)(2m_e)^{1/2}}{eh_p} = 6.83 \times 10^{-7} \text{ V eV}^{-3/2} \text{ cm}^{-1} \quad (2.23)$$

Using a line interpolation of the F-N plot, like that found in Figure 17, the slope and intercept of the line can be found. The field enhancement factor can be found by utilizing the interpolated slope, experimental parameters for emission area  $A$  and emitter surface to anode distance  $d$ , and the work function for the CNT  $\phi$ . Experimental data for various typed of CNTs and CNT surfaces are presented later.

### 2.4.3. Deviation for Nanoscale Tips

The nanoscale tips found on CNTs result in a deviation in the typical planar F-N criteria [38]. Field emitters with nanoscale tips having radii of curvature equal to or less than the potential barrier width result in a notable deviation from the one-dimensional planar barrier and field uniformity model [38]. The solution to the three dimensional Schrödinger equation is required for the asymmetrical potential barrier presented by the nanoscale tips [38]. Using a spherical-symmetric model, Fursey *et al* gave the potential dependence upon the distance  $x$  as equation (2.24).

$$U(x) = -\frac{e^2}{4x} - eF_0 R_e \left( \frac{x}{x + R_e} \right) + E_F + \varphi \quad (2.24)$$

Where  $F_0$  is the field strength on the emitting surface and  $R_e$  is the apex radius curvature. Fursey *et al*'s numerical solution deviation is compared to the 'traditional' F-N criteria for radii of 40 Å and 80 Å in Figure 19 [34], where the decrease of current density  $J$  for the same value of  $F_0$  is more significant for smaller values of  $R_e$  [38].

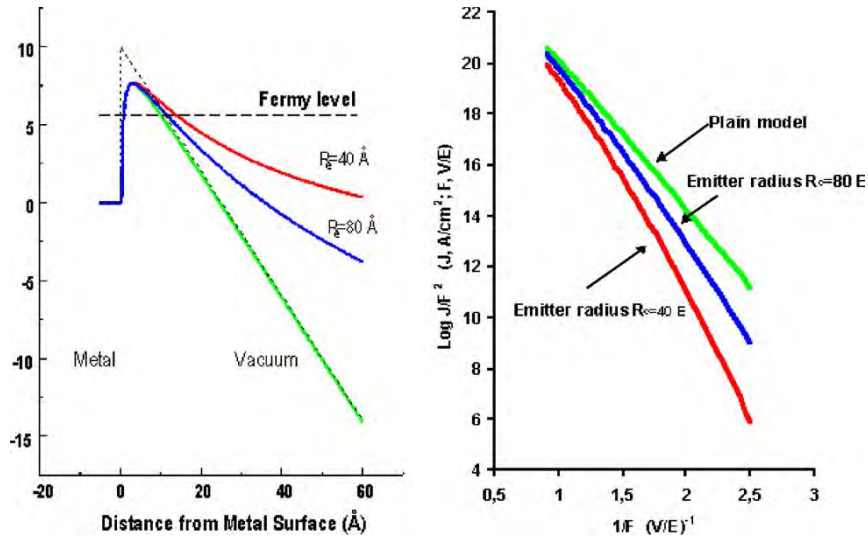


**Figure 19 – Comparison between Fursey *et al*'s numerical solution to the F-N equation compared to the traditional F-N criteria for emitter tip radii of 40 and 80 Å [39]**

#### 2.4.4. CNT Field Emission and Issues

Carbon nanotubes have unique properties that make them ideal field emission sources. These unique properties include high aspect ratio, excellent conductivity, and high temperature stability. Although both SWCNTs and MWCNT have shown field emission properties, MWCNTs are better suited for field emission. The improved field emission performance in MWCNTs is due to their robustness, stiffness, and semi-metallic nature when compared to SWCNTs.

In comparison to a metallic emitter which experiences thermal runaway at high temperatures, the semi-metallic nature of CNTs makes them robust emitters at high temperatures. MWCNTs have demonstrated that they can be heated by field emission current up to 2000 K and remain stable. In metals, the resistance increases with temperature, which corresponds to more heat,  $Q$ , produced as current,  $I$ , increases. The high temperature and electric field results in surface diffusion causing field sharpening of the emitter tips. Tip sharpening further increases the electric field, current, and

temperature. This corresponding relationship between  $Q$  and  $I$  causes a positive feedback mechanism resulting in unstable thermal runaway. In CNTs, the resistance of CNT decreases with temperature limiting  $I^2R$  heat generation [40].

#### 2.4.4.1. Early Field Emission Tests

CNTs as an electron source for electrons guns were demonstrated by de Heer *et al* in 1995. (de Heer 1995). The electron source, as shown in Figure 20, consisted of a purified CNT film formed by an arc discharge method and pressed on a PTFE sheet. A perforated mica sheet was bonded to the CNT film and covered with a copper grid [41].

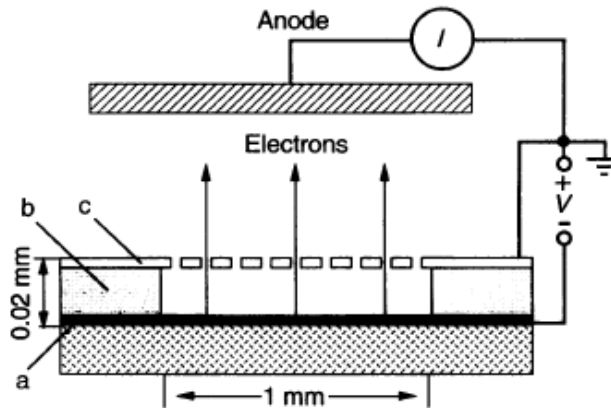


**Figure 20 – de Heer *et al* electron source consisting of a purified CNT film formed by an arc discharge method and pressed on a PTFE sheet, and a perforated mica sheet bonded to the CNT film and covered with a copper grid [41]**

In this configuration, the device functions as a diode with no current detectable under reverse bias. Electron beams with energies near 400 eV produced by this source were deflected with a radii of about 1 cm by a 10 G magnetic field. This deflection confirmed that the current was carried by electrons rather than ions which have a deflection two orders of magnitude smaller [41].

The emission characteristics for this device were determined from the current measurements taken at 1 cm from the top of the grid. The results are presented in Figure

21. The insert in Figure 21 shows a linear F-N plot, which confirms the current being the result of field emission. de Heer *et al*'s analysis of the F-N plot yielded a field enhancement factor of 1300 [41].

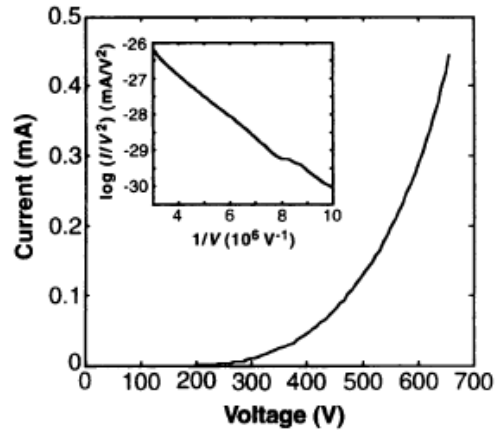


**Figure 21 – IV curve and F-N plot of data collected by de Heer from the setup described by Figure 20 [41]**

Bonard *et al* studied the field emission of both SWNT and MWNT films. Like de Heer *et al*, Bonard *et al* used an arc discharge method to produce the CNT. The SWNTs were suspended in solution and deposited on copper or brass platelets covered with Teflon at a density of  $\sim 10^8$  cm<sup>-2</sup> as shown in Figure 22 [42]. Field emission measurements were made under  $\sim 10^7$  mbar utilizing a 3mm cylindrical counter-electrode placed 125  $\mu$ m above the film surface [42]. The measurement setup is shown in Figure 22.

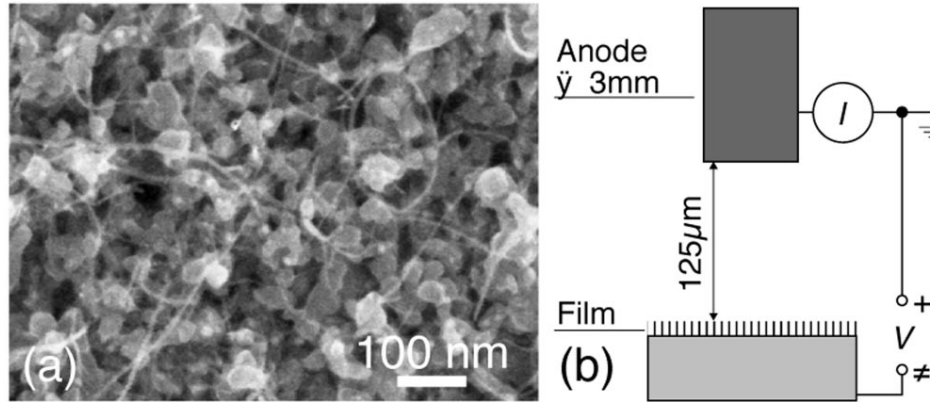


**Figure 22 – (a) SWCNTs deposited on copper or brass platelets at a density of  $\sim 10^8 \text{ cm}^{-2}$ ; (b) Field emission measurement setup [42]**

For all measurements, Bonard *et al* found stable and reproducible behavior with a constant F-N slope up to  $\sim 0.1 - 1 \mu\text{A cm}^{-2}$  for consecutive measurements. Figure 23 shows a single ramp I-V characteristic of a SWNT film. The inset in the figure is the F-N plot for the same data. Bonard *et al* found at higher currents the F-N slope decreased between 10% - 50%. This decrease is indicated by (a) in the inset of Figure 23. They also found saturation above  $\sim 10 - 100 \mu\text{A cm}^{-2}$  by observing the F-N slope diminishing by a factor of 3 as indicated by (b) in Figure 23 [43].

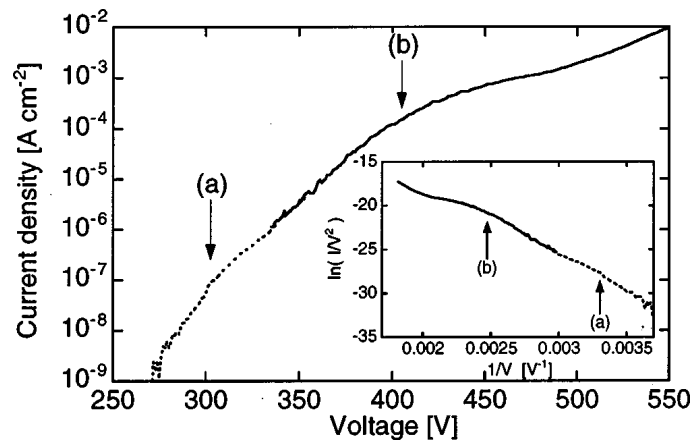


**Figure 23 – I-V curves and F-N plot from emission testing of SWNT films by Bonard *et al* [42]**

From the F-N slopes at low currents, Bonard *et al* estimated field enhancement factors of  $\beta = 3600$ , with values between  $\beta = 2500$  and  $\beta = 10,000$ . The turn on field ( $E_{to}$ ) and threshold field ( $E_{thr}$ ) required to produce currents of  $10 \mu\text{A cm}^{-2}$  and  $10 \text{mA cm}^{-2}$  were measured at  $E_{to} = 1.5 - 4.5 \text{ V}/\mu\text{m}$  and  $E_{thr} = 3.9 \text{ V}/\mu\text{m} - 7.8 \text{ V}/\mu\text{m}$  with an average value over all devices of  $E_{to} = 2.8 \text{ V}/\mu\text{m}$  and  $E_{thr} = 5.2 \text{ V}/\mu\text{m}$  [42].

Using a similar method, Bonard *et al* also investigated field emission from both a single MWNT and MWNT films [43]. For the single MWNT characterization, single MWNTs were mounted on a 20  $\mu\text{m}$  diameter gold wire which was etched to a 250 nm tip. The MWNTs are held to the tip by Van der Waals forces. The gold tip has multiple MWNTs attached; however Bonard *et al* state that the second-best placed tubes would not provide enough current to influence the measurement. The MWNT film was produced the arc-discharge method and deposited on platelets [42], with a resultant CNT density of  $\sim 10^9 \text{ cm}^{-2}$ . An example of the single MWNT on the gold tip and MWNT film along with the test setup diagram are provided in Figure 24.

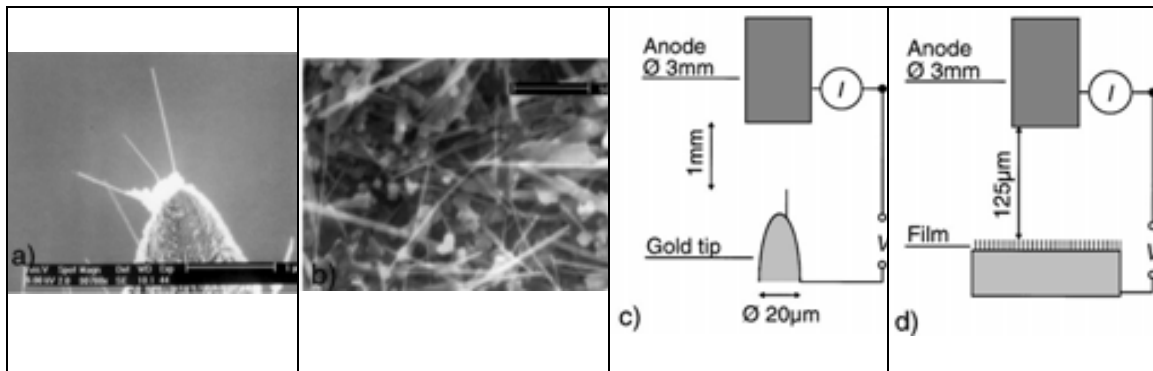


**Figure 24 – (a) MWNTs attached to a 250 nm gold tip, (b) MWNTs deposited on copper plate, (c) measurement setup of single MWNT, and (d) setup for MWNT film [43]**

The experimental I-V plots and corresponding F-N plots in Figure 25 show that the CNTs I-V characteristics followed F-N behavior at low currents with single MWNT tips having constant currents below  $\sim 10\text{-}20$  nA and MWNT films having constant current densities up to  $0.1 - 10 \mu\text{A cm}^{-2}$ . Bonard *et al* observed a 10-30% change in slope of the F-N plot at higher currents for both MWNT tips and MWNT films.

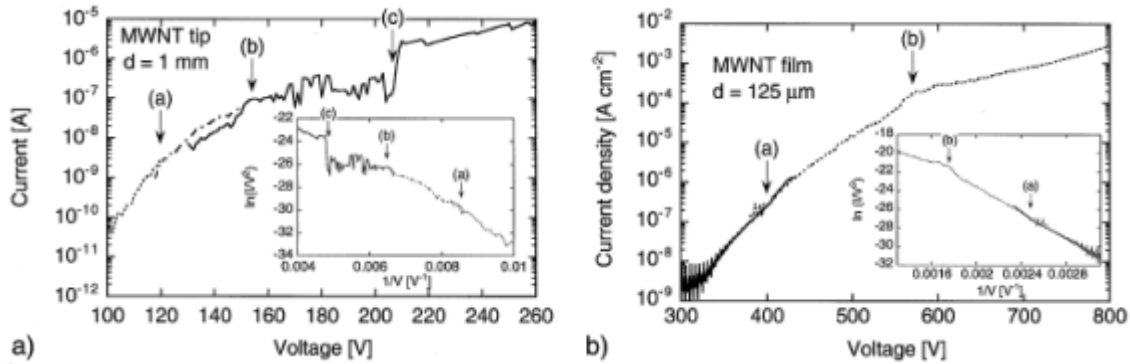


**Figure 25 – Experimental IV curves for (a) single MWNT and (b) MWNT films, insets show F-N plot [43]**

Using the slope in the low current region and assuming  $\phi = 5$  eV, Bonard *et al* determined field amplification factors ranging from  $\beta = 30,000$  to  $50,000$  for MWNT tips and  $\beta = 1000$  to  $3000$  for MWNT films [43]. They found for MWNT tips a currents of 1 mA were obtained at 250 V and the turn on field and threshold field to be  $E_{to} = 2.6$  V/ $\mu\text{m}$  and  $E_{thr} = 4.6$  V/ $\mu\text{m}$  respectively for MWNT films [43].

Deviations from the F-N criteria observed by Bonard *et al* in [42] and [43] were originally attributed to space-charge effects which decrease the F-N slope and consequently decrease the field enhancement factor. However Nilsson *et al* concluded after experimentation that the reduced field emission behavior is a combination of two effects. In high density film, the reduced emission is explained by electrostatic screening

caused by the relative proximity of neighboring emitters [44]. In low density films, specifically those used in Nilsson *et al*, the CNTs are short, bent, and do not protrude significantly from the surface. As a result, only a fraction have sufficient field emission factor for measurable field emission.

#### **2.4.4.2. Field Emission Screening**

The samples in Nilsson *et al*'s experiment were measured with a FE apparatus that integrated FE using a phosphor screen and locally resolved FE using a X/Y-scanning tip. Screen artifacts were minimized by maintaining a constant 3000 V and changing the field by adjusting the screen-cathode distance. A 2-5  $\mu\text{m}$  tip for X/Y scanning was biased at 100 V with scanning performed over a 200 x 200  $\mu\text{m}^2$  area divided into 100 x 100 pixels. The tip was kept at a distance of 3-5  $\mu\text{m}$  above the CNT surface. Nilsson *et al*'s integrated measurements on patterned samples with different CNT densities did not show significant differences in their field emission [44]. They found, as shown by the inset in Figure 26, that the emission was dominated by a relatively few strong emitters distributed throughout the sample, and concluded that emitters with lower length-to-diameter ratio or lower field amplification factors are not detected. By decreasing the measured surface, they found that it was possible to identify many emitters with  $\beta \sim 100$ -200 compared to finding only a few strong emitters with  $\beta \sim 1000$  for larger measurement sites. This revelation led Nilsson *et al* to perform further measurement which identified large differences in their samples.

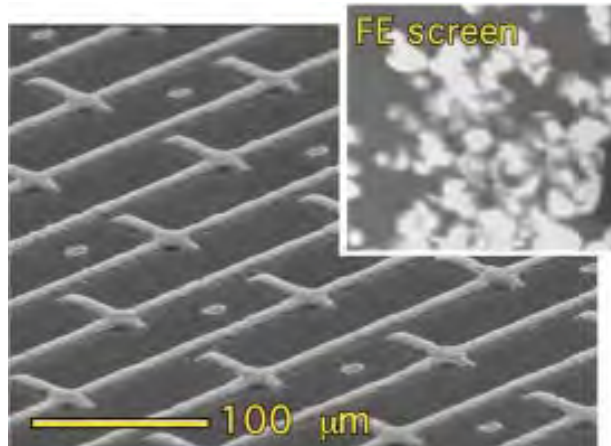


**Figure 26 – SEM image of Nilsson *et al* patterned CNTs, (inset) field emission intensity shown on a phosphor screen [44]**

Utilizing FE scans of patterned samples with different CNT densities, they found that a medium density CNT pattern produced the best emission image, as shown in Figure 27, when compared to low density and high density CNT patterns [44]. These scans led to Nilsson *et al*'s conclusion about high density and low density film highlighted above.

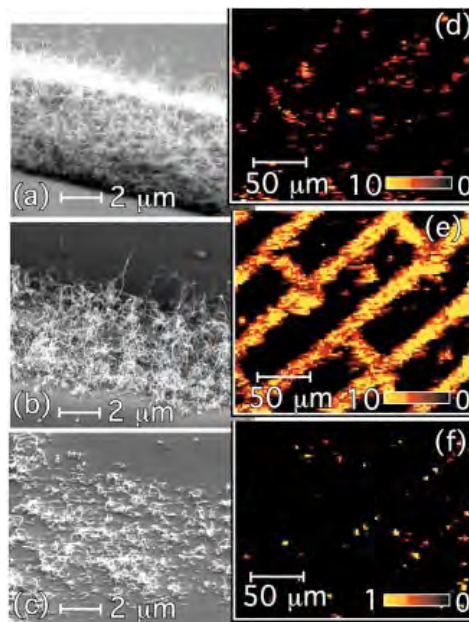


**Figure 27 – FE scans of different density of CNTs showing medium density with the best results [44]**

Nilsson *et al* verified their experimental findings by performing electrostatic calculations of the field penetration between parallel standing tubes, shown in Figure 28a. The calculations showed that a change in the intertube distance affected the equipotential lines and consequently the field emission factor  $\beta$ . Figure 28b from [44] shows  $\beta$  as a function of intertube distance also with the emitter density. Utilizing  $\beta$  and the emitter density within the F-N equation, Nilsson *et al* were able to plot the current density as a function of the distance and applied electric macroscopic field as shown in Figure 28c. From the specified experimental parameter of a 1  $\mu\text{m}$  emitter height, they found an optimal emitter spacing of 2  $\mu\text{m}$ , leading to their conclusion of an intertube distance of about twice the height of the CNTs optimizes the emitter current per unit area [44].

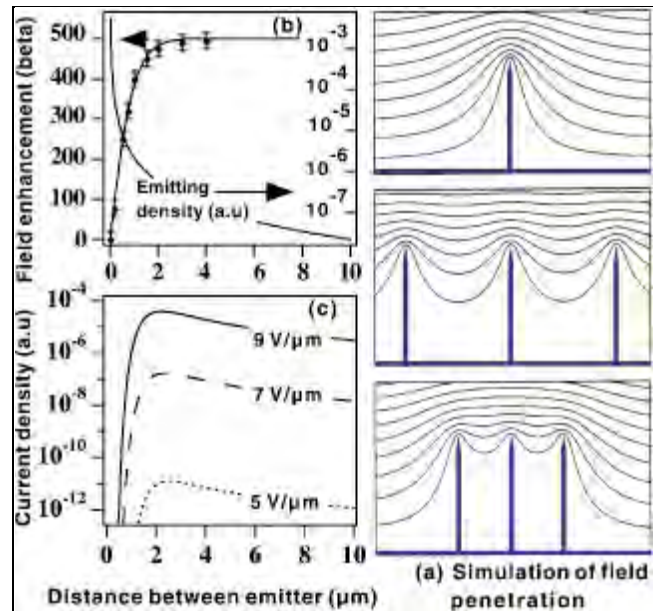


**Figure 28 – Electrostatic calculations on inter-emitter spacing showing the effects of spacing on current density and field enhancement [44]**

By maintaining the tube diameter and intertube spacing and varying the height of the CNTs, Suh *et al* experimentally showed that the field enhancement factor was greatest when the CNT height was comparable to the intertube distance which contradicts

Nilsson *et al* two-to-one intertube to height ratio. Figure 29a and Figure 29b show the I-V and F-N plots from varying the tube height for both 38 nm and 19 nm diameter CNTs [45]. Figure 29c shows field enhancement factor as a function of tip height for constant CNT spacing of 104 and 65 nm. Suh *et al* state that the field emission is affected by the tube height protruding from the surface and the field enhancement factor is very low when the CNT height is very small [45].

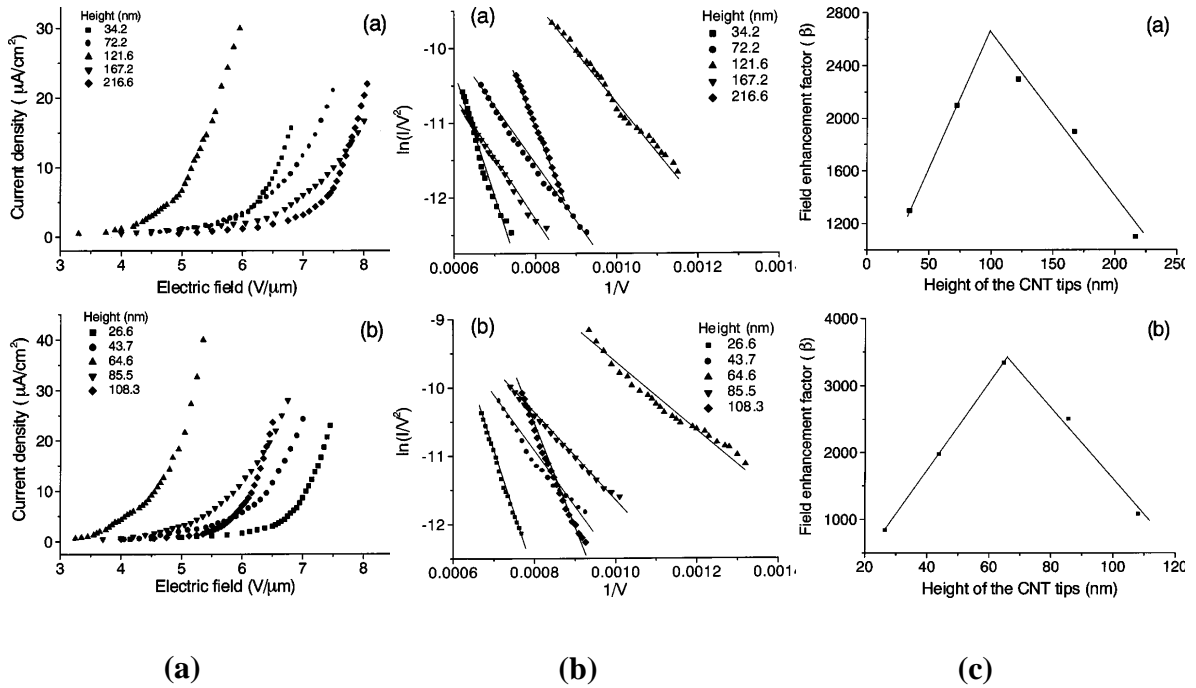


**Figure 29 – (a) and (b) Current density and F-N plots for various CNT heights and diameters of 38 and 19 nm; (c) Field enhancement factors against a variable heights of CNTs at constant spacing of 104 and 65 nm [45]**

Chen *et al* and Smith *et al et al* are just a few that have performed simulations on the effects of intertube spacing on field emission screening [12, 46]. Like Nilsson *et al*, Chen *et al*'s models are done in 2D, meaning that the modeled emitters are only affected by neighboring emitters to the left and right [12]. While Smith *et al* perform modeling utilizing 3D array models [46].

In their model, Chen *et al* simulated the field emission of an array of SWCNTs with a quantum and molecular method. The simulation assumes a SWCNT with a specified (5, 5) armchair type with the dangling bonds in the open mouths of the SWCNTs saturated with hydrogen atoms. All SWCNTs are uniformly vertically mounted on a metal surface. The WKB approximation for the transmission coefficient ( $D$ ) given by (2.25), with  $U(z)$  as the electron potential,  $E_F$  the Fermi energy, and the integral over the forbidden region where  $U(z)-E_F>0$ . Utilizing  $D$  yields the emission current ( $I$ ) for the individual SWCNTs can be estimated by (2.26)() where  $q_{exc}$  are the extra electrons of the first layer atoms and  $\nu$  is the collision frequency estimated from the average kinetic energy of  $\pi^*$  electrons as  $E_k(\pi^*)/h$  [12]. (Chen 2007)

$$D = \exp \left[ -\frac{2}{\hbar} \int \sqrt{2m[U(z) - E_F]} dz \right] \quad (2.25)$$

$$I = \nu q_{exc} D \quad (2.26)$$

Chen *et al* plotted the simulated current density against the intertube density for varying applied fields and SWCNT lengths in Figure 30. The figure shows that current density is very sensitive to both the SWCNT length and the applied field. The plots also show that emission turn-on occurs at a certain intertube spacing, shown to be approximately equal to the SWCNT lengths. It could also be deduced from these plots that the turn-on spacing and the maximum current density both depend on the applied field.

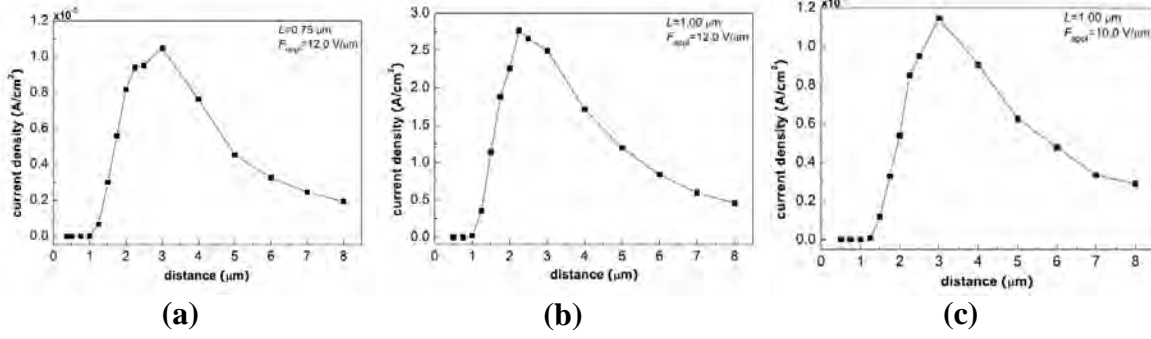


**Figure 30 – Simulated current density against the intertube density for varying applied fields and SWCNT lengths: (a)  $L = 0.75 \mu\text{m}$ ,  $F_{\text{app}} = 12.0 \text{ V}/\mu\text{m}$ ; (b)  $L = 1.00 \mu\text{m}$ ,  $F_{\text{app}} = 12.0 \text{ V}/\mu\text{m}$ ; and (c)  $L = 1.00 \mu\text{m}$ ,  $F_{\text{app}} = 10.0 \text{ V}/\mu\text{m}$  [12]**

However, Chen *et al* performed further analysis of the screening effect to deduce the effects of both the intertube distance and the applied field. In this analysis Chen *et al* defined a screening factor by (2.27).

$$\alpha = 1 - \frac{V}{LF_{\text{appl}}} \quad (2.27)$$

In (2.27),  $V$  is the voltage drop at the middle point of the line connecting two neighboring apexes, and should be zero with no screening effects and one when the array acts as an ideal metal layer of thickness  $L$  and screens the field completely. Plotting  $\alpha$  as a function  $d/L$  for different values of  $L$ ,  $d$ , and  $F_{\text{appl}}$ , Chen *et al* show in Figure 31a that variations of the parameters do not significantly change the curve. Hence, Chen *et al* imply that the screening factor is a function of  $d/L$ . By fixing  $d$  and  $L$  and varying  $F_{\text{appl}}$ , Chen *et al* show, by plotting  $\alpha$  against  $F_{\text{appl}}$  in Figure 31b, that a change in the applied field does not affect their screening factor implying that the screening factor fixed by the ratio  $d/L$  is an intrinsic feature of the array.

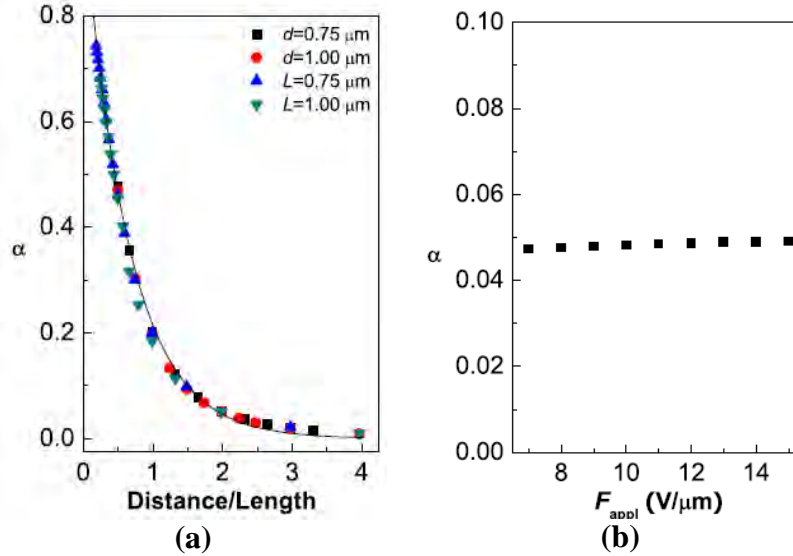


**Figure 31 – Using a defined screening factor  $\alpha$ , (a) and (b) show that variations in  $L$ ,  $d$ , and  $F_{\text{appl}}$  have little effect on the curves and hence  $\alpha$**

Chen *et al* provide further evidence to show correlation between  $\beta$  and emitter length and their screening factor. They found that for larger spacing distances, the current density increases rapidly as the length increased until the length is approximately 1.5 times the spacing distance, and for longer length emitters the current density only increased slowly. This would infer that lengths of the SWCNTs of an array do not need to be very long [12].

Smith *et al* performed modeling and simulation for 3D CNT arrays to determine an optimal intertube spacing to minimize field emission screening [46]. The basic 2D model for their simulation is given in Figure 32. In Figure 32, the vertically aligned CNTs of uniform height  $h$  and radius  $r$  are placed on a grounded cathode with separation  $S$  and anode-cathode distance  $D$ .

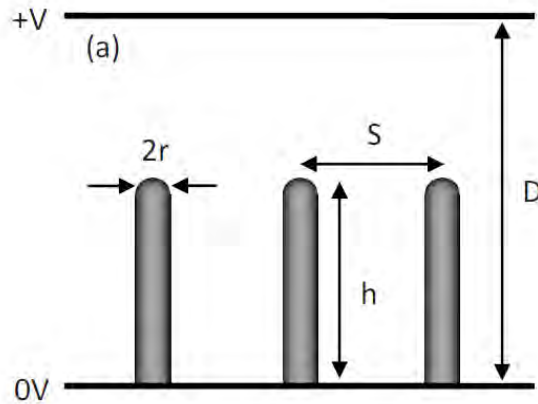


**Figure 32 – Basic 2D model for Smith *et al* simulations of CNT arrays; the vertically aligned CNTs of uniform height  $h$  and radius  $r$  are placed on a grounded cathode with separation  $S$  and anode-cathode distance  $D$  [46]**

In all, Smith *et al* simulated five different 2D conditions to determine the validity of further 3D array models. The first simulation involved placing a single CNT on the simulation workspace, while the other four were utilizing that single CNT with two, four, six, and eight neighbors with a constant intertube spacing of  $3\ \mu\text{m}$ . From these simulations, Smith *et al* observed that the ratio of local fields of the central CNT in the array to the single array varied by only 1.5% for each of the five simulations [46]. After achieving reliable results, they then modeled an array of nine CNTs. The contour plot in Figure 33 is from the sample modeled using the following characteristics: nine CNT array with spacing  $S$  of  $3\ \mu\text{m}$ , height  $h$  of  $3\ \mu\text{m}$ , radius of  $50\ \text{nm}$ , and anode-cathode spacing of  $80\ \mu\text{m}$  with a positive  $100\text{V}$  potential. Figure 33 shows a reduced field strength of approximately 15% between the center emitters and the emitters on the edge [46]. The emission at the tips of the corner CNTs were 8.6% lower than isolated control CNT.

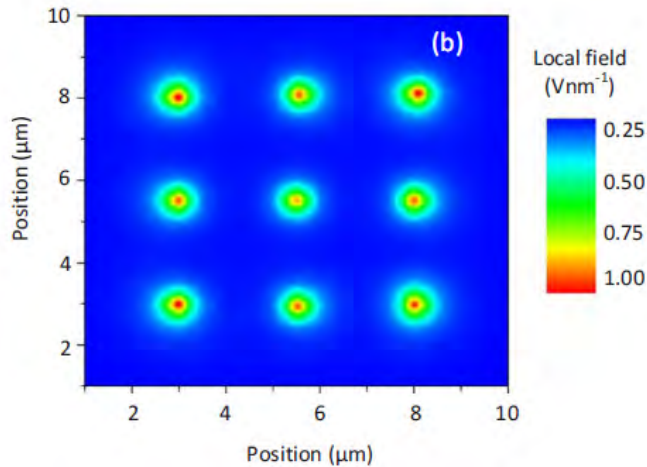


**Figure 33 – Contour plot from a nine CNT array with spacing  $S$  of  $3 \mu\text{m}$ , height  $h$  of  $3 \mu\text{m}$ , radius of  $50 \text{ nm}$ , and anode-cathode spacing of  $80 \mu\text{m}$  with a positive  $100\text{V}$  potential showing a drop of approximately  $15\%$  between the center emitters and the emitters on the edge [46]**

Smith et al also performed simulations on arrays of  $3 \times 3$ ,  $7 \times 7$ , and  $11 \times 11$  with constant heights and radius with a varied spacing ranging from  $S=0.3h$  to  $S=5.3h$  [46]. The results, plotted in Figure 34, show for the assumed optimal spacing of  $S=2h$  a decrease of  $11\%$  for the center CNT. A linear array was simulated to mimic work of Nilsson *et al* and has a screening of around  $2\%$ .

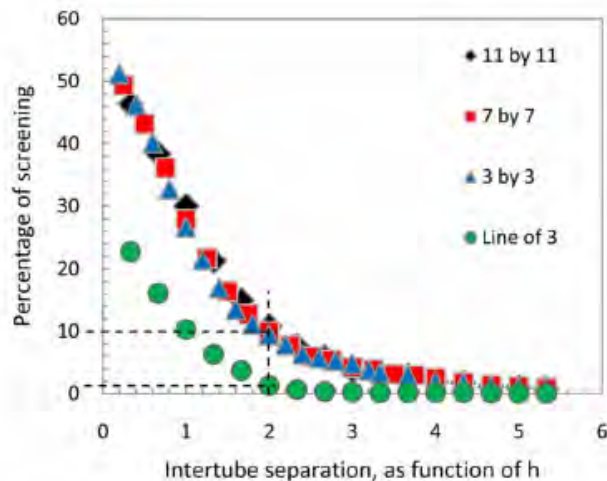


**Figure 34 – Simulations on arrays of  $3 \times 3$ ,  $7 \times 7$ , and  $11 \times 11$  with constant heights and radius with a varied spacing ranging from  $S=0.3h$  to  $S=5.3$ , showing for the assumed optimal spacing of  $S=2h$  a decrease of  $11\%$  for the center CNT [46]**

To further study the impact of screening, Smith *et al* took CNT dimensions and FE performance from their previous work, and modeled an array with a constant area of 5 mm<sup>2</sup> and varying intertube spacing. Smith *et al* substituted the local electric field,  $E_L$ , in place of  $bE$  in the standard F-N equation to yield equation (2.28) below.

$$I_0 = \frac{aAE_L^2}{\phi} \exp\left(\frac{-b\phi^{3/2}}{E_L}\right) \quad (2.28)$$

They compare the ratio of the local electric field of the isolated CNT and a CNT in an array, given by  $E_{Lisolated}$  and  $E_{Lscreened}$  respectively in equation (2.29), where S screening percentage.

$$E_{Lisolated} = SE_{Lscreened} \quad (2.29)$$

The ratio between the isolated emission current and the screened emission current yields equation (2.30),

$$\frac{I_{screened}}{I_{isolated}} = S^2 \exp\left[\left(\frac{-b\phi^{3/2}}{E_{Lisolated}}\right) + \left(\frac{-b\phi^{3/2}}{E_{Lscreened}}\right)\right] \quad (2.30)$$

which simplifies to equation (2.31).

$$\frac{I_{screened}}{I_{isolated}} = S^2 \exp\left[\left(\frac{-b\phi^{3/2}}{E_{Lisolated}}\right)\right]^{[(1/S)-1]} \quad (2.31)$$

Smith *et al*, for  $S=2h$  ( $S$  in this case is the intertube distance) and  $S=5h$ , calculated an ordered array of CNTs to be screened by 10% and 2%. Assuming  $I_{Lisolated}$  of 1 mA, Smith *et al* found the screened emission decreased to 177 nA for  $S=2h$ , and 861 nA for  $S=5h$ . By varying the spacing and emission current of a CNT array, Smith *et al* found a sharp increase in the current density as the CNTs become less packed and a maximum current density at an intertube separation of  $3h$ , as shown in Figure 35 [46]. Like Chen *et*

al in [12], Smith *et al* showed that after the peak at  $3h$ , the current density decreased linearly as the CNTs become increasingly unscreened. The same trends are visible in Figure 35 where the emission area is varied. Smith *et al* conclude that to achieve a fully unscreened array that the optimal intertube spacing need to exceed  $S=5h$ , but maximum efficiency can be achieved at  $S=3h$ .

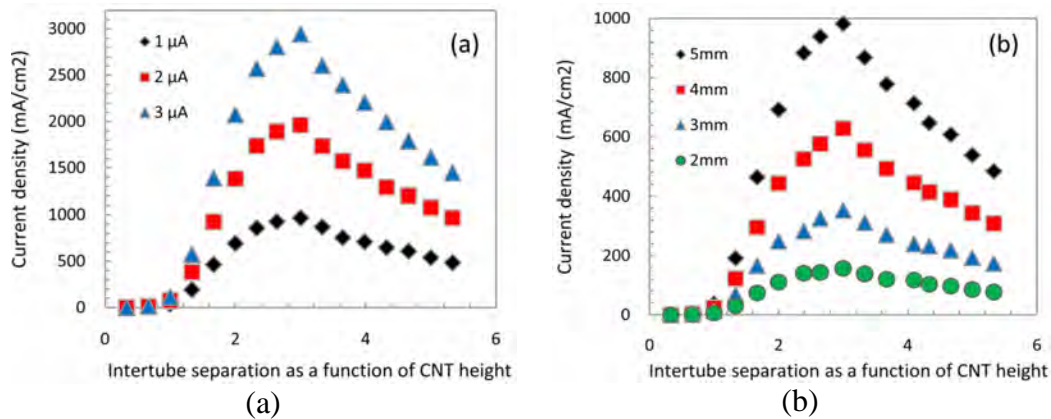


**Figure 35 – Current density as a function of the ratio between intertube separation and height, showing from simulations the optimal current density is obtained when  $S=3h$  [46]**

## 2.5. Patterning of SiC

### 2.5.1. Silicon Carbide Properties

As a result of its structure and material, SiC has excellent mechanical, electrical, and chemical properties. Its mechanical hardness of nine on the Mohs scale falls between topaz (eight) and diamond (ten). SiC also has a wear resistance of 9.15 as compared to 9.00 for  $Al_2O_3$  and 10.0 for diamond [47]. SiC is relatively chemically inert and not easily etched by most acids. It can be wet etched by KOH, but only at molten temperatures above 600 °C [48]. Thermally, SiC does not melt but sublimes near 1800 °C.

Table 2 provides a comparison of semiconductor properties from various materials.

**Table 2 – Semiconductor properties of SiC with other semiconductors [48]**

Property	3C-SiC (6H-SiC)	GaAs	Si	Diamond
Melting Point (°C)	2830 <sup>1</sup>	1238	1415	1400 <sup>2</sup>
Thermal Conductivity (W/cm°C)	5	0.5	1.5	20
Coeff. Thermal Expan. (10 <sup>-6</sup> /°C)	4.2	6.86	2.6	1.0
Young's Modulus (GPa)	448	75	190	1035
Physical Stability	excellent	fair	good	fair
Bandgap (eV)	2.2 (2.9)	1.424	1.12	5.5
Electron Mobility (cm <sup>2</sup> /Vs)	1000 (600)	8500	1500	2200
Hole Mobility (cm <sup>2</sup> /Vs)	40	400	600	1600
Breakdown Voltage (10 <sup>6</sup> V/cm)	4	0.4	0.3	10
Dielectric Constant	9.72	13.1	11.9	5.5

<sup>1</sup> sublimation temperature

<sup>2</sup> phase change temperature

The robustness of SiC has both positives and negatives for patterning and growth of carbon nanotubes by thermal decomposition. Its thermal properties make it an ideal material for CNT growth, since the growth process occurs between 1400 °C and 1700 °C [24]. Its chemical inertness, however, limits the available techniques needed to pattern a SiC wafer.

### 2.5.2. Silicon Carbide Etching

Because SiC cannot be wet etched by most acids other techniques must be used. SiC patterning is commonly obtained by plasma-based dry etching in fluorinated compounds using lithographic masking techniques. Common fluorinated gases used for dry etching include CF<sub>6</sub>, CHF<sub>3</sub>, NF<sub>3</sub>, and SF<sub>6</sub>. Lithographic masking is accomplished using a metallic mask such as Au, Al, Cr, Ni, or indium-tin-oxide [48, 49]. Dry etching is usually accomplished by reactive ion etching or RIE. RIE with fluorinate compounds provides an anisotropic etch. Also RIE etch rates of SiC are low compared to etch rates of Si. The etch rates can be enhanced by combining oxygen with the fluorinated

compound in the plasma [49, 50]. The addition of oxygen to the system effects the etch rate by reacting with the carbon molecules, while the silicon reacts with the fluorine molecules [49]. In addition to the oxygen concentration, the etch rate is effected by the RIE system's RF power, chamber pressure, and gas flow rate [51]. Kothandaraman *et al* found SiC etch rates using SF6 increased with RF power increases and decreased chamber pressures. Conversely, the SiC etch rate decreased as the gas flow rate increased. A table is provided in Appendix B: Silicon Carbide Structure, which summarizes RIE mixtures for select SiC polytypes.

## **Chapter III: Process Development and Experimental Methodology**

This chapter outlines the experimental processes used to characterize the field emission from patterned carbon structures on SiC. These processes include the development of semiconductor processing methods required to create structures from SiC, and the CNT growth procedures used to create the emitter surface. The chapter further discusses the methods used to collect field emission data including the field emission vacuum chambers setup and test apparatus. Finally this chapter will discuss the methodology used for analysis of the collected field emission data.

### **3.1. Pre-CNT Growth Sample Preparation**

The methodology for sample preparation prior to CNT growth followed known semiconductor processing techniques. These known techniques involve metal evaporation, application of a photoresist (PR), ultra-violet (UV) photolithography, metal etching, and PR removal. Further processing steps include reactive-ion etching of the substrate surface and final removal of remaining metal. The result of these steps was a patterned substrate suitable for CNT growth.

#### **3.1.1. Pre-RIE Process**

The first step in sample preparation was the evaporation of nickel onto the substrate surface. Using a Torr® Electron Beam Evaporation System, 2200 Å (22nm) of nickel (Ni) was deposited on a commercially available polished SiC wafer. After the nickel was evaporated onto the samples, the samples are spin coated with a positive photoresist. Initially in this process, 1818 PR was used, however it was found that during Ni etching, it was too thick to identify the level of undercut. As a result, the more translucent and thinner 1805 PR was selected. The 1805 PR is applied to the sample

surface using a spinning technique. The samples are flood coated with 1805PR, then spun at 3000 RPM for thirty seconds, with a 500 RPM spread for 4 seconds and a 200 RPM ramp. After PR application the samples are soft-baked on a hot plate for 120 seconds.

There were three masks utilized in the development of the sample preparation process. One mask with 12  $\mu\text{m}$  features was borrowed from another field emission project. This mask was used to understand the undercut from the nickel etching. Another mask was developed from results found during nickel etching and reduced the spacing between features and had 6  $\mu\text{m}$  features with 3  $\mu\text{m}$  spacing. This mask was found later to be defective due to ghosting caused by vacuum system issues during mask writing. The first and primary mask contained four different minimum features sized ranging from 3  $\mu\text{m}$  and 6  $\mu\text{m}$  circles with spacing equal to twice the circle diameter. The minimum feature size of all masks was dictated by minimum feature size of the Heidelberg Instruments mask maker and the amount of undercut caused by the nickel etchant.

After the application of the 1805 PR, the samples are masked utilizing a SUSS Microtec MJB3 mask aligner. The SUSS was selected because of the non-uniform geometry of the samples and the lack of need for further mask alignments. Samples coated with 1805 PR are exposed for 4 second under a UV lamp. After exposure the samples are developed for 30 seconds using Microdeposit 351 developer mixed at a ratio of 1:5 with deionized water (DI) with 30 second DI rinse and 30 second nitrogen dry. The samples are then inspected for feature size, under/overexposure, and defects. If defects are identified in the photolithography process, the sample can be stripped by

using a combination of acetone, methanol, isopropanol, with a DI rinse and the process started over. If no defects are found in the PR, samples are ready for nickel etching.

Nickel etching was done utilizing Transcene ® TFG Nickel Etchant. Prior to etching, the TFG was heated on a hotplate to 50 °C. Due to varying sample sizes and odd shapes, the samples were held by locking grips. The samples were lowered into the etchant and slowly agitated for a predetermined time. Optical inspection of samples found that an etch time of 2.5 to 2.75 minutes was required to sufficiently etch the nickel through to the substrate. These times were nearly 8 times the expected etch time of 44 seconds provided by the manufacture. After nickel etching, the remaining PR could be removed prior to substrate etching steps. The nickel etching process revealed problems with the substrate. Optical and SEM inspection of the substrate found that the C-face of the SiC was insufficiently polished to identify clear nickel structures. Tests using a profilometer yield a surface roughness very close to the thickness of the evaporated nickel. As a result, it was determined that processing of further substrates should occur on the Si-face of the SiC substrates. At the etch time of 2.5 to 2.75 minutes, the nickel under cut was approximately 1.5 to 2 µm. This finding led to the decision that to obtain usable structures, the minimum feature of the pillars must be equal or greater than 4 µm.

### **3.1.2. RIE Process**

Development of the RIE process began with testing different configurations of masking materials, gas mixtures, flow rates, and etch times to find an optimal REI configuration. The initial tests were conducted utilizing a March Jupiter III RIE. The results of these test gave an indication to the etch rates of both SF<sub>6</sub> and CF<sub>4</sub> with trace amounts of O<sub>2</sub>.

Prior to determining the use of nickel as a masking material, an attempt of masking the SiC with both SU-8 and 1818 photoresists was attempted. The results for the 1818 after 6 minute RIE in a 33:67% CF<sub>4</sub>:O<sub>2</sub> mixture and 200 mW showed that the 1818 was completely removed from the surface. The SU-8 was tested using both SF<sub>6</sub> and CF<sub>4</sub> mixtures. The SU-8 was spun onto the sample to a thickness between 5.5 μm and 6.0 μm, and tested using both SF<sub>6</sub> and CF<sub>4</sub> mixtures. However while testing using the SF<sub>6</sub>, an odorous emanation from the vacuum pump was detected and further testing aborted. The first RIE test using a flow mixture of 20:1 (flow) CF<sub>4</sub>:O<sub>2</sub> at 200 mW for 50 minutes resulted in an etch depth of 0.900 μm. A second test using a flow mixture of 30:1 (flow) CF<sub>4</sub>:O<sub>2</sub> at 250 mW for 40 minutes resulted in an etch depth of 1.0 μm. Using an identical flow mixture and power, etch depths of 1.0 μm and 1.6 μm were found for etch time of 30 minutes and 60 minutes respectively. Typical results from using SU-8 are shown in the SEM image in Figure 36.

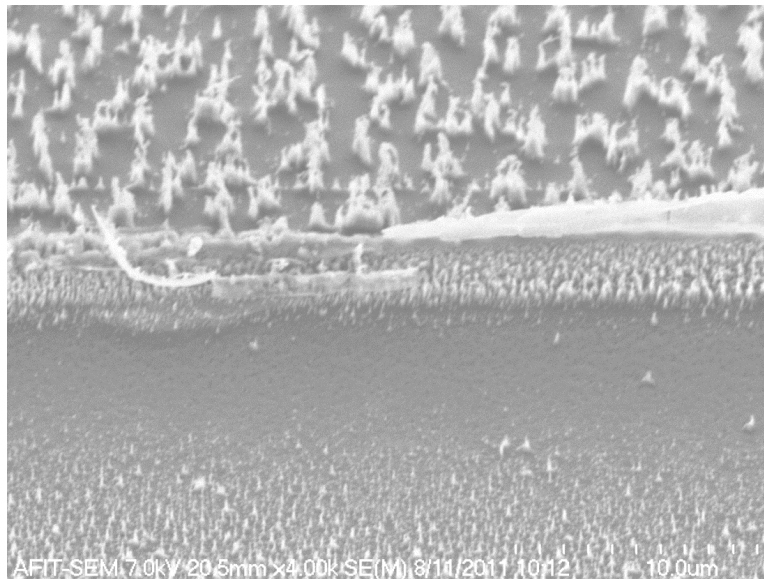


**Figure 36 – SEM image of SiC test sample masked with SU-8**

The nodules or spikes in Figure 36 were originally thought to be remnants of the SU-8. In an attempt to remove these defects the sample above was subjected to an O<sub>2</sub> RIE for ten minutes, followed by soaking the sample in 110 °C 1165 stripper for 30 minutes, and then 10 minute in a plasma asher. The SEM images in Figure 37-Figure 39 show that little to no change in the surface morphology after the post processing steps. Research from Yih *et al* states that the protrusions, thought to be remnants of the mask, are caused by micro-masking caused by the interaction of the plasma with the cathode surface inside the RIE system [50].

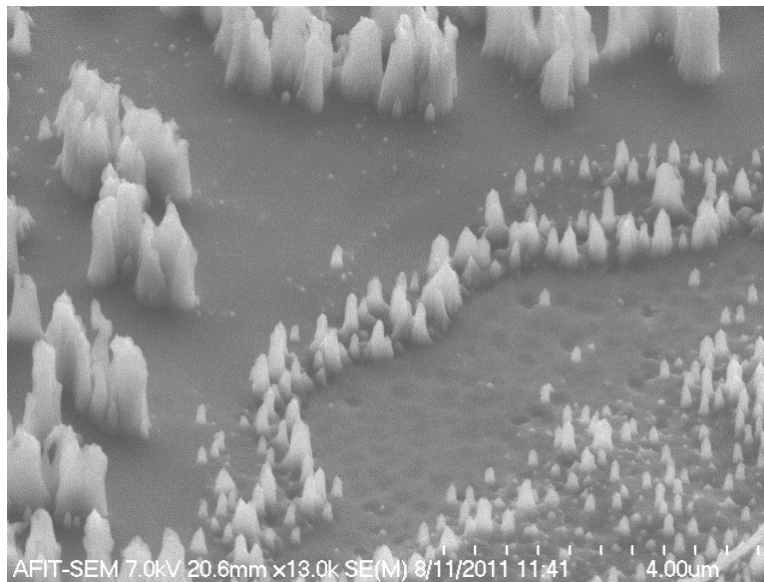


**Figure 37 – SEM of SiC sample after O<sub>2</sub> RIE showing no change in surface texture**

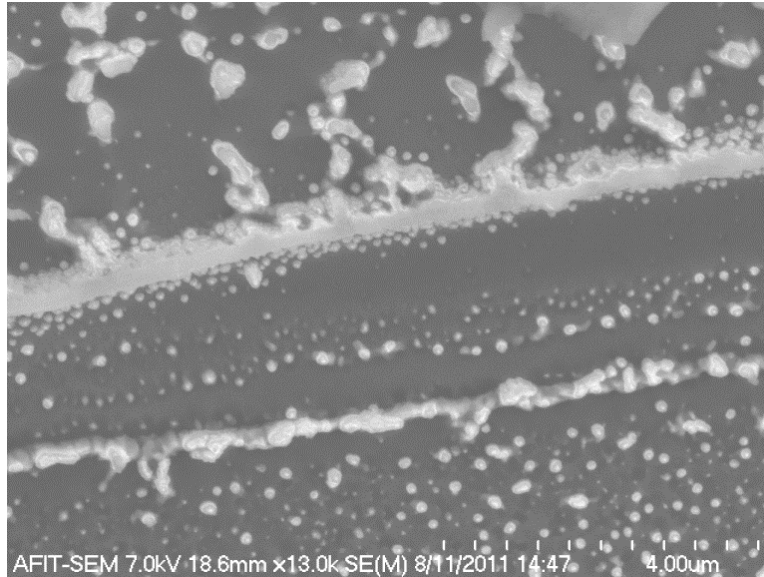


**Figure 38 - SEM of SiC sample after O<sub>2</sub> RIE and 10 minute soak in 110 C 1165 stripper showing no change in surface texture**

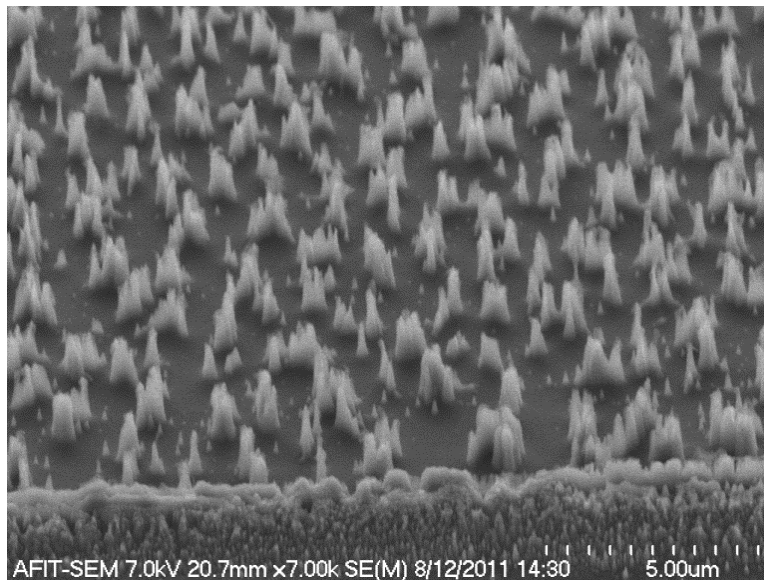


**Figure 39 - SEM of SiC sample after O<sub>2</sub> RIE, 10 minute soak in 110 C 1165 stripper and 10 minutes in plasma asher showing no change in surface texture**

To determine the nickel patterning process, two different methods were used. The first method used metal liftoff. The results from this method showed overexposure of small features during the deep UV exposure step. As such, a second method of post patterning the nickel after evaporation was utilized in this work. Three samples were

etched at a flow rate of 30:1  $\text{CF}_4:\text{O}_2$  at 250 mW for a period of 30, 60, and 90 minutes using a nickel mask. The etch depths were determined to be between 1.47 and 2.3  $\mu\text{m}$  by using the SEM images in Figure 40-Figure 42 below.

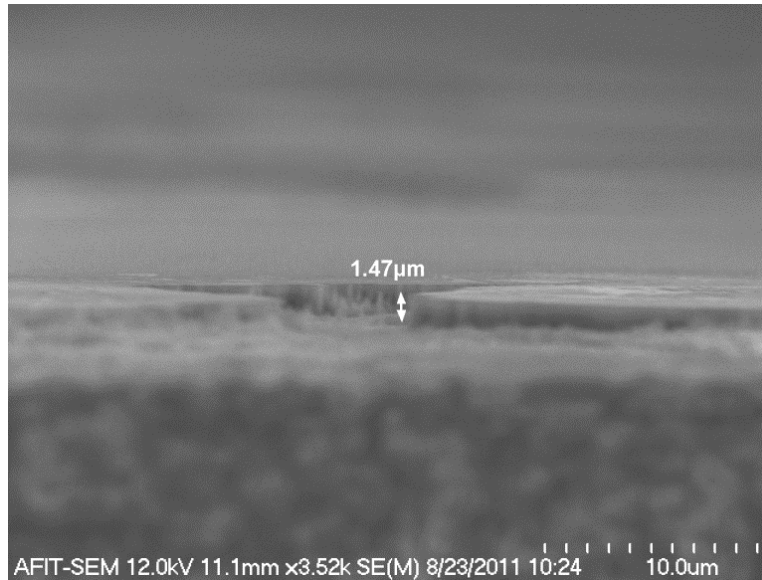


**Figure 40 – SEM image of SiC test piece RIE etched at a flow rate of 30:1  $\text{CF}_4:\text{O}_2$  at 250mW for 30 minutes**

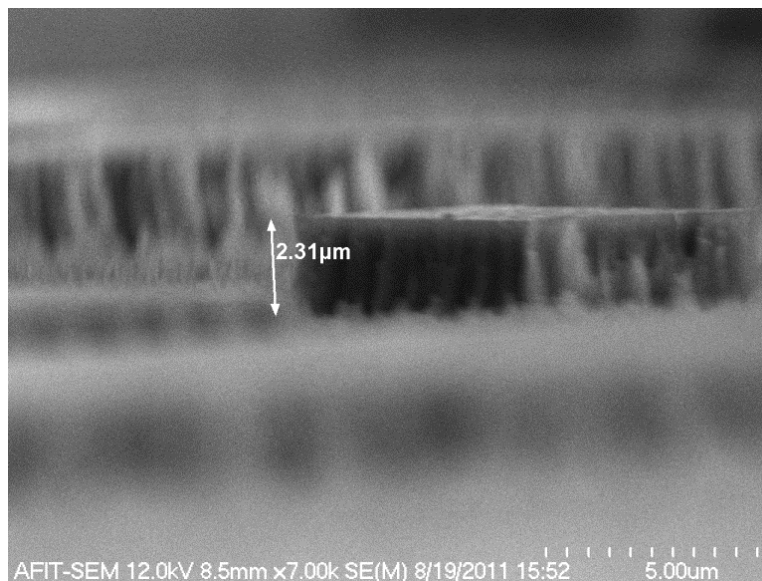


**Figure 41 - SEM image of SiC test piece etched at a flow rate of 30:1  $\text{CF}_4:\text{O}_2$  at 250mW for 60 minutes**

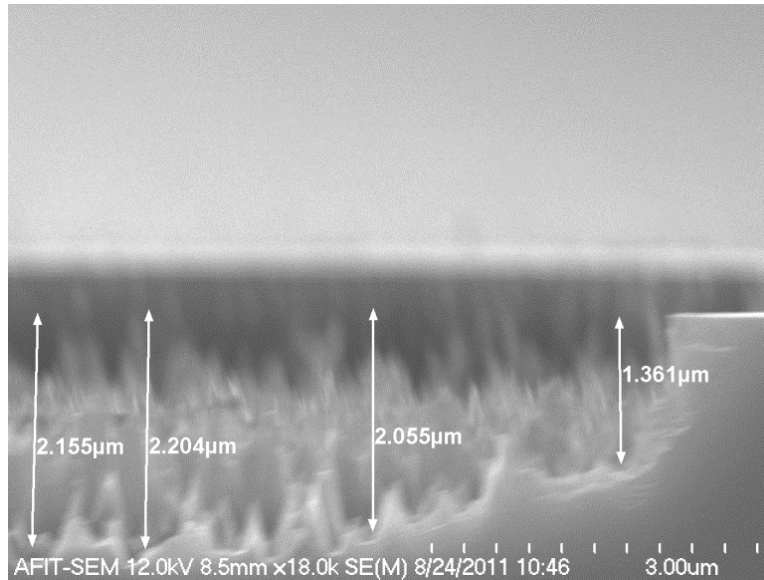


**Figure 42 - SEM image of SiC test piece etched at a flow rate of 30:1  $\text{CF}_4:\text{O}_2$  at 250mW for 90 minutes**

One issue found with the Jupiter RIE was it does not hold a plasma at lower powers and requires constant adjustment to ensure proper operation. This issue was resolved by the installation of a Trion RIE in the AFIT cleanroom. The Trion RIE allows for controlled etching with little user interaction. It also maintains a plasma at lower operating parameters. As such, it became the RIE of choice in this work. Because of the change in RIE system, an additional etch depth test was conducted using the Trion RIE.

Four different samples were used to characterize the etch rate of the Trion ICP RIE. Each sample was prepared as outline in the pre-RIE process documented above using the borrowed ALICE mask. Because the flow parameters of the Trion system vary from the Jupiter system, the standard cubic centimeter per minute (sccm) was changed from the scale reading of the Jupiter flowmeters. For example, a  $\text{CF}_4$  scale flow of 30 corresponds to 13 sccm. The samples were etched with the parameters listed in Table 4.

**Table 3 – Etch Rate Study Parameters using TRION RIE**

Sample	Time (sec)	Power (mW)	CF <sub>4</sub> Flow (sccm)	O <sub>2</sub> Flow (sccm)	Pressure (mTorr)
1	20	250	13	5	85
2	25	250	13	5	85
3	20	250	40	4	25
4	20	250	60	12	25

A profilometer was used to characterize the etch depth of the RIE samples. Each sample was measured with the probe moving to both the left and the right. Table 4 summarizes the result of the step height analysis after the nickel mask was etched. The results below show that the flow rate had little effect on the etch depth. As such an arbitrary flow values of 25 sccm for CF<sub>4</sub> and 5 sccm for O<sub>2</sub> was used to obtain a flow ratio 20%.

**Table 4 – Summary of Etch Rate Step-height analysis**

Sample	Direction	Measurements (mm)			Average (mm)
1	Left	1.58	1.78		1.68
	Right	1.683	1.767		1.73
2	Left	2.1	2.2		2.15
	Right	2.3	2.25		2.28
3	Left	1.93	1.686		1.81
	Right	1.77	1.79	1.78	1.78
4	Left	1.68	1.67	1.73	1.69
	Right	1.62	1.62	1.8	1.68

The SEM images in Figure 43 and Figure 44 are from sample 2 etched with 13 sccm CF<sub>4</sub> and 5 sccm O<sub>2</sub>. They show the etched structure before and after the nickel mask was removed. As was discussed previously, micromasking of the etched surface can be seen in Figure 44 as the bulbous heads. Along with etching the nickel mask, the nickel etchant also removes these heads leaving an etched spiked surface.

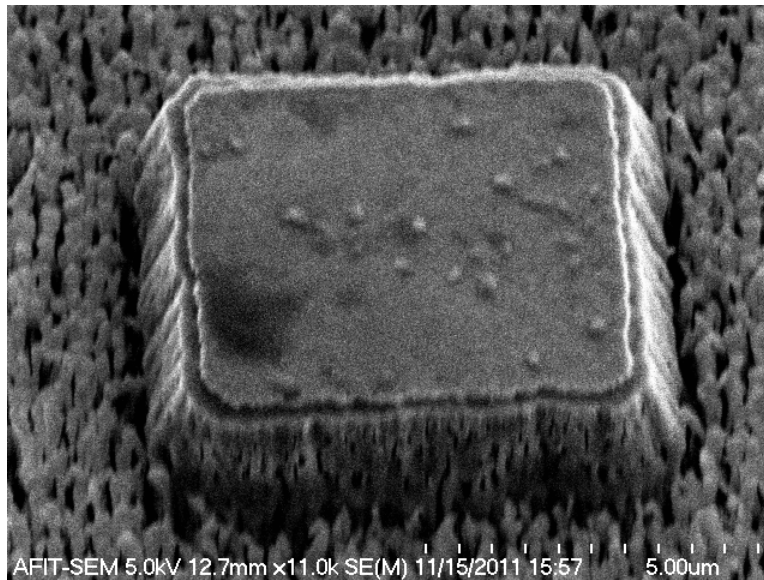


**Figure 43 – SEM image of test sample 2 after a 25 min RIE at a flow rate of 13:5 sccm  $\text{CF}_4:\text{O}_2$  at 250mW prior to nickel mask removal**

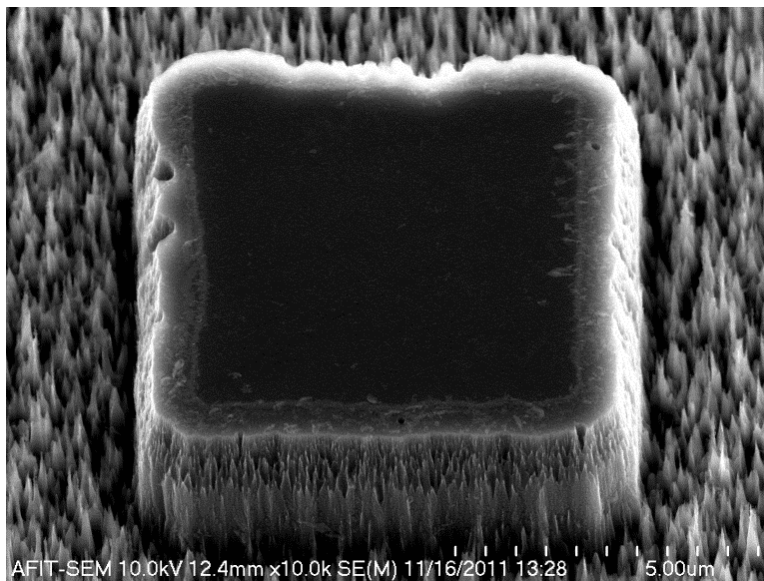


**Figure 44 – SEM image of test sample 2 after a 25 min RIE at a flow rate of 13:5 sccm  $\text{CF}_4:\text{O}_2$  at 250mW after nickel mask removal**

### 3.2. CNT Growth Procedures

The SiC decomposition method used to grow CNTs was based on a hierarchy of previous work starting with Kusunoki *et al*, followed by Mitchel and then Pochet [17, 19, 52]. The basic thermal decomposition method, described in detail in section 2.3. , involves the heating of a SiC substrate to 1700 °C for a predetermined time.

The SiC samples used for decomposition have either been patterned by an RIE process outlined above or remain unetch. Prior to decomposition, the samples were cleaned using a solvent to remove any remnant organics and a buffered-oxide-etch to remove native oxides that may have formed on the surface. Once the samples were cleaned, they were placed inside a graphite resistance furnace manufactured by Oxy-Gon Industries, Inc, Epsom NH. The furnace was pumped down to a high vacuum between  $10^{-5}$  and  $10^{-6}$  Torr. The samples were then heated to 1250 °C and held for 30 minutes to allow carbon nanocaps to form by the process described in section 2.3.1. The heating cycle for nanocap formation was shown in Figure 45.

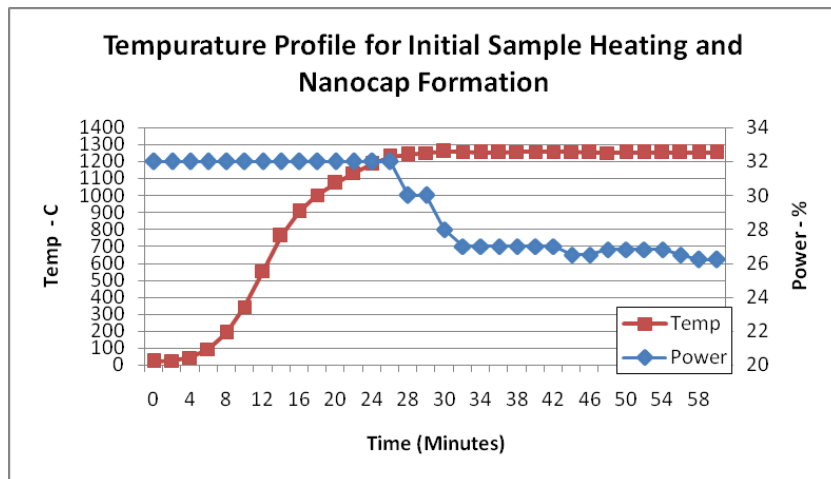


**Figure 45 – SiC temperature and heating profiled for initial sample heating and carbon nanocap formation**

After 30 minutes the samples were heated to 1700 °C. The profile for this heating cycle is shown in Figure 46. A linear regression of the heating cycle in Figure 47 shows that the furnace increases the temperature of the sample as roughly 54.5 °C per minute at a power of 37%. The heating rate can be changed by either raising or lowering the power during this cycle.

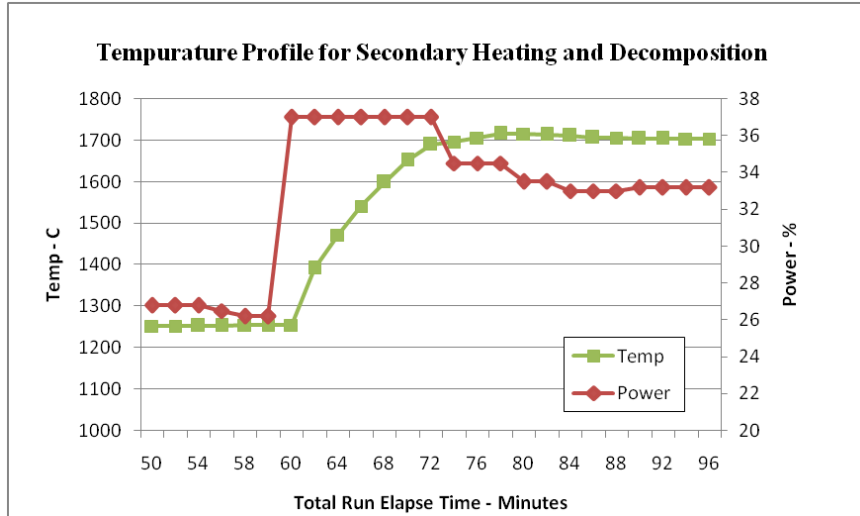


**Figure 46 – SiC temperature and heating profile between 1250 C and 1700 C**

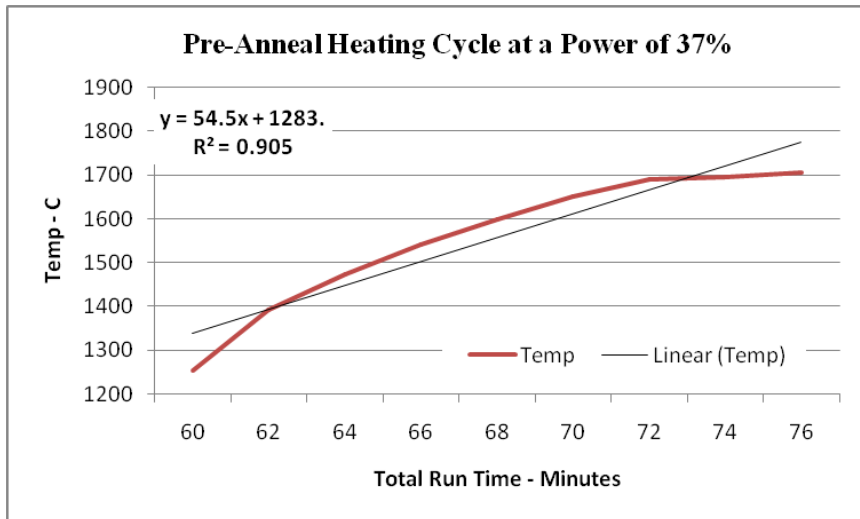


**Figure 47 – Pre-anneal heating cycle between 1250 C and 1700 at a constant 37% power, showing a heat rate of approximately 54.5 degrees/minute**

The result of this growth process is shown in Figure 48 which shows a cross-sectional SEM image C-face SiC sample annealed for 60 minutes at 1700 °C. The inset figure shows a growth of approximately 250 nm.

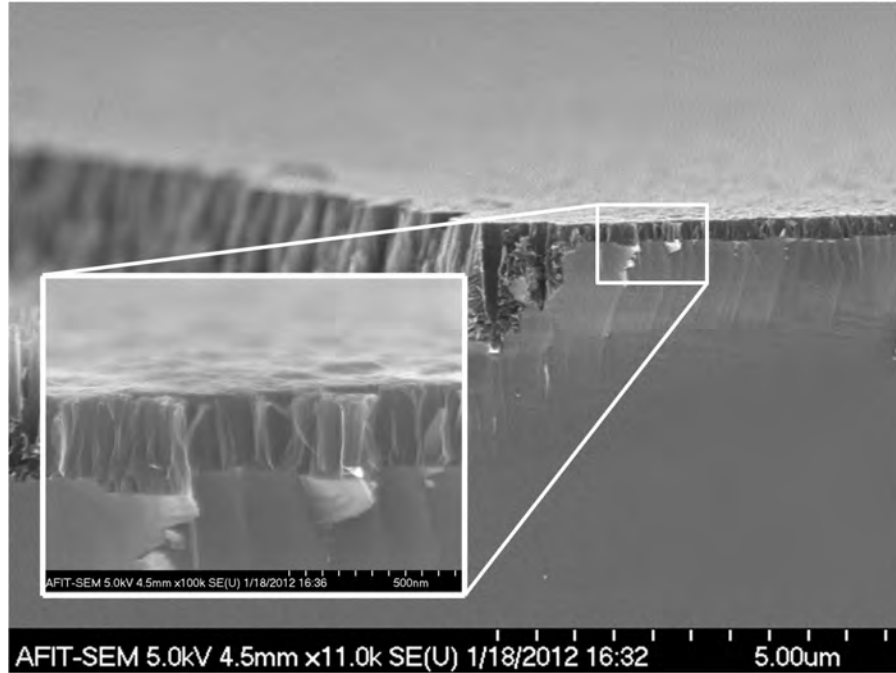


**Figure 48 – C-face SiC sample annealed for 60 minutes at 1700 C, inset shows an approximate growth of 250 nm**

The CNTs grown on Si-face SiC for 3 hrs are shown in the 45 degree tilt SEM image in Figure 49 while Figure 50 shows the top of the CNT surface at a 45 degree tilt. The CNTs in the inset are approximately 200-225 nm in length, which was consistent with the 3:1 ratio between the growth rate on the C-face and Si-face described by Mitchell *et al* [19].

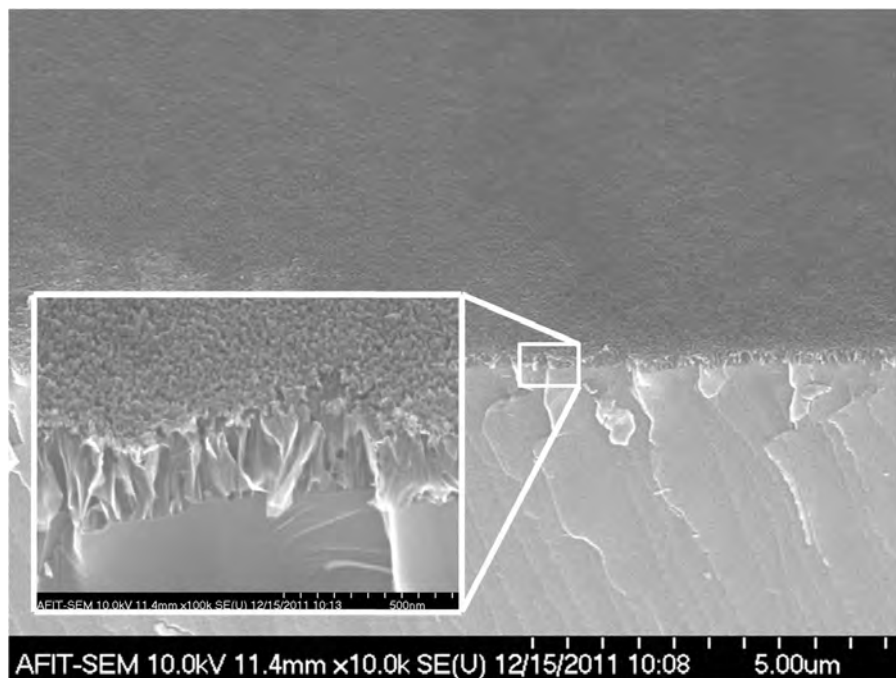


**Figure 49 – Si-face SiC sample annealed for 3 hours at 1700 C, inset shows an approximate growth of 200-225 nm**

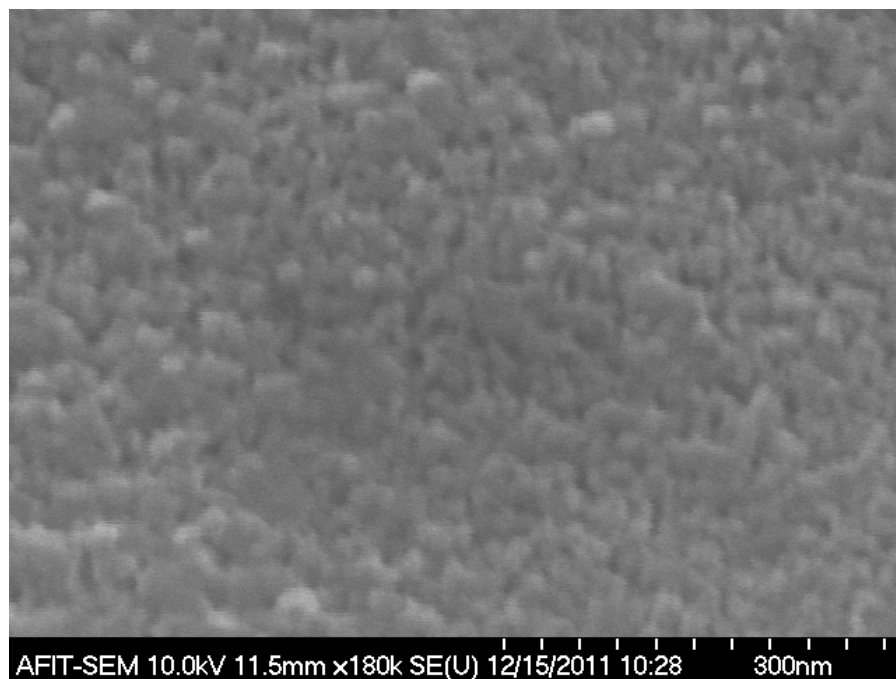


**Figure 50 – 45 degree surface view of Si-face SiC sample annealed for 3 hours at 1700 C, showing CNT caps and amorphous carbon**

### 3.3. Field Emission Testing

#### 3.3.1. Data Collection

Field emission test were conducted a vacuum chamber setups at AFIT. The test configuration consisted of two parallel plates separated by acrylic spacers. The setup was borrowed from the ALICE project and since it has an air gap was referred to as the AA setup. The CNT sample on the AA setup was held in place on the cathode plate by using the copper ground wire.

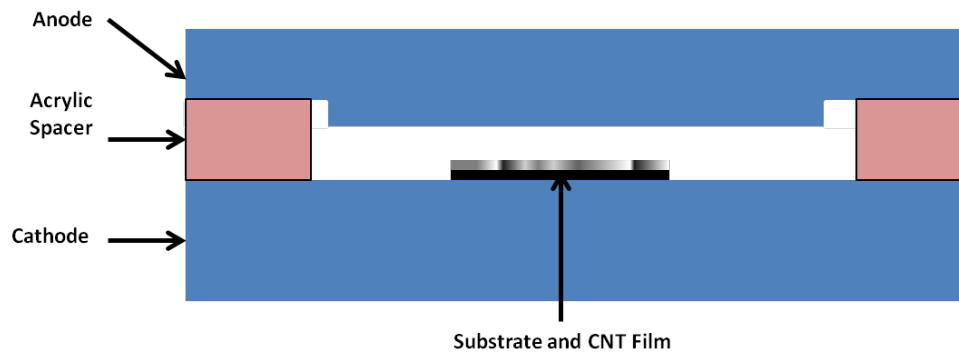


**Figure 51 – Alice with airgap (AA) test setup with a 215  $\mu\text{m}$  anode-sample gap**

Due to the irregular shape of the emission surface the platform was modified to resemble the method developed by Pochet [52]. This method uses a 100  $\mu\text{m}$  thick Teflon<sup>®</sup> spacer with a 1/16” hole. Because it uses the ALICE setup with a Teflon space this setup was referred to as the AT setup. The hole in the Teflon<sup>®</sup> provides a controlled emission area of .0186  $\text{cm}^2$ . The test configuration for this configuration is illustrated in Figure 52.

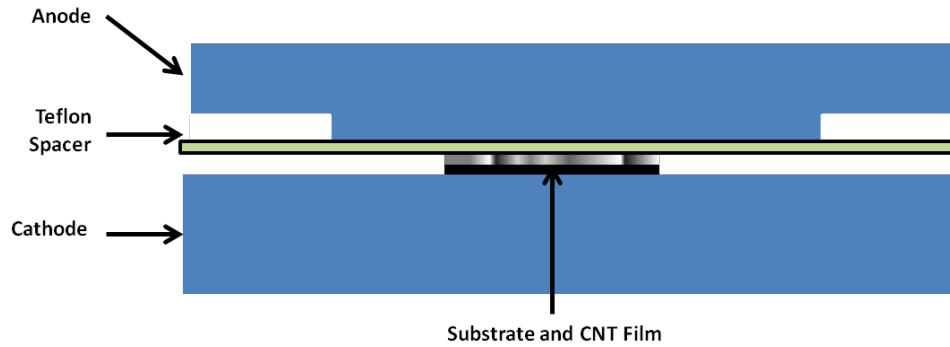


**Figure 52 – ALICE with Teflon<sup>®</sup> space (AT) with an emission area of .0186 cm<sup>2</sup> and 100 μm anode-sample gap**

The third sample testing setup, shown in Figure 53, was the exact apparatus used previously by Pochet, as such it was referred to as the MP setup. The configuration of the MP setup was identical to that shown in Figure 53, but the copper plates and holding mechanisms differ. The surface of the copper anode in this configuration was highly polished in comparison to the two ALICE setups. The MP setup was also modified to work with the connections used in the vacuum chamber.

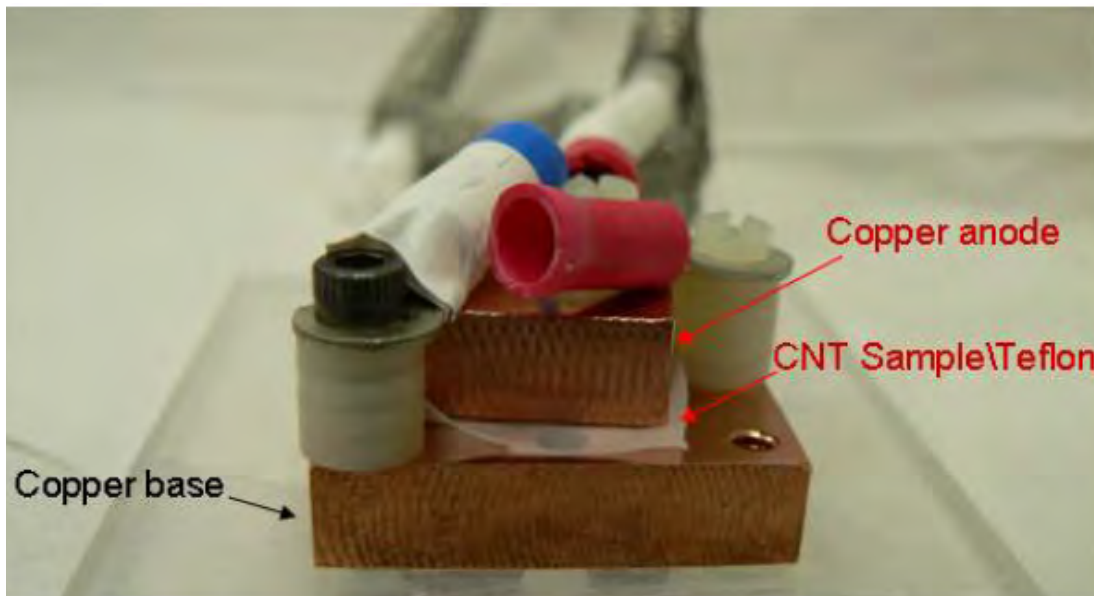


**Figure 53 – Pochet setup with Teflon<sup>®</sup> space (MP) with an emission area of .0186 cm<sup>2</sup> and 100 μm anode-sample gap (Pochet 2006)**

Once the samples are configured for field emission, they are loaded into the vacuum system. The vacuum system, diagrammed in Figure 54, consist of load lock and vacuum chamber capable of vacuum pressures of  $10^{-9}$  Torr. The vacuum was obtained through the use of turbo pump backed by a roughing pump. The procedure used to load and unload samples from the chamber was provided in Appendix D: Field Emission Chamber Procedures (Courtesy of Major Nathan Glauvitz, AFIT).

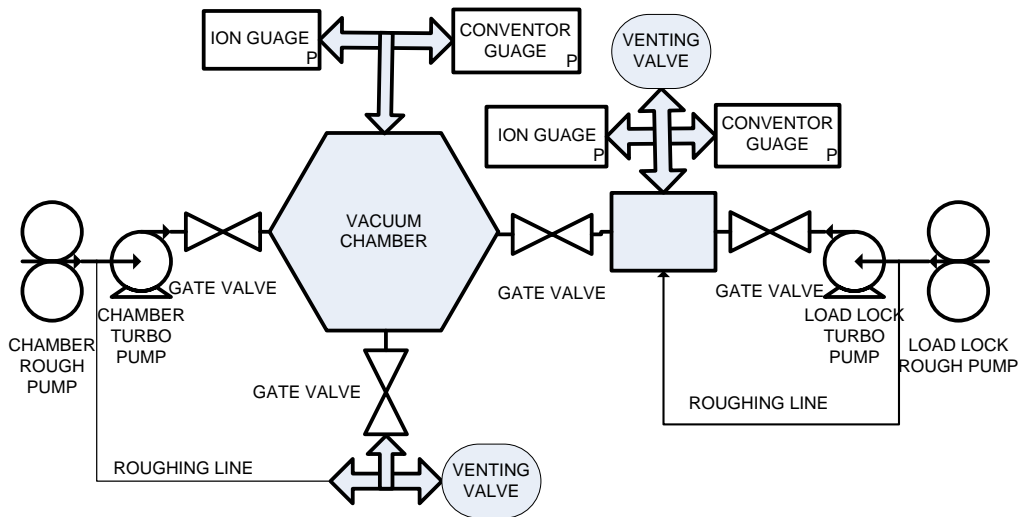


**Figure 54 – AFIT field emission vacuum chamber setup**

Electrical connections inside the chamber were obtained through the use of a MDC transferable test station which allowed easy connection and removal of sample from the chamber. Field emission measurements were obtained through National Instruments LabView Virtual Instrument (VI) software. The LabView VI was connected to a Stanford Instruments high voltage supply, and Agilent digital multimeters through a USB enabled GPIB controller. Voltage data were obtained from the power supplies, while current data were obtained the voltage measurements across a known 1 k $\Omega$  resistors in both the supply and return paths as illustrated in Figure 55 The data are collected by sweeping the high voltage source from 100 V to 2000 V in 25 V steps until

the supply detected a current overload and trips. The maximum voltage obtained was used as the maximum for the device under test. A quick analysis of the I-V plot was used to narrow the voltage sweep and reduce the quantity of data collect. Subsequent data collections were swept in step increments of 10 VDC. Final collection runs of samples were paused at a predetermined voltage to collect constant current data. Data were outputted to a data file that can be post-processed in Microsoft® Excel, MATLAB®, or other data processing suites.

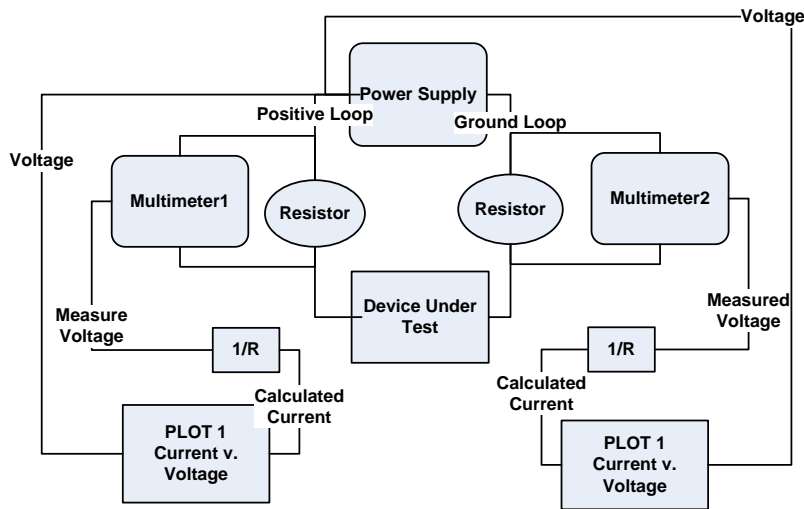


**Figure 55 – Field emission measurement setup, current was derived from voltages measured across 1kΩ resistors**

### 3.3.2. Data Processing

Collected data were processed to determine the structured CNTs parameters. These parameters include the turn-on field  $E_{to}$ , the threshold field  $E_{th}$ , maximum current density  $J_{max}$ , and field enhancement factor  $\beta$ . To allow comparisons to different published works,  $E_{to}$  will be calculated  $1 \mu\text{A}/\text{cm}^2$ . The values for  $E_{th}$  were determined for a current density of  $1 \text{ mA}/\text{cm}^2$ .

The field emission from the samples was also analyzed using F-N plots. The F-N plots have a coordinate system utilizing  $\ln(I/V^2)$  on the dependent (y) axis and  $I/V$  on the independent (x) axis. Specifically in the case of F-N plots  $V$  can be either the applied voltage in  $V_{DC}$  or the applied electric field  $V/\mu m$ , while  $I$  was the emission current density given in  $A/cm^2$ . As discussed previously, if the F-N plot is linear the device are emitting by field emission. The F-N plot was also used to determine  $\beta$ . By utilizing equations (2.16), (2.20), and (2.21), restated below as (2.32), (2.33), and (2.34),  $\beta$  can be determined using a linear plot fit to find the slope of the F-N plot.

$$\ln(I/V^2) = (-b\phi^{3/2}d/V) + \ln(Aa\phi^{-1}d^{-2}) \quad (2.32)$$

$$M = \frac{-b\phi^{3/2}d}{\beta} \quad (2.33)$$

$$B = \ln\left(\frac{Aa\beta^2}{\phi d^2}\right) \quad (2.34)$$

Equation (2.33) can be solved for  $\beta$  as shown in equation (2.35) where  $b$  is universal constants defined as  $6.83 \times 10^{-7} V eV^{3/2} cm^{-1}$ ,  $M$  is the slope of the fitted linear plot,  $\phi$  is the work function of the carbon nanotubes (4.5 – 5.0 eV), and  $d$  is the distance from the emitter tip to the anode.

$$\beta = \frac{-b\phi^{3/2}d}{M} \quad (2.35)$$

### **3.4. Chapter Summary**

The purpose of this chapter was outline the process required to create sample suitable for field emission. It outlined the lithography process needed to pattern the SiC samples. It discussed the methods used to determine the RIE process. Finally, it discussed the process by which field emission data were collected and analyzed.

## **Chapter IV: Results and Analysis**

### **4.1. Introduction**

During sample preparation, samples were grouped into sets to compensate for varying conditions that may occur during different days. The intent of making these sets was to have multiple samples that were developed under identical conditions. These sets were also maintained during in the SiC decomposition and CNT process. The final samples used for field emission testing were labeled as sample set H, J, K, and L. In the analysis of the samples the sets continuity is maintained for a sample-to-sample comparison after which a set-to-set comparison can be made. With the exception of sample set H, all the sets were processed using the Si-face of the SiC carbide wafer. This was due to the polish roughness of the C-face on those samples. Samples in sets J, K, and L were all patterned. The samples in set H contained two samples with etched patterns, a sample etch without patterning, and an unetched sample. This set specifically allowed the opportunity to examine the variability of sample extremes and as such its analysis is presented last among the samples. After the samples were processed, they were subjected to field emission testing. The analysis of this testing, highlighted in section, 4.4.5. reveal how each sample reacts to an applied electric field, and whether or not the electron emission current from the samples is from field emission.

### **4.2. Sample Set Surface and Process Analysis.**

#### **4.2.1. Sample Set J**

This sample set contained two samples, with each sample processed according to the procedure outlined in Chapter 3. The nickel mask on both samples was etched using 50 °C TFG for 3.5 minutes, and the PR was not removed prior to RIE. The samples were

etched in a  $\text{CF}_4$  and  $\text{O}_2$  plasma for 20 minutes. The results of the RIE prior to nickel removal can be seen in Figure 56 and Figure 57, which show the moderately symmetric pillars for both sample J1 and J2. Figure 58 shows spacing of both sample J1 and J2. The SEM images show a contrast between the amount of nickel mask remaining and quality of the pillar surface. After the nickel mask was removed the pillar structures resemble those shown in Figure 59.

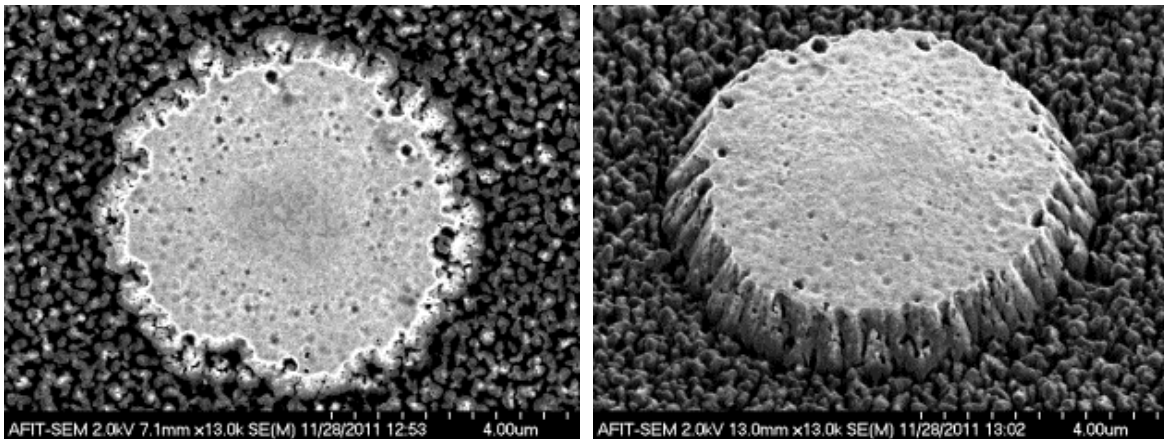


**Figure 56 – SEM image of sample J1 after 20 min RIE and prior to nickel mask removal, (left) planar view of surface at 13k magnification, (right) 45 degree view taken at 13k magnification**

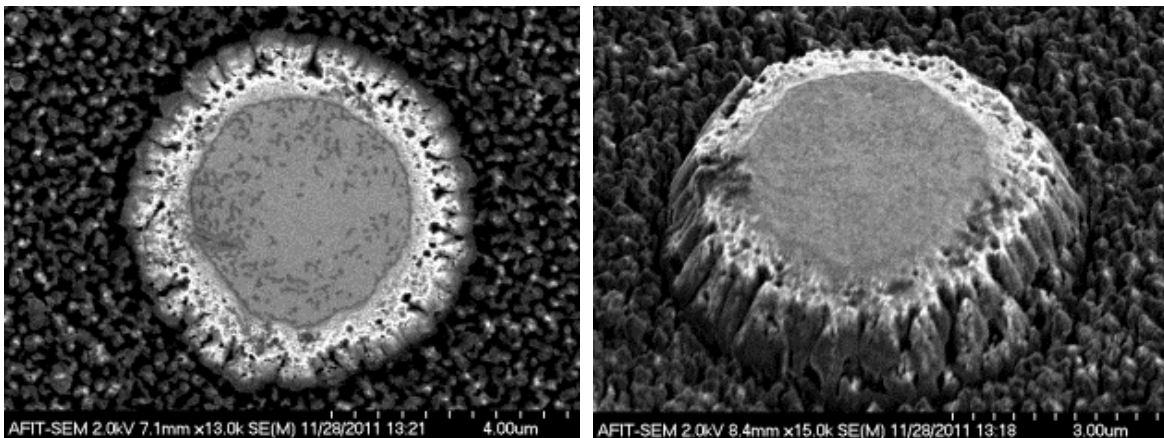


**Figure 57 – SEM image of sample J2 after 20 min RIE and prior to nickel mask removal, (left) planar view of surface at 13k magnification, (right) 45 degree view taken at 15k magnification**

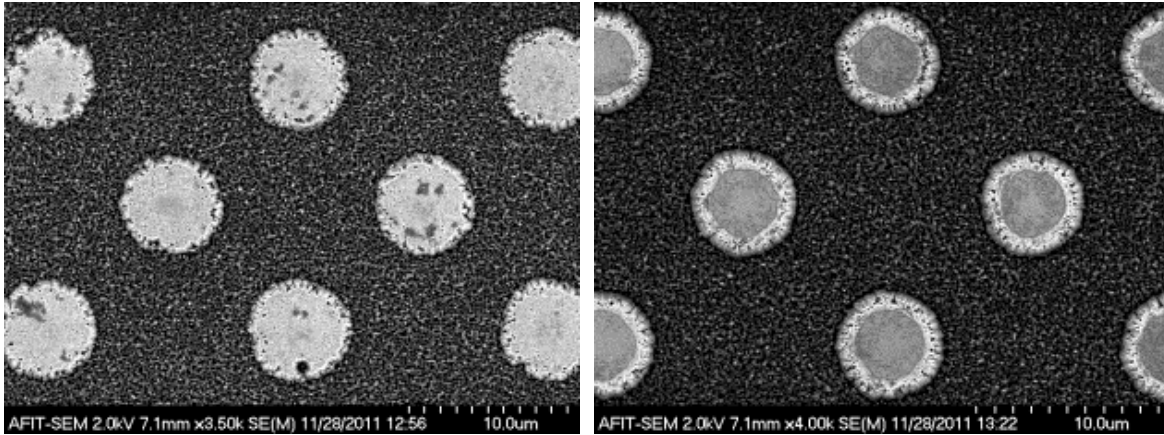


**Figure 58 – SEM image of sample set J after 20 min RIE and prior to nickel mask removal showing the inter-pillar spacing, (left) J1, (right) J2**

After the nickel mask was removed the pillar structures resemble those shown in Figure 59.

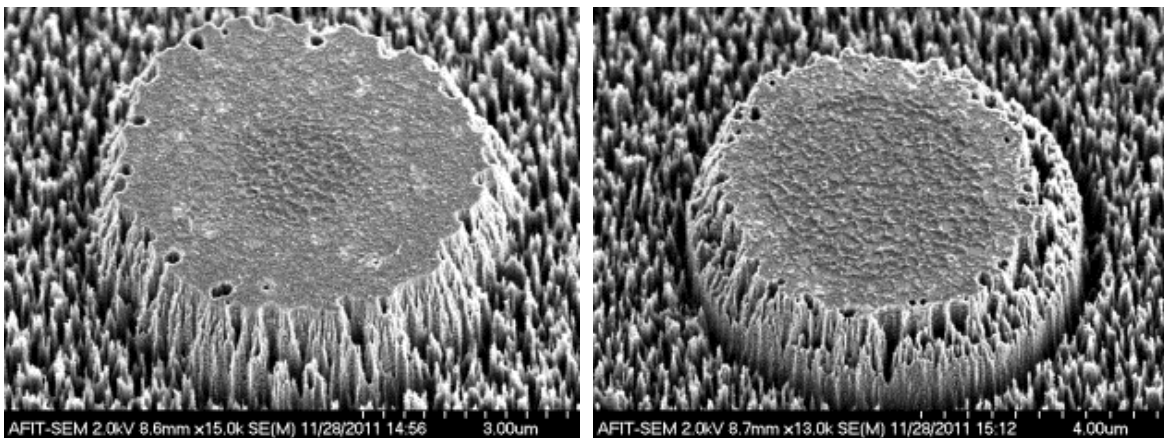


**Figure 59 – SEM image of sample set J after 20 min RIE and after nickel mask removal, (left) J1, (Right) J1**

#### 4.2.2. Sample Set K

Sample Set K included three samples. Each sample was processed according to the procedures outlined in Chapter 3, with the nickel mask etch time varied. The variability in the etch times was an attempt to refine the masking process. The samples identified as K1-K3 were etched in TFG for times of 2.5 minutes, 3 minutes, and 3.25 minutes. Optical inspection of the sample revealed good undercut from the 2.5 minute

and 3 minute etch times, and poor undercut for the 3.25 minute etch. No optical images of this set are available due to image capture equipment being inoperable during the time of this processing step. Increased etching times were investigated due to the belief that residual nickel remained on the areas to be etched, resulting in the rough surface topology on the etched areas as observed in Figure 37. The increased etch time was an attempt to more thoroughly remove all the nickel from the exposed surface; however, the increased etch time resulted in too severe of an undercut to the nickel pattern to provide workable samples for future SiC etching. Another issue that arose with this sample set was a wave pattern was present on the sample after exposure. This pattern was believed to be the result of poor sample-mask contact caused by having a small sample size and using the vacuum contact mode of the mask aligner. The resulting exposure of the photoresist, resembles closely the refraction pattern of light on the mask itself. This wave pattern can be seen in the SEM images in Figure 60 for sample K1.

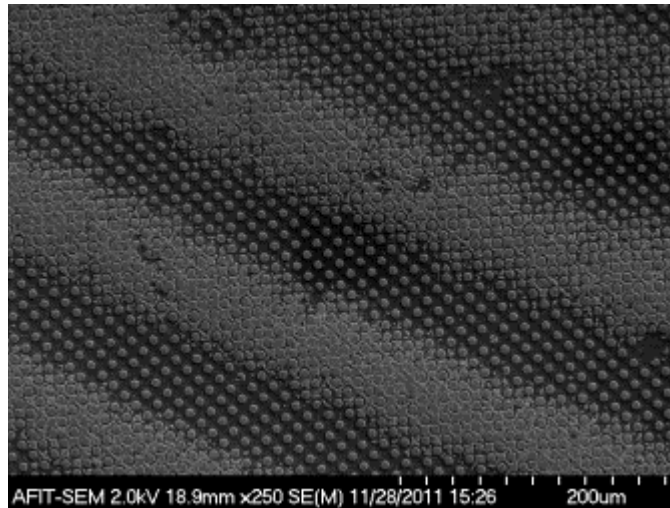


**Figure 60 – SEM image of the wave pattern created by UV light refraction on the during the photolithography process**

The SEM images in Figure 61, Figure 62, and Figure 63 show planar and 45° view of pillars from sample K1-K3 after the nickel mask was removed. The difference between the samples is the result of undercutting during the nickel mask etch. The pillar walls from sample K1 in Figure 61 show a cleaner structure and the pillars were more symmetric, while at the other extreme sample K3 in Figure 63 shows a ring where the nickel was etched but not completely removed. The pillars on sample K3 were also vary asymmetric. Figure 64 shows the spacing of all three samples.

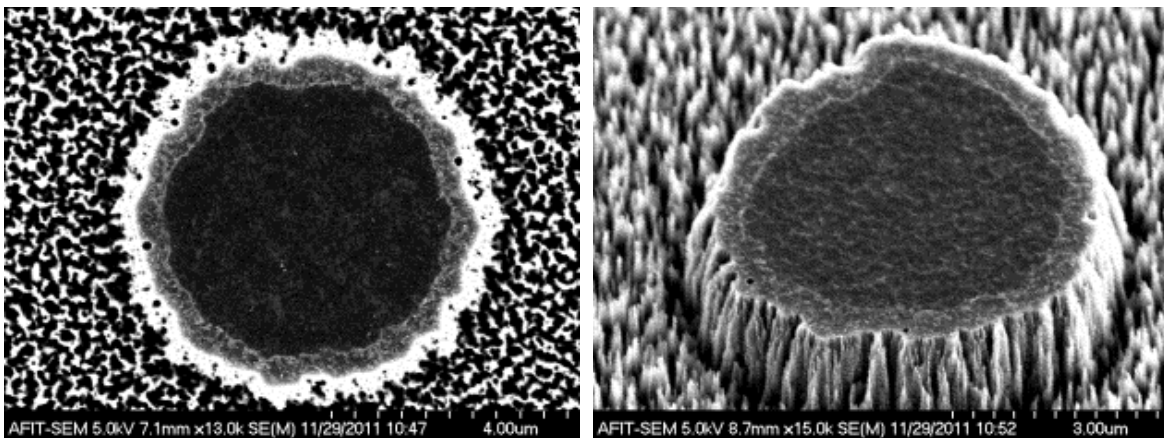


**Figure 61 – SEM image of sample K1 after 20 min RIE and after nickel mask removal, (left) planar view of surface at 13k magnification, (right) 45 degree view taken at 15k magnification**

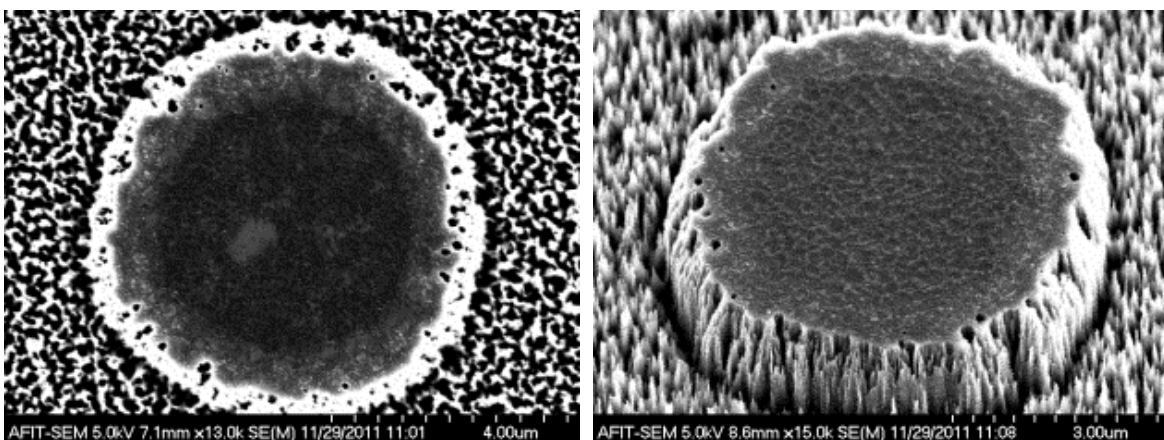


**Figure 62 – SEM image of sample K2 after 20 min RIE and after nickel mask removal, (left) planar view of surface at 13k magnification, (right) 45 degree view taken at 15k magnification**

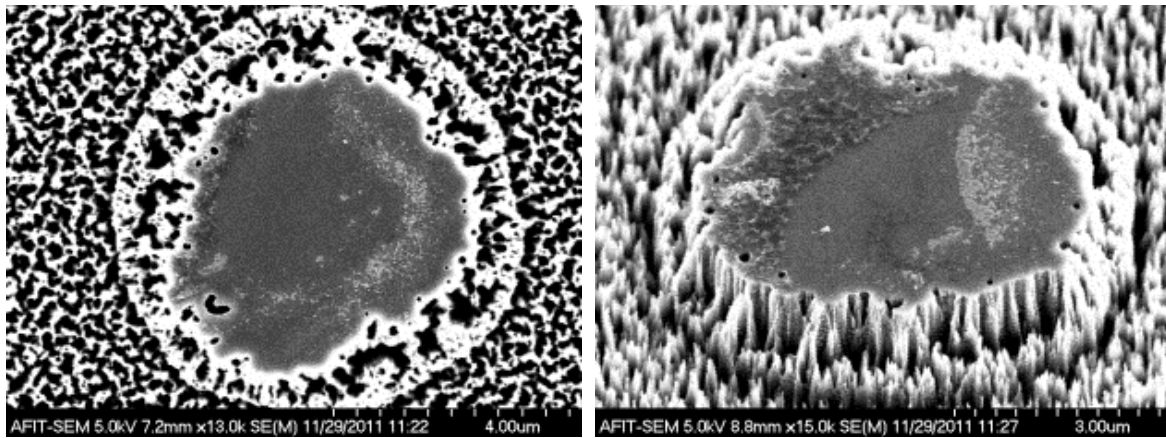


**Figure 63 – SEM image of sample K3 after 20 min RIE and after nickel mask removal, (left) planar view of surface at 13k magnification, (right) 45 degree view taken at 15k magnification**

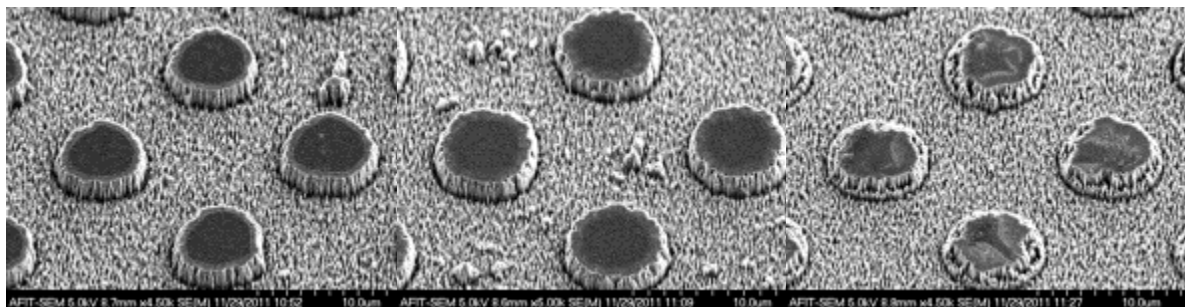


**Figure 64 – SEM image of sample set K after 20 min RIE and after nickel mask removal showing the inter-pillar spacing, (left to right) K1, K2, and K3**

#### 4.2.3. Sample Set L

The two samples from sample set L were processed through the same steps as sample sets J and K. The nickel mask was etched for 3 minutes in 50 °C TFG. The variations between the two samples come from the presence of the 1805 PR during the RIE. Sample L1 had the 1805 removed prior to RIE while the 1805 PR was not removed from the sample L2 prior to RIE. This method was attempted to see the effects of the existence of PR during RIE on pillar structure. A side-by-side comparison of both samples is shown in the SEM images in Figure 65. The results can be interpreted in one of two ways. The first is that the presences of the PR slowed the etching on the edges of

the structure. The second is that the original nickel insufficiently masked the surface. Since sample L1 closely resembles that of sample K3 in Figure 63 above, the later explanation is most likely. SEM images of the L1 and L2 after the nickel mask was removed are shown in Figure 66

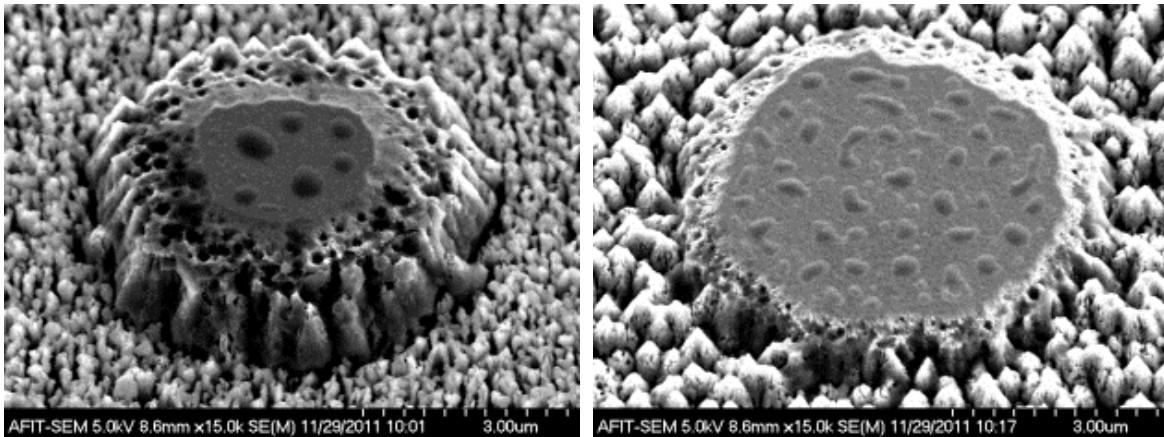


**Figure 65 – Comparison of sample set L after 20 min RIE and prior to nickel mask removal taken at 45 ° and 15K magnifications, (left) L1 had the PR removed prior to RIE(right) L2 had PR remaining prior to RIE**

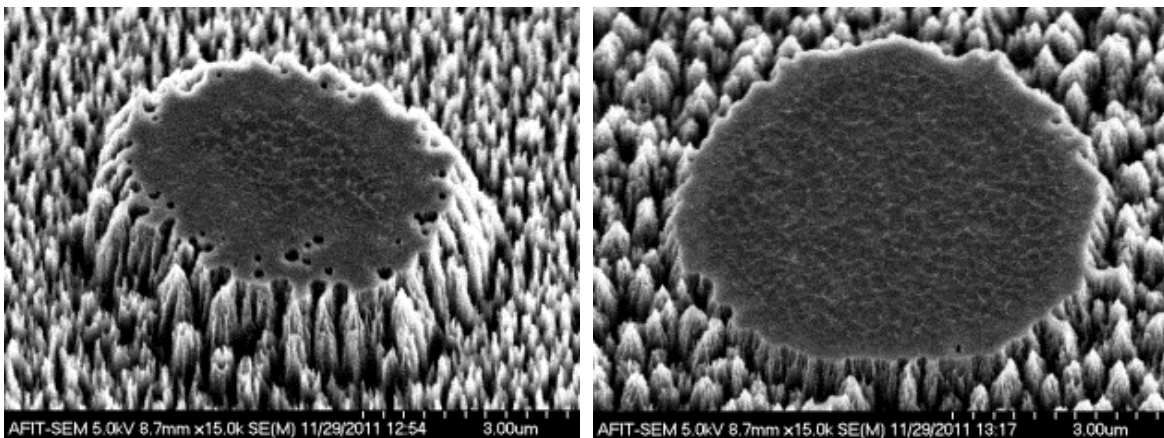


**Figure 66 – Comparison of sample set L after 20 min RIE and after nickel mask removal taken at 45° and 15K magnifications, (left) L1 had the PR removed prior to RIE(right) L2 had PR remaining prior to RIE**

#### 4.2.4. Sample Set H

Sample set H contained four samples each processed differently. Unlike previous samples, sample set H utilized the C-face of the SiC wafer. Samples H2 and H3 were

each processed for RIE using methods outlined in chapter 3. Samples H2 and H3 was masked with 6  $\mu\text{m}$  features. In an attempt to achieve a more symmetrical and controllable undercut the samples were agitated in TFG horizontally using a basket (rather than vertically using forceps as previously done). The process, however, required a large volume of TFG and subsequently more heat to obtain and maintain the etch temperature of 50  $^{\circ}\text{C}$ . The results of the nickel etch for sample H2 are shown in Figure 67, which shows the primary round nickel structure and remaining ‘spider-web’ effect on the rest of the SiC substrate.

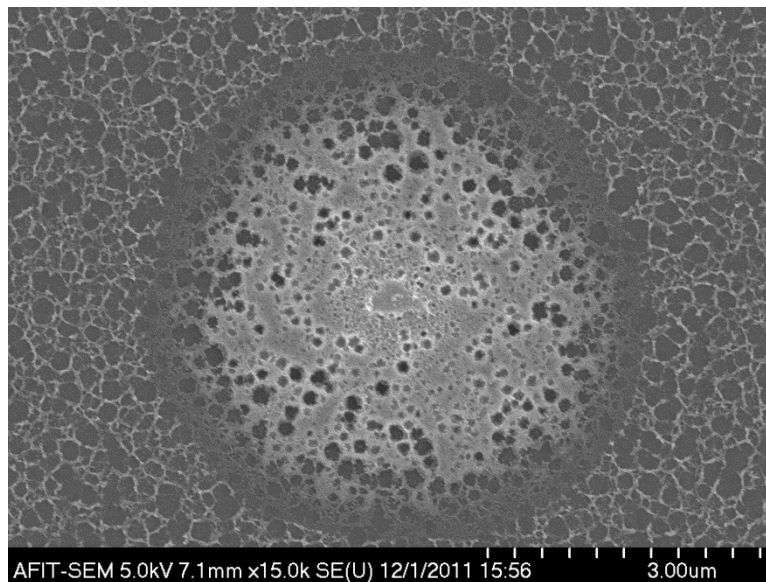


**Figure 67 – SEM image of etched nickel on a H sample, showing the lack of thorough Ni etching and spider web Ni pattern on unmasked region**

This again shows an issue with trying to etch the nickel mask completely. Any attempt to completely remove the nickel from the substrate results in poor structures, but trying to maintain a well defined nickel mask leads to an increase in the micro-masking structures found after RIE, shown in Figure 68. These micro-masking effects can be seen in more detail in the SEM images found in Figure 69 which shows a comparison between

pre and post-nickel mask removal. Sample H3 was etched also etched for 3.5 minutes in TFG, but after RIE showed a more defined structure which can be also be seen in Figure 68.

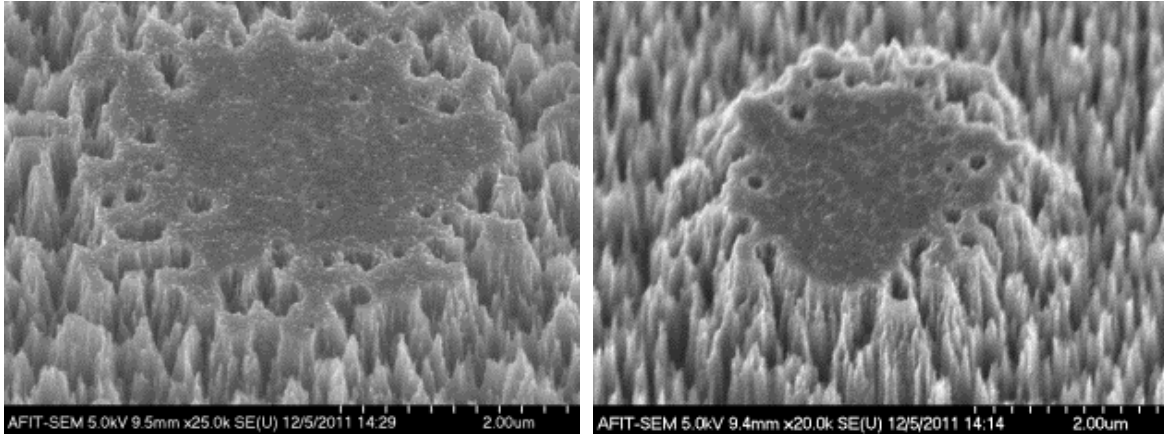


**Figure 68 – SEM images taken at 45 ° of sample set H after 20 min RIE and after to nickel mask removal, showing the results of a defined nickel mask (left) H2 at 20k magnification, (right) H3 at 20k magnification**

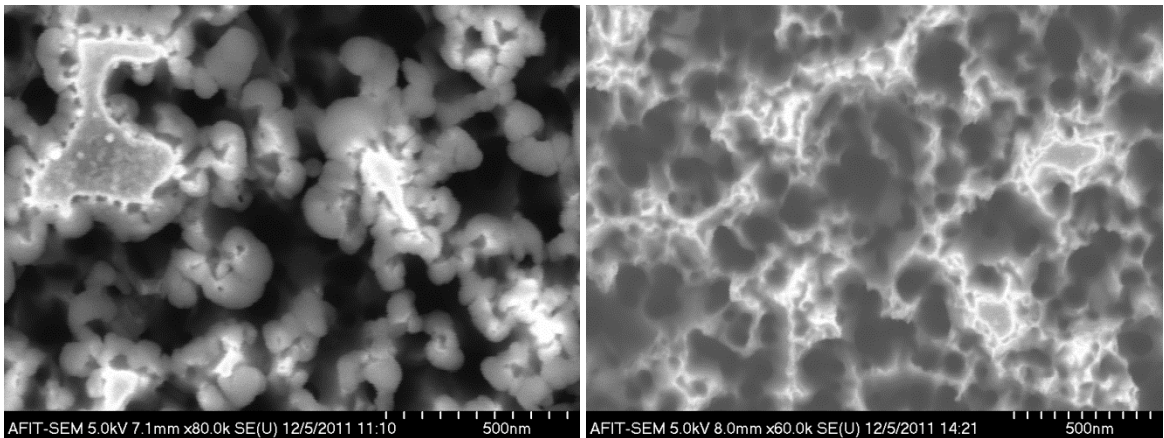


**Figure 69 – SEM image of the etch portion of the SiC, (left) prior to Ni removal, (right) after Ni removal**

### **4.3. SiC Decomposition of Samples**

This section shows the results of the CNT growth on the sample sets. Included in these results are the parameters for growth for each set as well as a discussion on where CNTs grew on each samples. Again, the samples will be discussed in the order of sets J, K, L and concluding with sample H.

#### **4.3.1. Sample Set J**

Sample set J was annealed in the AFRL/RX furnace for 3 hours. The time selected for decomposition was because of the use of the Si-face of the SiC wafer. Growth on the Si-face has been shown to grow at a rate one-third of the C-face. The sample temperature in the chamber was first increased to 200 °C to provide a softbake for 15 minutes. After the softbake, the temperature was raised to 1250 °C for 30 minutes to form nanocaps. The chamber temperature was increased to 1700 °C to perform the CNT growth. After growth, the chamber was allowed to cool and samples removed. Sample J2 was then cleaved and placed inside the AFIT SEM for inspection. The results of the CNT growth are shown in incremental magnification in Figure 70 and Figure 71. The CNT carpet on the structures grew to a height of approximately 280-300 nm.

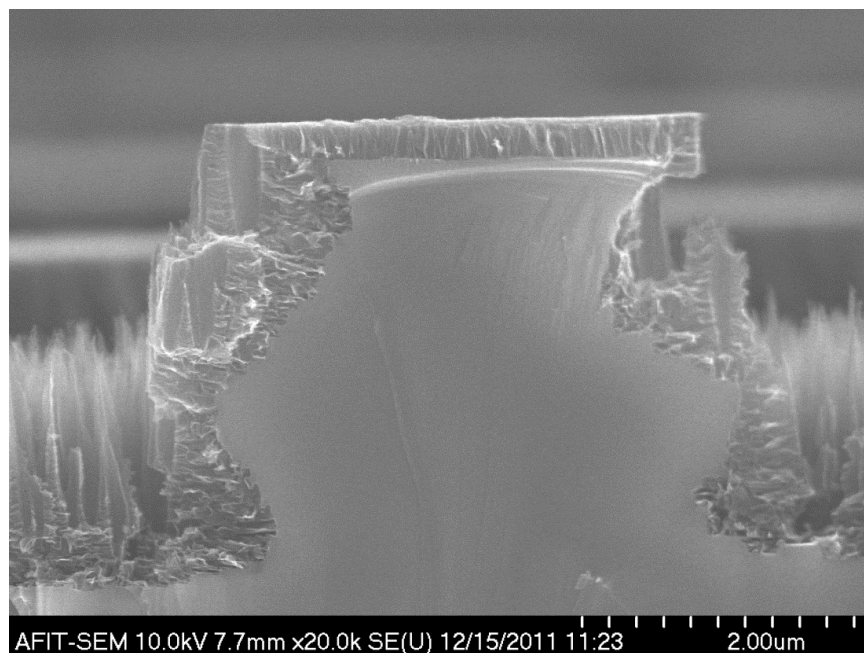


**Figure 70 – SEM image taken at 20k magnification of sample J2 showing the growth of CNTs on the pillars after 15 minute softbake, 30 minute nanocap formation and 3 hour CNT growth**

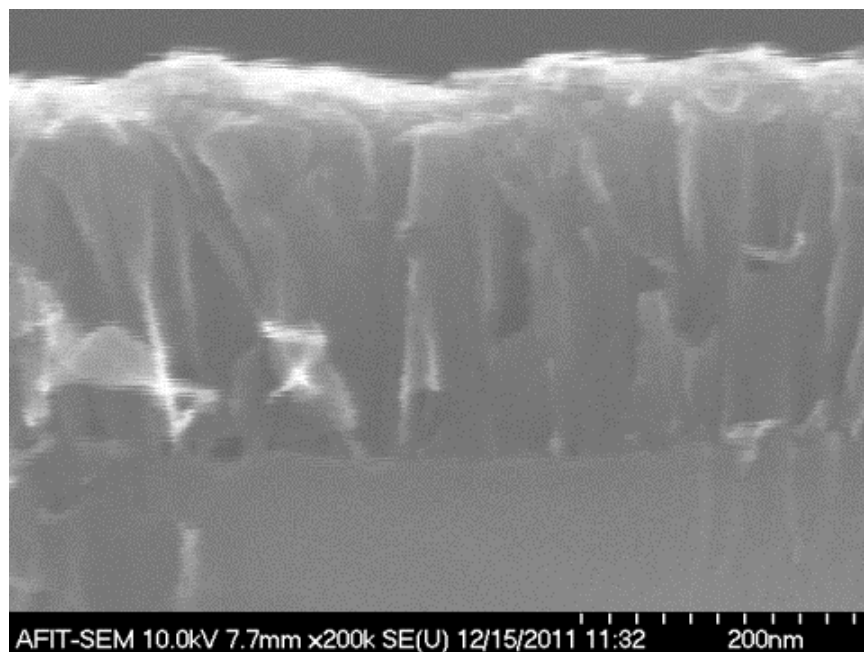


**Figure 71 – SEM image taken at 200k magnification of CNT film found on top of structure found on sample J2 in figure ( )**

CNT growth, however, was also found throughout the sample. The SEM image in Figure 72 shows CNTs growing on the sides of the structures and terminating at the base of the vertically grown CNTs. This termination can clearly be seen as an angled line at the base of the CNTs in Figure 72.

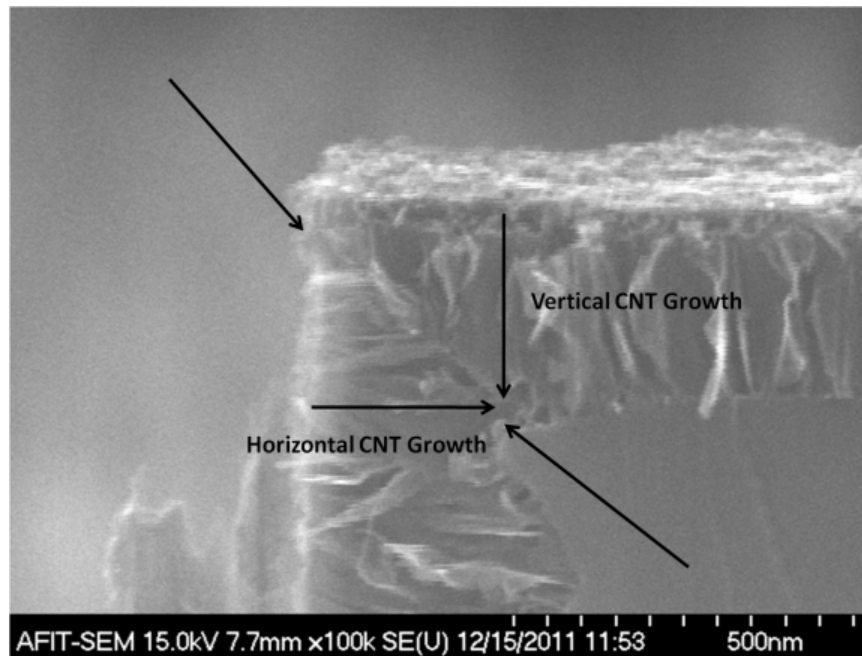


**Figure 72 – SEM image taken at 100k magnification of vertically and horizontally grown CNTs found on pillar of sample J2, 15 minute softbake, 30 minute nanocap formation and 3 hour CNT growth**

Probable CNT growth was also found on the etched SiC spikes in between structures. The discovery of CNTs in this location is significant since most CNT growth from the thermal decomposition of SiC is thought to only be possible on smoother surfaces. [17]. Figure 73 shows an SEM image of this growth where the CNTs appear to terminate at the center of the spiked structure.

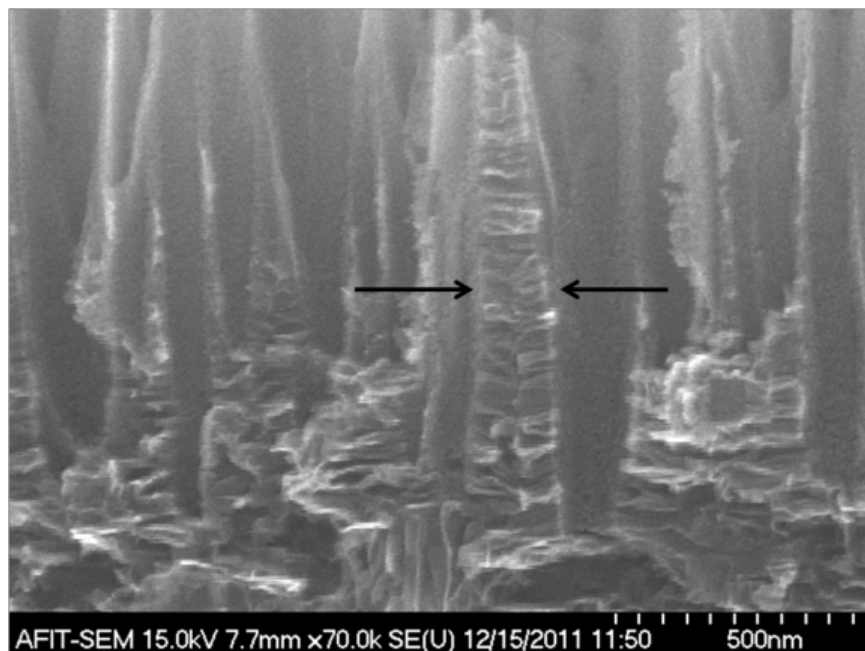


**Figure 73 – SEM image taken at 70k magnification of etched surface of sample J2 showing probable CNT growth, 15 minute softbake, 30 minute nanocap formation and 3 hour CNT growth**

#### **4.3.2. Sample Set K**

Sample set K was also annealed for 3 hours. However, discussion about the process with Dr. John Boeckl found that for thermal decomposition the use of the softbake step was unnecessary. Hence the samples were heated directly 1250 °C to allow for nanocap formation and then to 1700 °C for thermal decomposition and CNT formation. Once the samples were cooled, they were removed, cleaved and imaged using the AFIT SEM. The results of the CNT growth are similar to that of sample set J with a growth height of approximately 250-300 nm. The SEM images showing this growth are shown in Figure 74 and Figure 75. The images were taken at a 45° tilt and the top of the carpet structure can be seen in Figure 75.

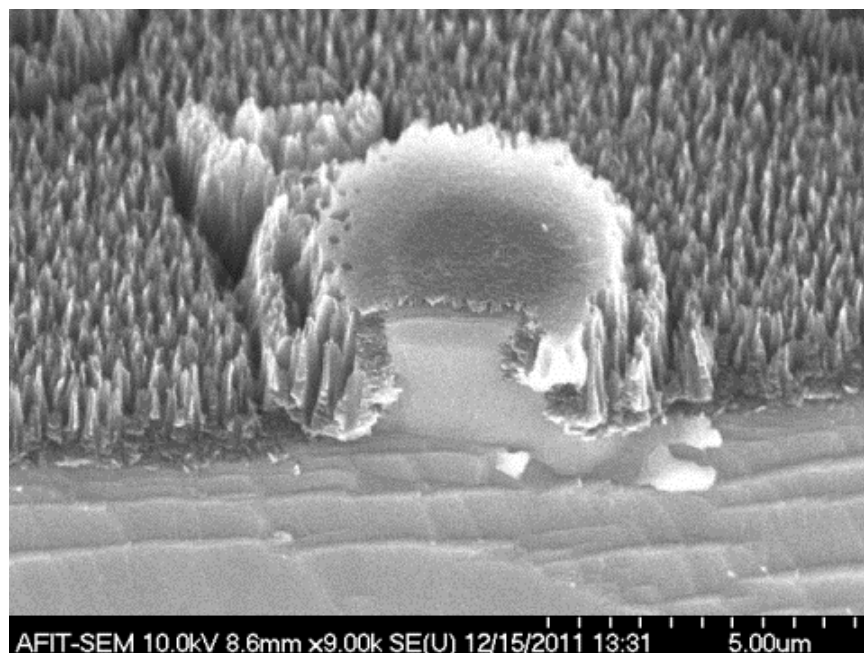


**Figure 74 – SEM image taken at 9k magnification of CNT growth on pillar of from sample set K, 30 minute nanocap formation and 3 hour CNT growth**

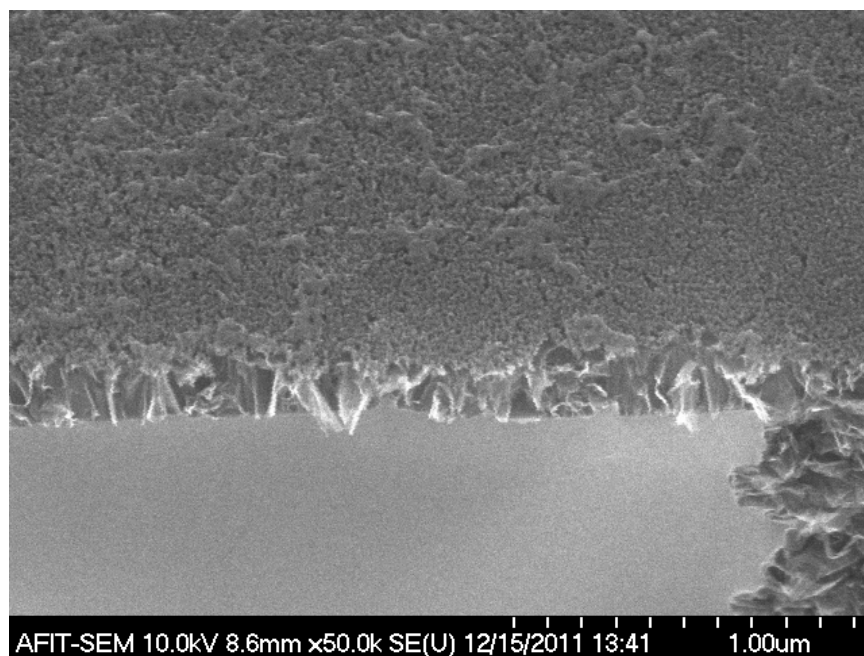


**Figure 75 – SEM image taken at 50k magnification of CNT growth on pillar of from sample set K showing the CNT carpet structure and the surface morphology, 30 minute nanocap formation and 3 hour CNT growth**

### 4.3.3. Sample Set L

Sample set L was processed for CNT growth identical to samples set K, except the growth time was increased to 4.5 hrs. Sample L1 was cleaved and imaged using the AFIT SEM. The SEM image in Figure 76 shows growth on the structure of a height of approximately 640 nm. The CNT in the image appears to be not vertically aligned, however this is most likely due to the cleaving of the structure which removed the CNT layer. The removed layer can be seen in the reduced magnification image in Figure 77. Figure 78 shows an example of the surface morphology of the pillar structures from a 90°.

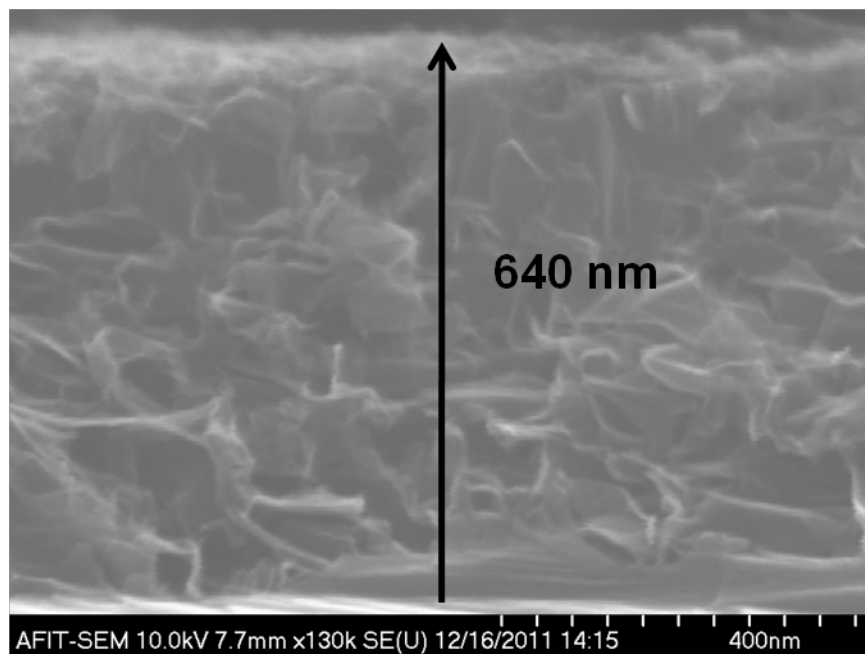


**Figure 76 – SEM image taken at 130k magnification of probable CNT growth on a pillar from sample L1, 30 minute nanocap formation and 4.5 hour CNT growth**

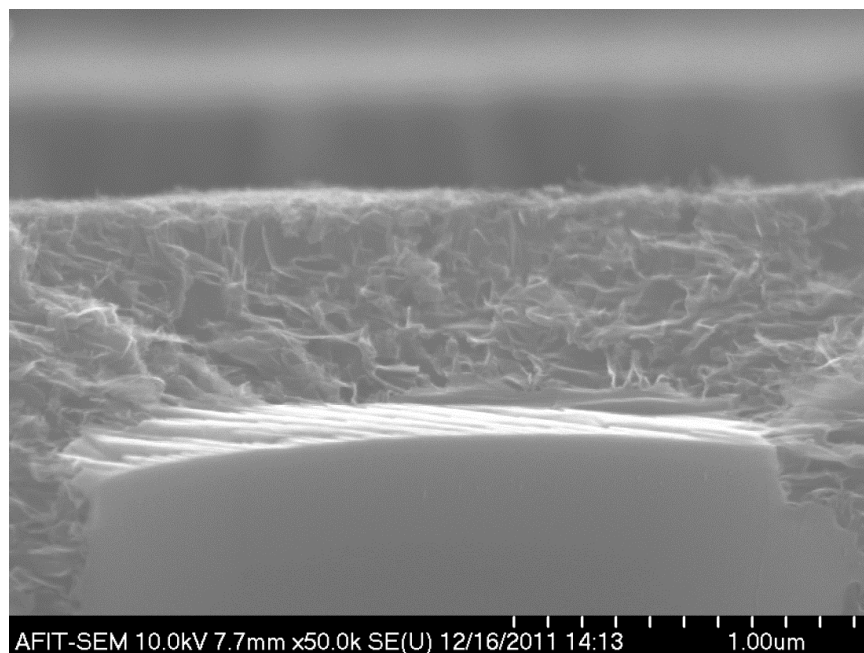


**Figure 77 – SEM image taken at 50k magnification of probable CNT growth region shown in previous figure on a pillar from sample L1, 30 minute nanocap formation and 4.5 hour CNT growth**

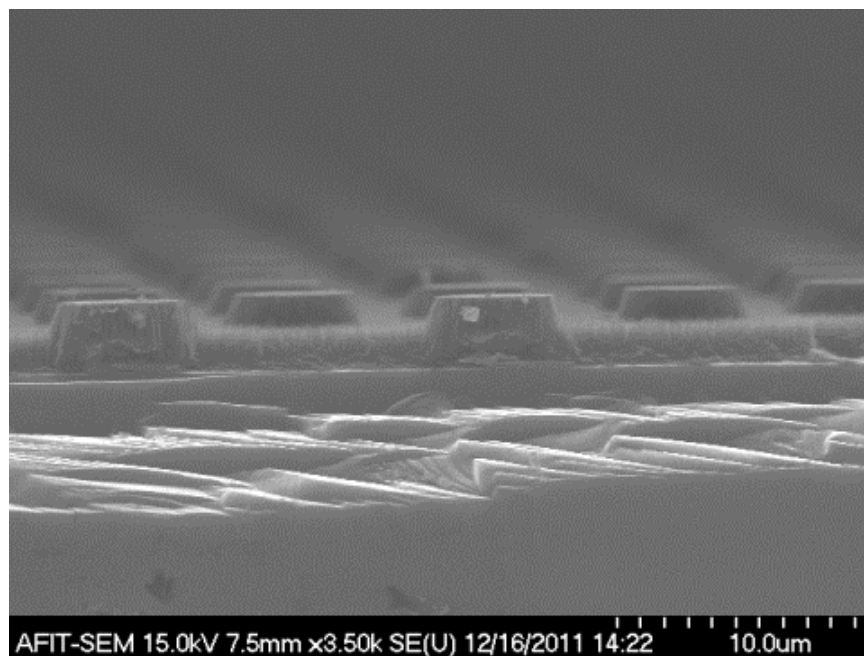


**Figure 78 – SEM image taken at approximately 90 degrees and 3.5k magnification showing the pillar structure found on sample L1**

#### 4.3.4. Sample Set H

Sample set H is the only sample that was patterned using the C-face of the SiC. As such it required less growth time than the previous samples. The samples were heated to 1250 °C for 30 minutes and then 1700 °C for 1 hour. Sample H2 was cleaved and placed imaged in the AFIT SEM. It was only necessary to image one of the patterned samples since each patterned sample contained regions that include an etched portion, an unetched portion, and a patterned portion. The overall patterned region with the unetched pillars and a single cleaved pillar are shown in Figure 79.

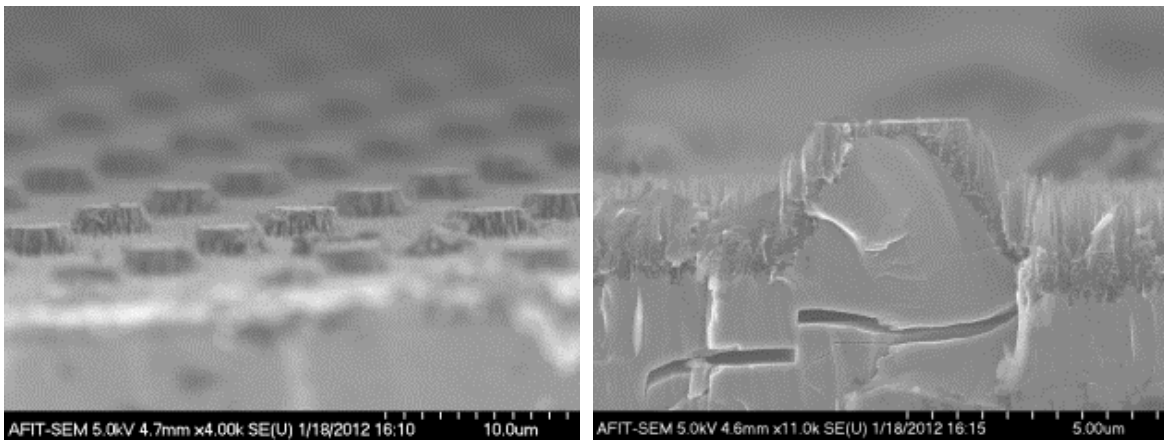


**Figure 79 – SEM images taken at 90 degrees of sample H2, (right) landscape view showing the pillar and spacing, (left) cleaved pillar structure at 11k magnification with CNT growth; C-face SiC with 30 min nanocap formation and 1 hour growth**

A magnified image of the top of the pillar reveals a CNT growth of approximately 270-280 nm.

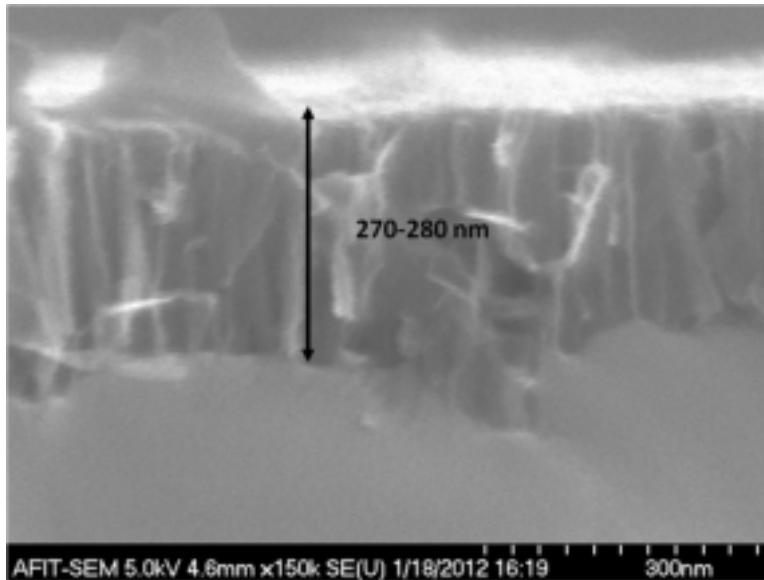


**Figure 80 – SEM image at 150k magnification of CNT growth on top of pillar on sample H2, showing 270-280 nm of growth after 30 min nanocap formation and 1 hour growth**

The unpatterned etched region of the wafer does not appear to have the same CNT growth pattern that was identified with sample J2 above. However, there are areas that appear to have CNT growth from the top of the spikes that appear similar to CNT growth found using a CVD process. This growth is shown at two different magnifications in Figure 81.

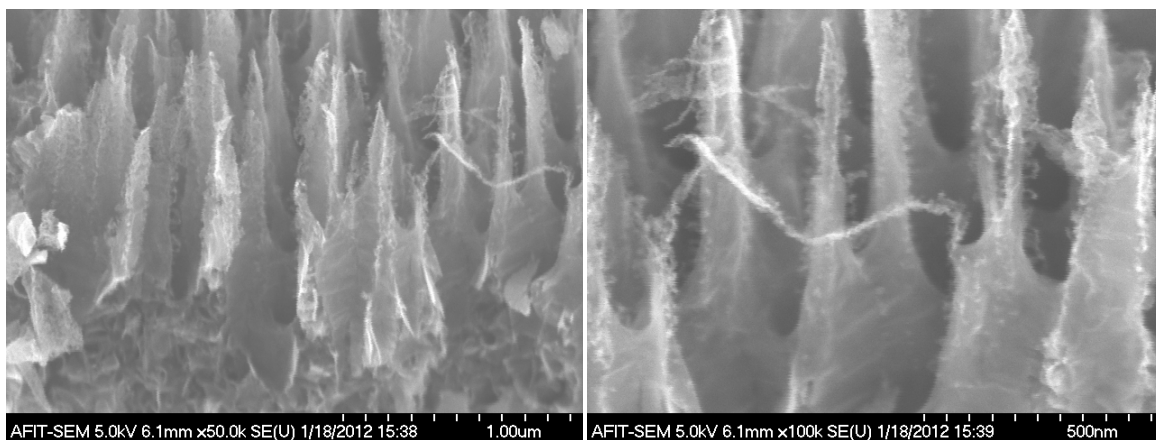


**Figure 81 – SEM image taken of etched surface of sample H2 showing probable CNT growth for 30 min nanocap formation and 1 hour growth, (left) 50k magnification, (right) 100k magnification**

A comparison between etched and unetched regions can be seen at the transition between the two in Figure 82. The large area of the unetched region shows a clear CNT carpet.

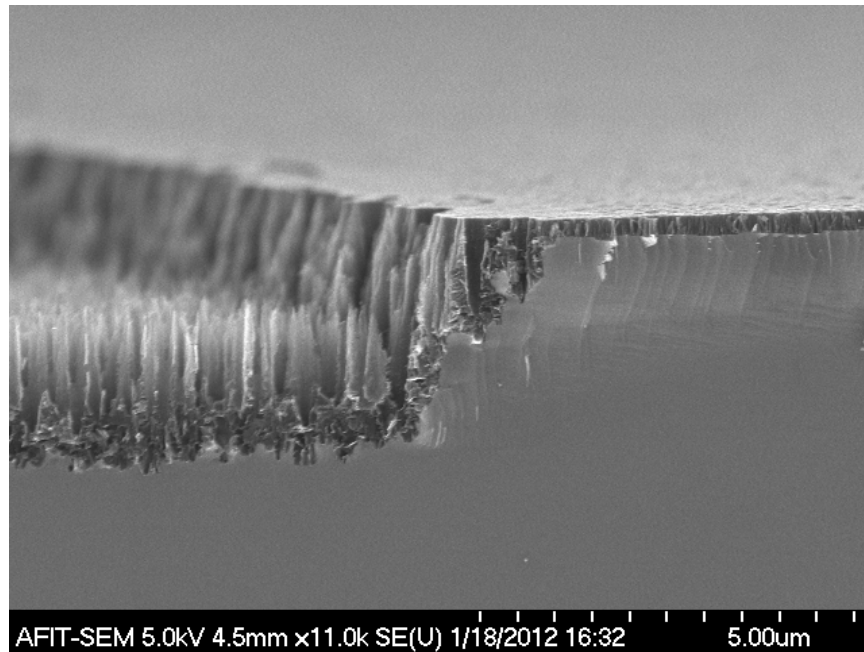


**Figure 82 – SEM image taken at 11k magnification of inter-region boundary between etched region and unetched region, unetched region showing CNT carpet growth**

#### **4.4. Field Emission Results and Analysis**

During field emission testing an applied voltage was applied to an anode and ground applied to the sample. As the voltage was ramped up in steps, current measurements were taken. The data collected during these tests was saved into an output file and labeled with the starting and ending voltage, an apparatus indicator, a run number, and an over-current trip voltage or an off voltage. The files were processed to determine operating parameters: including turn-on voltages, emission current density, and field-enhancement factor, of the samples and allow for comparison between samples in each set and between sample sets.  $E_{TO}$  determined the field required to reach  $1 \mu\text{A}/\text{cm}^2$ , while  $\beta$  was calculated from the linear interpolations of F-N plots. The analysis below is

broken first into individual sample, then sets, and finally into an overall result. Like the surface analysis above, the analysis will start with sample sets J-K and finish with sample set H. Only those samples that showed either a turn-on voltage or provided consistent runs with limited spikes in current are presented graphically. A common theme of the samples was an initial set of runs to condition the surface prior to obtaining measureable emission

#### 4.4.1. Sample Set J – Field Emission

Sample set J, containing two samples J1 and J2, was subjected to 28 different runs using the three different test configurations. This sample set is present by sample and apparatus below.

##### 4.4.1.1. Sample J1 – Field Emission

Sample J1 was tested using both the Alice setup with a 100  $\mu\text{m}$  Teflon insulator with a 1/16 inch diameter ( $.0186\text{ cm}^2$ ) emission area, and the MP setup using the same style insulator. The run parameters for the Alice setup are presented in Table 5 below.

**Table 5 – Sample J1 AT Setup Run Parameters**

Sample	Apparatus	Run	Start Voltage (V/ $\mu\text{m}$ )	Stop Voltage (V/ $\mu\text{m}$ )	Step	Dwell Time	Trip/Off/Hold
J1	AT	1	200	1200	25	2	Trip/975
		2	500	1200	20	2	Trip/950
		3	700	950	5	2	Trip/945
		4	400	1000	5	2	Trip/885
		5	400	1000	25	2	Trip/900

Using the AT (Alice w/Teflon) setup, sample J1 was subjected to 5 runs. Although data was collected for runs 3 and 4, the data collected contained frequent current spikes making it unusable for analysis. For runs 1, 2, and 5, the samples had subsequent

decreasing measured ETO of 8.01 V/mm, 6.9 V/mm, and 6.5 V/mm, respectively. The current density plot for runs 1, 2, and 5 is shown in Figure 83. The decrease in ETO is the result of impurities on the emitter surface or defects being removed during the emission surface.

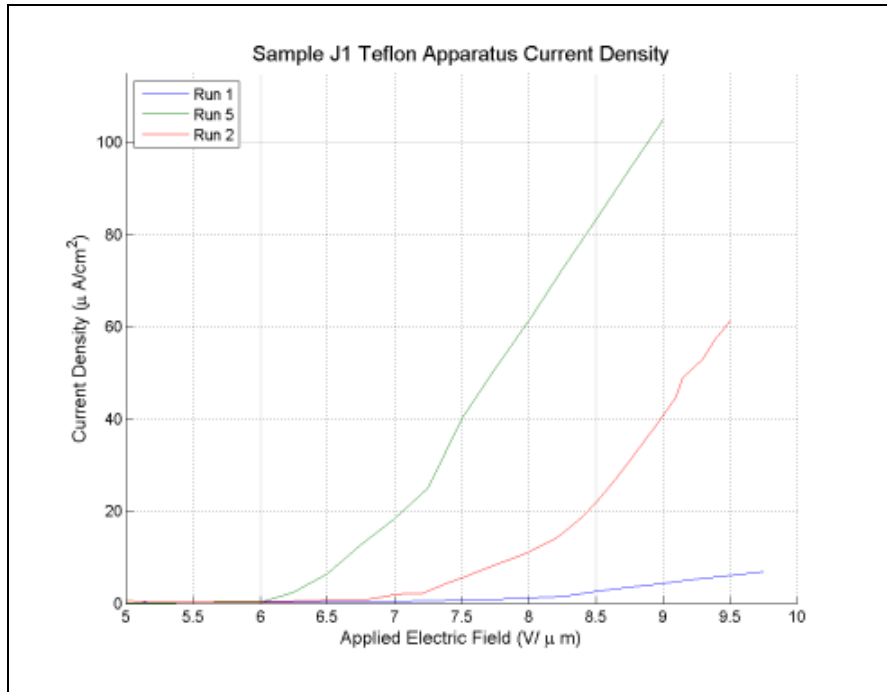


**Figure 83 – Field emission testing current density (J-E) curves for sample J1, AT setup runs 1, 2, and 5**

The maximum measured current density was 26.79  $\mu\text{A}/\text{cm}^2$  at 9.7 V/ $\mu\text{m}$  for run 1, 287.16  $\mu\text{A}/\text{cm}^2$  at 9.4 V/ $\mu\text{m}$  for run 2, and 269.23  $\mu\text{A}/\text{cm}^2$  at 9.0 V/ $\mu\text{m}$  for run 5. To compare the current density of the runs directly, the current densities of each run at the selected field of 8.0 V/ $\mu\text{m}$  were 1.19  $\mu\text{A}/\text{cm}^2$ , 12.8  $\mu\text{A}/\text{cm}^2$ , and 80.4  $\mu\text{A}/\text{cm}^2$ . The plots in Figure 84 are linear, which indicates that the emission from the sample is from field emission. The field enhancement factor can be derived from taking the slope of the linear interpolation of the plots. The field enhancement factors for each run were 635 for run 1, 568 for run 2, and 1039 for run 5.

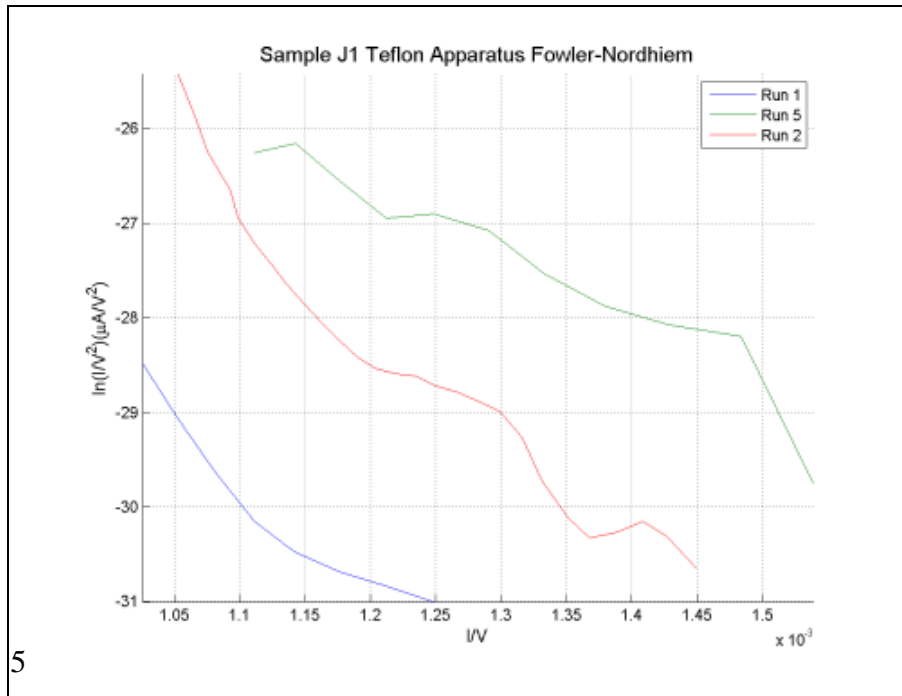


**Figure 84 – Field emission testing Fowler-Nordheim plots for sample J1, AT setup runs 1, 2, and 5**

The test parameters for sample J1 using the MP test setup are given in Table 6 below. The sample was subjected to 3 runs with the test setup tripping on the first run at 8.9 V/μm. The collected result from run 3 showed errant spikes in the measured current and as such was not plotted as an IV curve.

**Table 6 – Sample J1 MP Setup Run Parameters**

Sample	Apparatus	Run	Start Voltage	Stop Voltage	Step	Dwell	Trip/Off/Hold
J1	MP	1	500	900	10	2	Trip/890
		2	500	800	10	2	
		3	500	800	10	2	

Runs 1 and 2, shown in Figure 85, showed consistent current density to applied field (J-E) characteristics with measured  $E_{TO}$  of 6.6 V/μm for run 1 and 6.5 V/μm for run 2. The maximum current density for was 170 μA/cm<sup>2</sup> at 8.6 V/μm for run 1 and 166 μA/cm<sup>2</sup> at

7.2 V/ $\mu\text{m}$  for run 2. At 7 V/ $\mu\text{m}$ , runs 1 and 2 had current densities of 13.9  $\mu\text{A}/\text{cm}^2$  and 94.3  $\mu\text{A}/\text{cm}^2$  respectively.

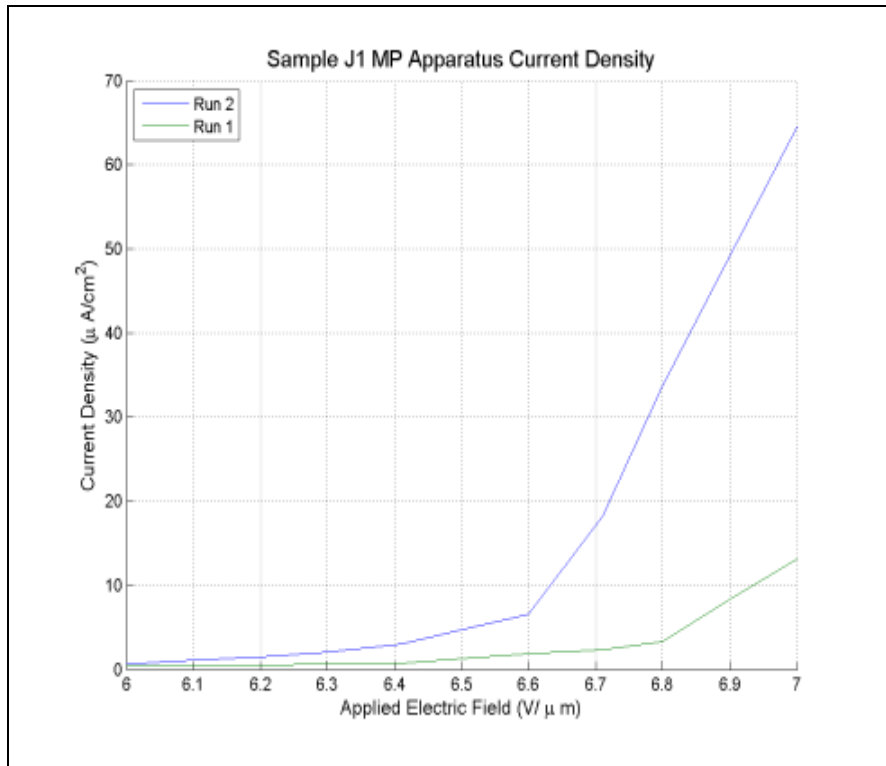


**Figure 85 – Field emission testing current density (J-E) curves for sample J1, MP setup runs 1 and 2**

The F-N plot, in Figure 86, for sample J1 using the MP apparatus show a linear correlation at applied fields below 7 V/ $\mu\text{m}$  for both runs 1 and 2 which is indicative of field emission sources. A linear fit of the applied fields below 7 V/ $\mu\text{m}$  was used to determine the field enhancement factor. Run 1 had a field enhancement factor of 714 and run 2 had a field enhancement factor of 975.

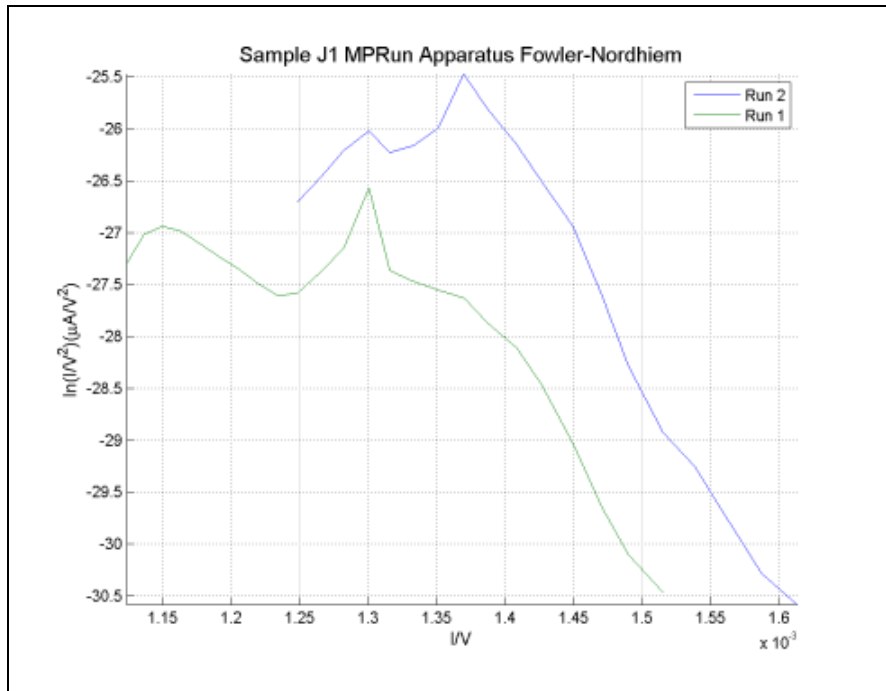


**Figure 86 – Field emission testing Fowler-Nordheim plots for sample J1, MP setup runs 1 and 2**

#### 4.4.1.2. Sample J2 – Field Emission

Sample J2 was test using the Alice setup with an air gap of 215  $\mu\text{m}$ , the Alice setup with a 100  $\mu\text{m}$  Teflon insulator with a 1/16 inch diameter (.0186  $\text{cm}^2$ ) emission area, and the MP setup using the same insulator. Sample J2 was tested using Alice with air gap setup using the parameters in Table 7. Both run 5 and 7 were paused during their runs to provide information about current stability of the devices and is presented later.

**Table 7 – Sample J2 AA Setup Run Parameters**

Sample	Apparatus	Run	Start Voltage	Stop Voltage	Step	Dwell	Trip/Off/Hold
J2	AA	1	500	2000	25	2	
		2	1000	2000	25	2	
		3	1000	2000	10	2	
		4	1000	2000	10	2	
		5	1000	2000	10	2	Hold/1810
		6	1000	2000	10	2	
		7	1000	2000	10	2	Hold/2000

Because of configuration of the test setup, it was not possible to determine the current density from the measured current. Consequently, the turn-on field could not be determined directly. However, the IV plot in Figure 87 for runs 1-4 and run 6, shows a value of approximately 1200 V (5.5 V/ $\mu\text{m}$ ) for the turn-on voltage. The IV plot also shows that the runs after run 1 show have higher currents at lower voltages. For example, at an applied voltage of 1500 V (6.97 V/ $\mu\text{m}$ ), the runs 1-4 and 6 have currents 0.274, 1.01, 1.23, 1.70, and 1.06  $\mu\text{A}$ . This can be attributed to run 1 pre-conditioning the emission surface allowing the increased current. The decrease in run 6 is most likely due to it being completed directly after a long hold.

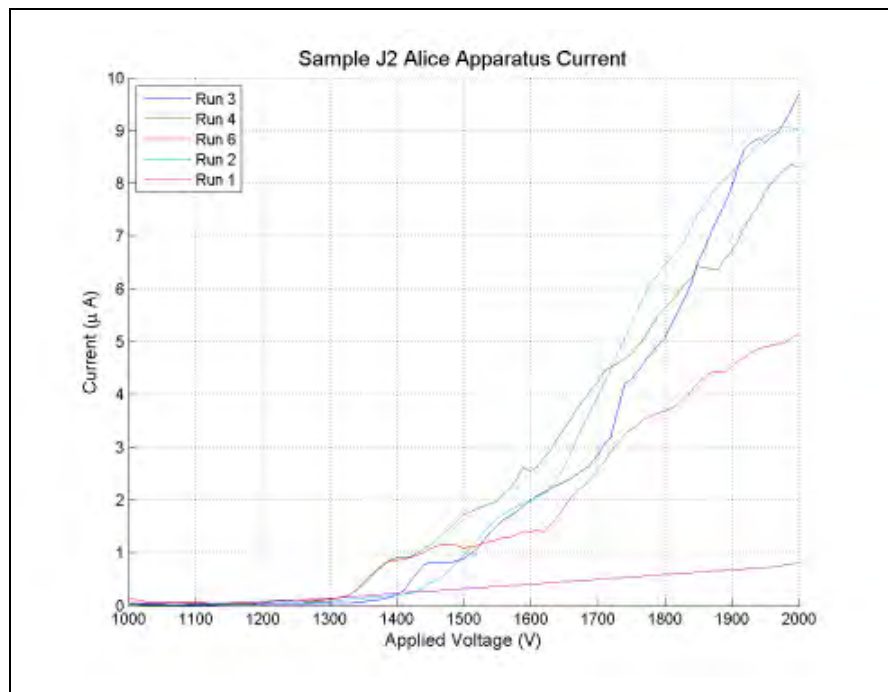


**Figure 87 – Field emission testing current (IV) curves for sample J2, AA setup runs 1-4 and 6**

Because the F-N plot can utilize either the current density or current, the calculated field enhancement factor can still be obtained from without knowing the current density. The F-N plot, in Figure 88, for the above run show a linear correlation,

meaning the dominant emission mechanism is electron field emission. Using the slope of a linear fit to the F-N plots, the calculated field enhancement factor for runs 1-4 and 6 are 792, 1165, 1369, 1904, and 2384.

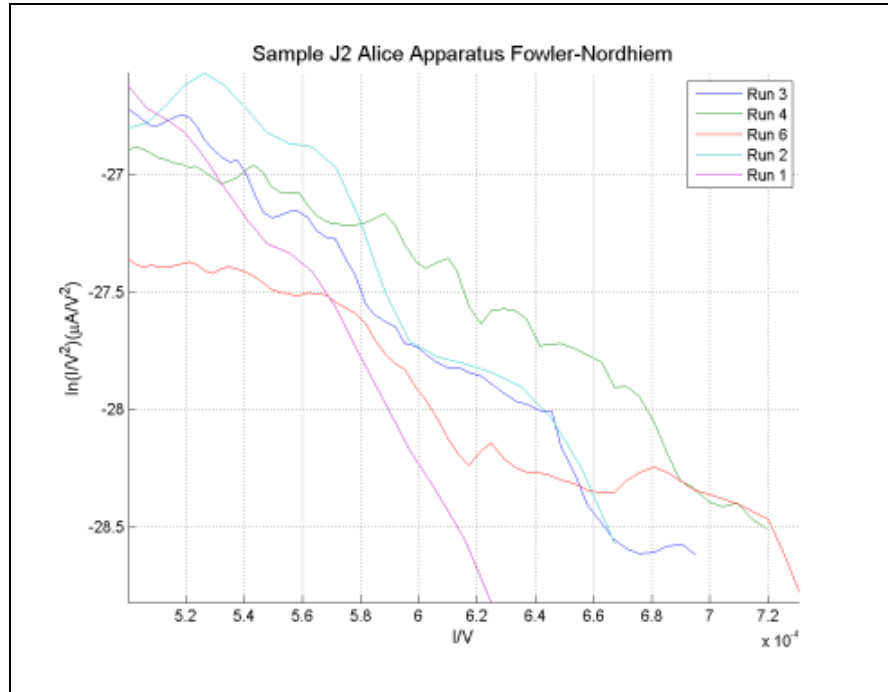


**Figure 88 – Field emission testing Fowler-Nordheim plots for sample J2, AA setup runs 1-4 and 6**

Sample J2 was also subject to field emission testing utilizing the Alice setup using a Teflon spacer. The run configurations for this setup are given in Table 8. Of these runs, the first 3 appear to precondition the surface as they have high turn-on voltages or tripped due to voltage-breakdown and arcing before turning on.

**Table 8 – Sample J2 AT Setup Run Parameters**

Sample	Apparatus	Run	Start Voltage	Stop Voltage	Step	Dwell	Trip/Off/Hold
J2	AT	1	200	1800	25	2	Trip/1625
		2	1200	1700	25	2	
		3	1200	1800	10	2	Trip/1730
		4	800	1500	10	2	
		5	200	1500	10	2	Trip/1290
		6	200	1200	10	2	Trip/1160

The J-E plot in Figure 89 shows the performance of the sample over runs 1-6. The plot shows clear device emission for runs 4-6 with  $E_{TO}$  of 8.01, 5.4, and 6.3 V/ $\mu$ m. During run 6, the emissions appear to turn-on then hold a constant current and then increase again. This could be attributed to a portion of the emission surface ceasing to emit and another area contributing to the overall emission. At a selected applied field of 12 V/ $\mu$ m, the current density of runs 4-6 is 18.1, 247, and 266  $\mu$ A/cm<sup>2</sup>.

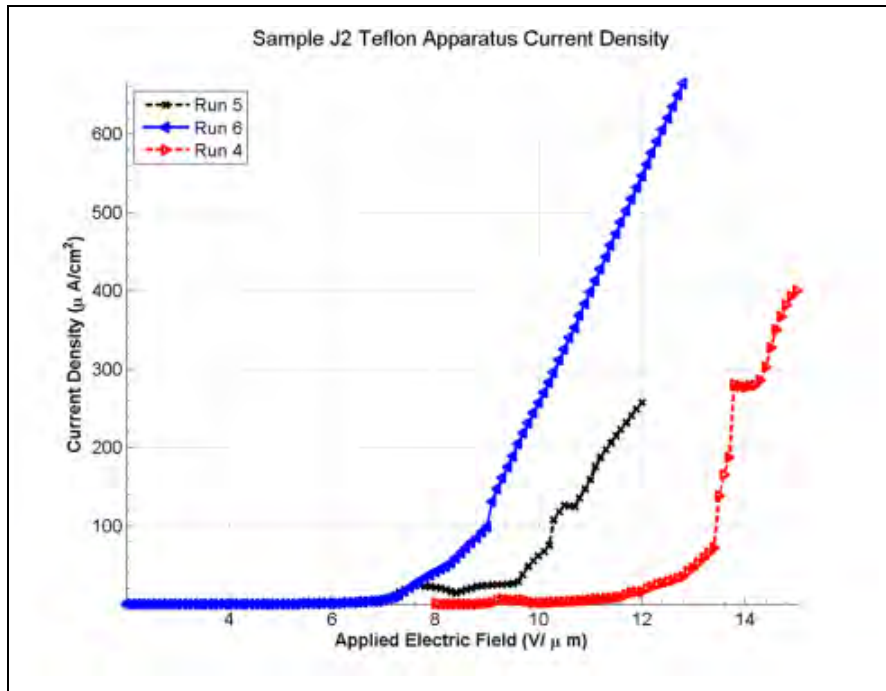


**Figure 89 – Field emission testing current density (J-E) curves for sample J2, AT setup runs 4-6**

The F-N plot in Figure 90 show the overall trend of the curves is linear which indicative of field emission. From this plot, the field enhancement factor for runs 4-6 of sample J2 can be calculated as 593, 1305, and 1305. Although the J-E plot for runs 5 and 6 are different, the field enhancement factor is identical.

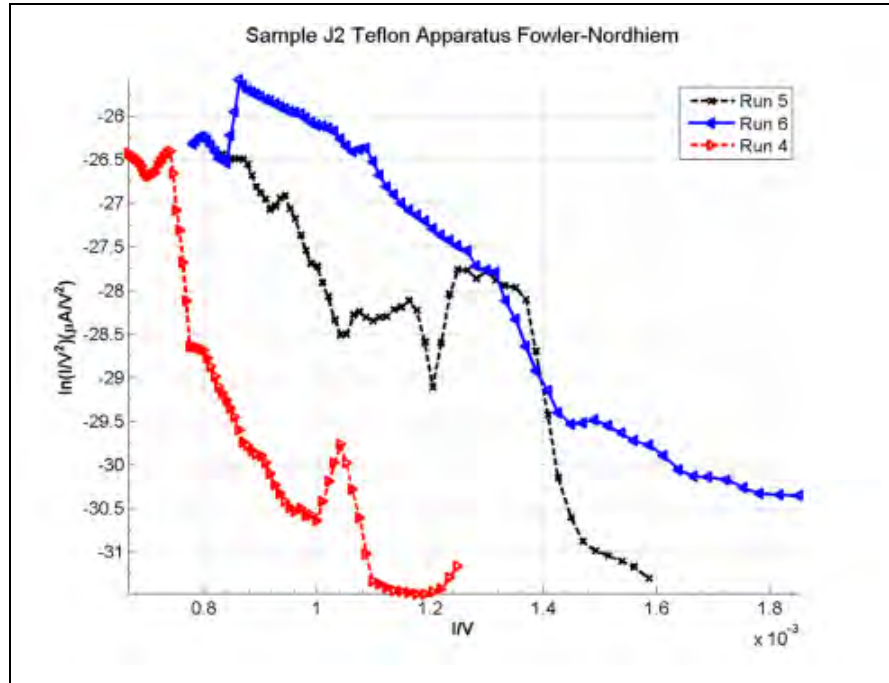


**Figure 90 – Field emission testing Fowler-Nordheim plots for sample J2, AT setup runs 4-6**

Finally sample J2 was tested using the MP apparatus. Of the three test setups, with parameters given in Table 9, the runs performed using the MP apparatus were the most inconsistent. The reason for this inconsistency is unknown, but could be from poor contact between the anode and the Teflon spacer, or poor structure in the emission area.

**Table 9 – Sample J2 MP Setup Parameters**

Sample	Apparatus	Run	Start Voltage	Stop Voltage	Step	Dwell	Trip/Off/Hold
J2	MP	1	500	1500	10	2	Trip/1175
		2	500	1200	10	2	Trip/1025
		3	500	825	10	4	
		4	250	700	10	4	
		5	250	625	5	4	
		6	250	625	10	4	

In the J-E curves for runs 3 and 6 shown in Figure 91, the current density would reach a peak, the sample would quit emitting and then begin to emit again. On runs 3 and 6, the samples begin emitting immediately after the run begin, so it is not possible to determine the exact turn-on voltages. For run 2,  $E_{TO}$  is  $6.71 \text{ V}/\mu\text{m}$ .

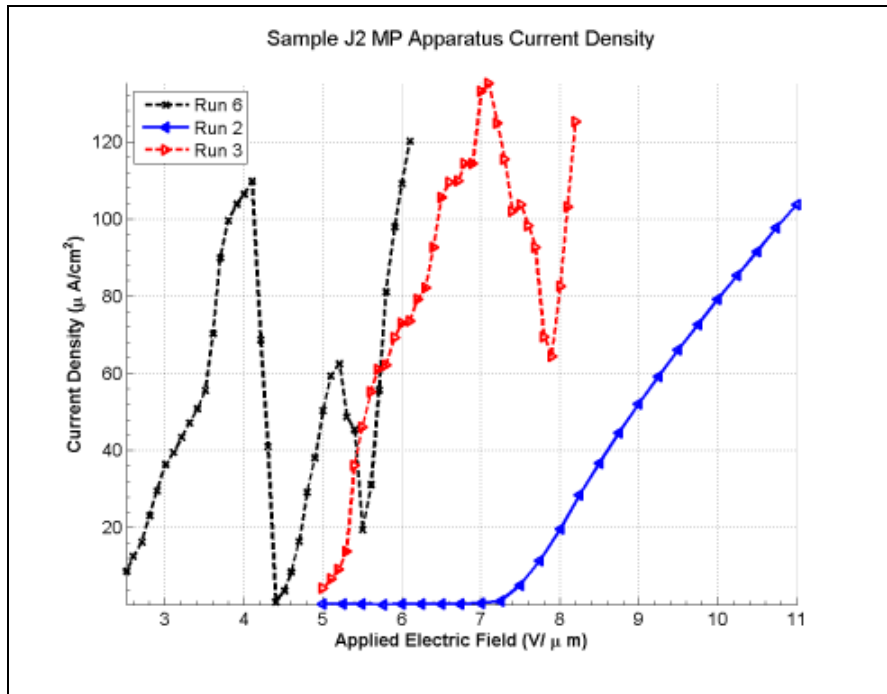


**Figure 91 - Field emission testing current density (J-E) curves for sample J2, MP setup runs 2, 3 and 6**

Like the J-E curves, the F-N curves, found in Figure 92, reveal areas where the sample is not emitting or where field emission is not the primary method of emission. The field-enhancement factors extracted from the F-N curves are from sections that show the linear characteristic of field emission, for example between 2.5 V/ $\mu\text{m}$  and 4 V/ $\mu\text{m}$  of run 6. The field enhancement factors for runs 2, 3, and 6 are 2423, 2180, and 8007.

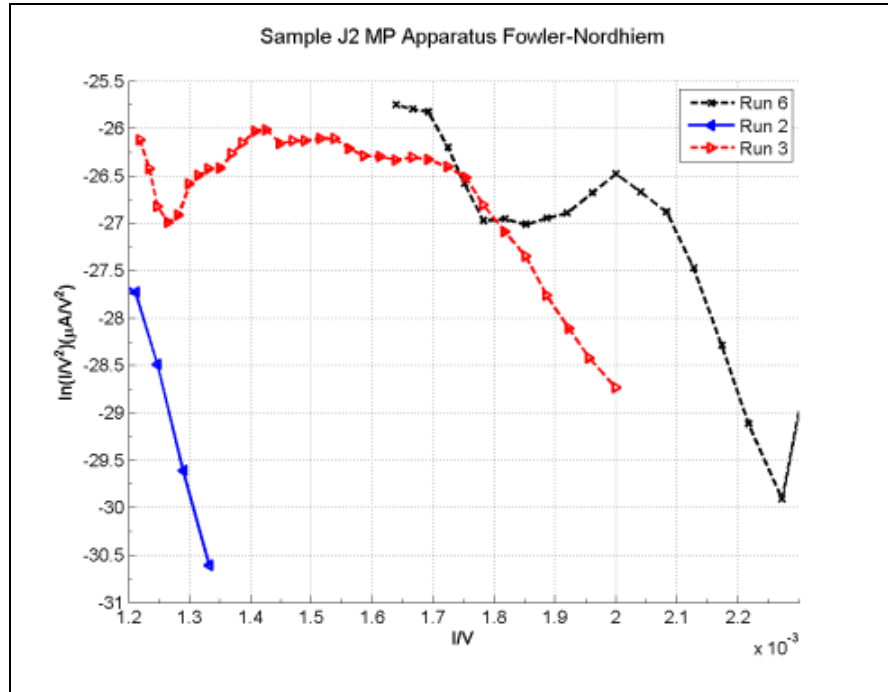


**Figure 92 – Field emission testing Fowler-Nordheim plots for sample J2, MP setup runs 2, 3, and 6**

#### 4.4.2. Sample Set K – Field Emission

Sample set K is comprised of three samples labeled K1-K3. The entire set was test over 43 different runs using the three different test configurations. This sample set’s results are presented by sample and apparatus in the following sections.

#### 4.4.2.1. Sample K1 – Field Emission

Sample K1 was tested using both the Alice setup with an air gap (AA) and the MP setup using the Teflon spacer. The parameters for the Alice setup are presented in Table 10 below.

**Table 10 – Sample K1 AA Setup Run Parameters**

Sample	Apparatus	Run	Start Voltage	Stop Voltage	Step	Dwell	Trip/Off/Hold
K1	AA	1	500	1250	25	4	
		2	500	2000	25	4	Trip/1300
		3	500	1300	20	4	Hold/1040
		4	500	1500	100	120	
		5	1200	1300	10	2	Hold/1290

Of the five runs performed on sample K1 only three were are presented for field emission analysis. Runs 3 and 5, which were subjected to a voltage hold, will used later in determination of the samples current stability. Since sample K1 was tested using the AA apparatus, the current density value could not be accurately calculated since the emission area is unknown. However, the IV curves are presented in Figure 93.

An investigation of the curves in Figure 94 reveals estimated  $V_{TO}$  of 800, 650, and 600V<sub>DC</sub> for run 1, 2, and 4. The corresponding applied fields, using the calculated gap of 215  $\mu\text{m}$ , for runs 1, 2, and, are 3.95, 3.02, and 2.80 V/ $\mu\text{m}$ . The corresponding F-N plot for the three runs is shown in Figure 95. Since the plot utilizes current rather than current density, the field enhancement factor can be determined from the slope of the linear best fit of the plots. The calculated field enhancement factors for sample K1 using the AA setup were 1521, 3463, and 4143 for runs 1, 2, and 4 respectively.

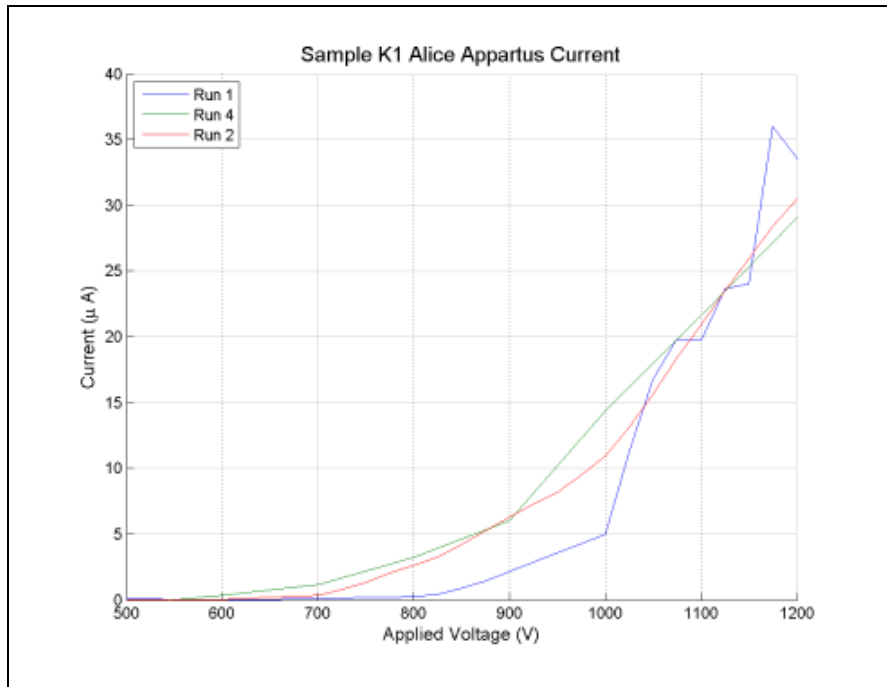


Figure 93 – Field emission testing current (IV) curves for sample K1, AA setup runs 1, 2, and 4

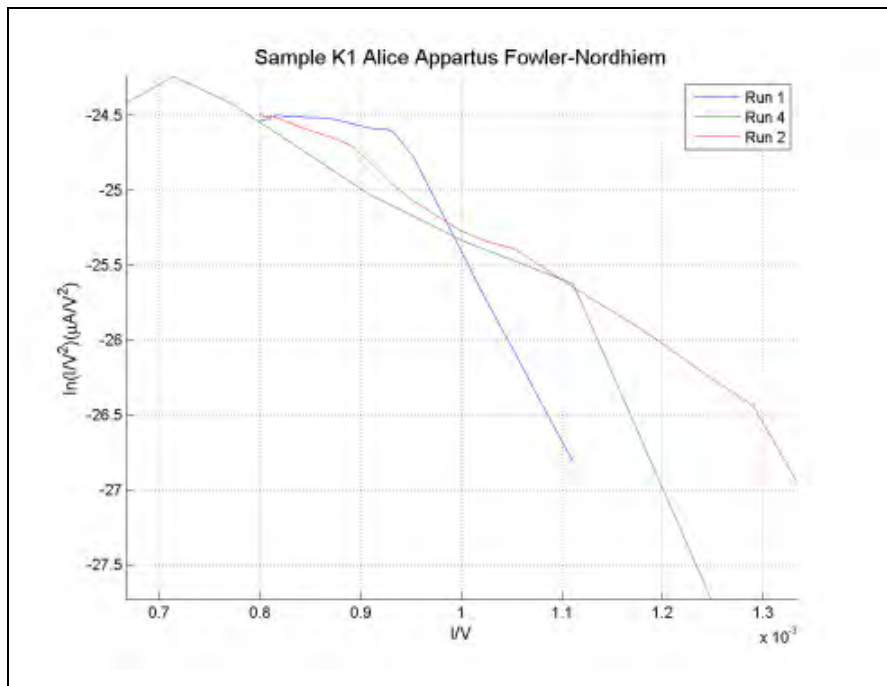


Figure 94 – Field emission testing Fowler-Nordheim plots for sample K1, AA setup runs 1, 2 and 4

Using the MP setup, 11 runs were conducted on sample K1. Of the 11 runs, only runs 2, 3, 4, 7 and 11 are analyzed below. The remaining runs involved holds of varying lengths which can be used to determine current stability of the samples. The summary of the runs is presented in Table 11Table 11.

**Table 11 – Sample K1 MP Setup Parameters**

Sample	Apparatus	Run	Start Voltage	Stop Voltage	Step	Dwell	Trip/Off/Hold
K1	MP	1	100	1000	25	2	Hold/650
		2	100	600	20	2	Off/290
		3	100	400	10	2	
		4	100	600	5	2	Off/470
		5	100	450	5	2	Hold/450
		6	100	450	5	2	Off/275
		7	100	400	5	1	
		8	200	400	5	1	Hold
		9	200	450	10	4	Hold/400
		9.1	200	600	10	4	Hold/540
		11	200	600	10	4	

The J-E curves for runs 2-4, 7 and 11 are shown in Figure 95. The curves reveal that the emitting surface was very poor except on runs 2 and 11. However, what is not shown in the plot is the instability of run 2 beyond approximately 4.25 V/ $\mu\text{m}$ . Run 2 reached a peak current density of 1.76 mA/cm<sup>2</sup> before essential turning off and emitting only temporarily for the entire run. Run 11 obtained a E<sub>TO</sub> of 4.00 V/ $\mu\text{m}$  but did not begin to emit as a field emitter until beyond 4.5 V/ $\mu\text{m}$ .

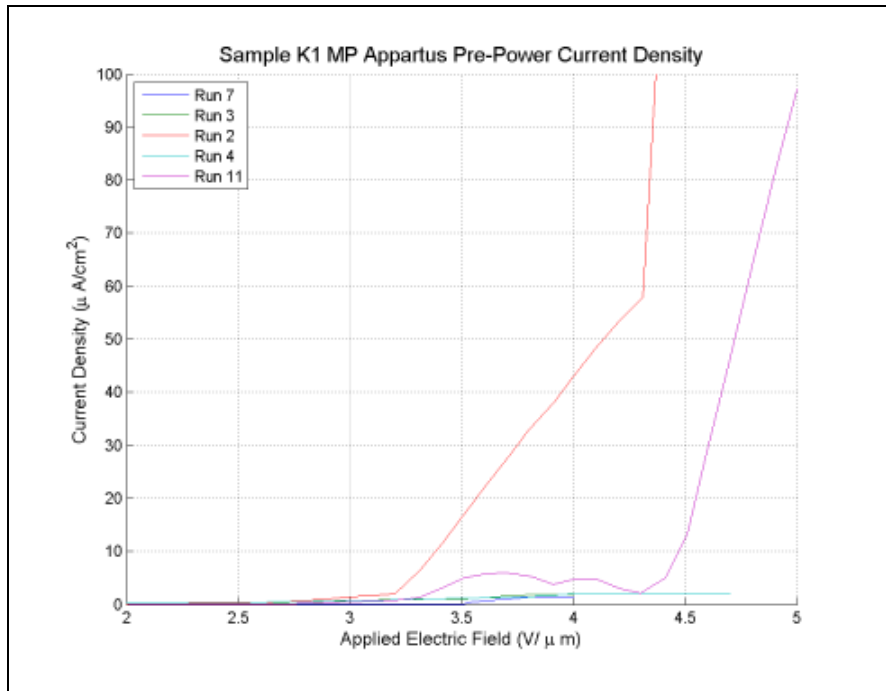


**Figure 95 – Field emission testing current density (J-E) curves for sample K1, MP setup runs 2-4, 7, and 11**

The corresponding F-N plot, Figure 96, for these samples reveals that field emission is not the dominant source of electron being emitted. However, some portions of all the curves are linear once the turn-on field has been reached. As such a estimated field enhancement factor can be derived from the linear estimate of those regions. In the case of sample K1 using the MP setup, the field enhancement factors for all plotted runs are 1160 for run 2, 3790 for run 3, 1493 for run 4, 2255 for run 7, and 1710 for run 11. Overall the sample showed no predictability between runs, which meant that there was patterned increase or decrease in  $\beta$  for consecutive runs.

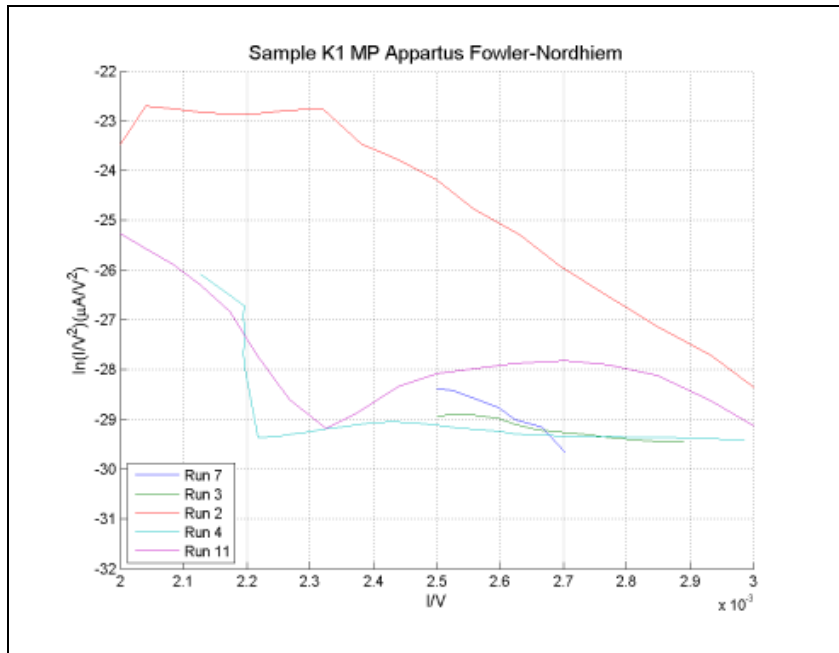


**Figure 96 – Field emission testing Fowler-Nordheim plots for sample K1, MP setup runs 2-4, 7, and 11**

#### 4.4.2.2. Sample K2 – Field Emission

Sample K2 was test for field emission using the AT setup and the MP setup. The test parameters using the AT setup are shown in Table 12.

**Table 12 - Sample K2 AT Setup Run Parameters**

Sample	Apparatus	Run	Start Voltage	Stop Voltage	Step	Dwell	Trip/Off/Hold
K2	AT	1	400	1000	25	2	
		2	1400	2000	10	2	Trip/1910
		3	1400	2000	10	2	Trip/1860
		4	1400	1800	25	2	
		5	1000	1900	10	2	
		6	1200	1900	25	2	

Runs 2-6 were all plot to show their J-E curves in Figure 97. What the curves show is that although the samples seems to be emitting current the high applied voltages do not drastically change the current density. The curves themselves mimic the early readings of the software, which showed a slowly increasing current as voltage increased.

However, those current changes were in the  $10^{-8}$  A range and not the ranges shown in Figure 97. From these curves and the nearly flat F-N plot found in Figure 98, it can be concluded that field emission was not observed during the set up runs.

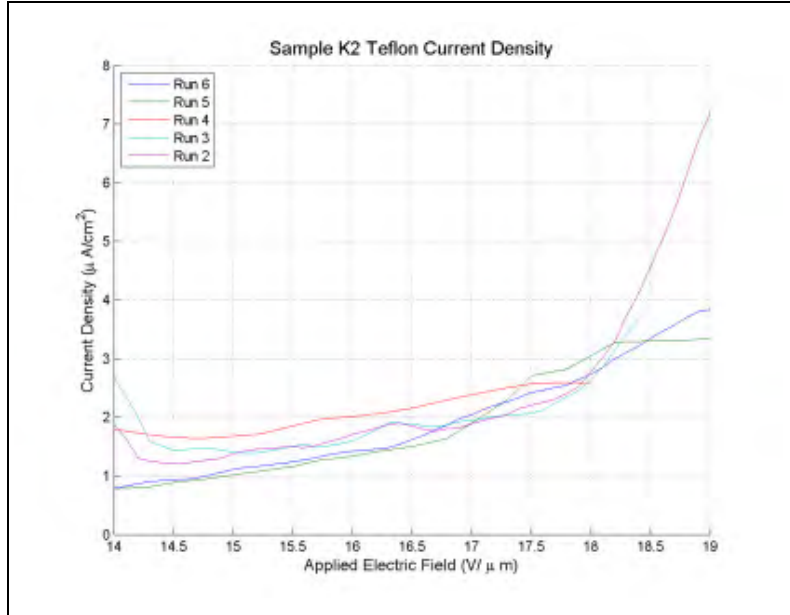


**Figure 97 – Field emission testing current density (J-E) curves for sample K2, AT setup runs 2-6**

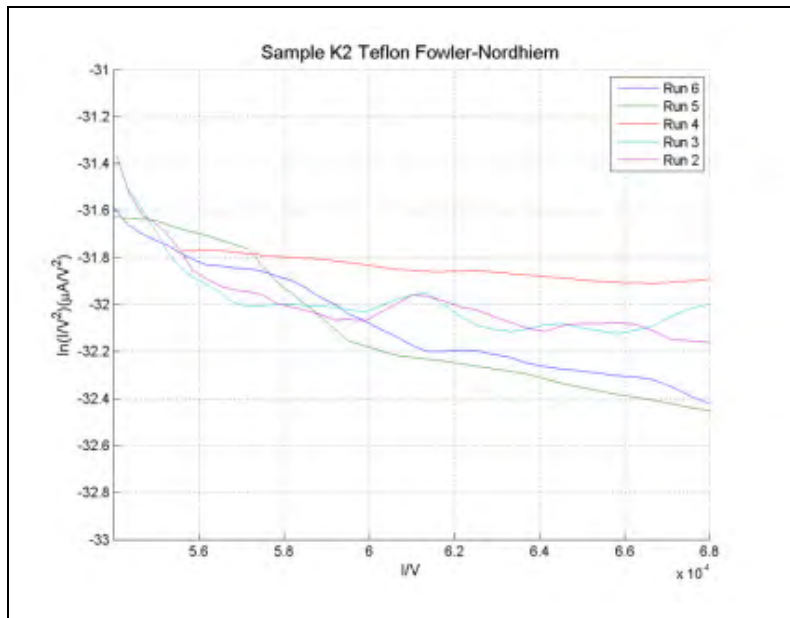


**Figure 98 – Field emission testing Fowler-Nordheim plots for sample K2, AT setup runs 2-6**

Using the parameter listed in Table 13, sample K2 was also tested using the MP setup.

**Table 13 – Sample K2 MP Setup Parameters**

Sample	Apparatus	Run	Start Voltage	Stop Voltage	Step	Dwell	Trip/Off/Hold
K2	MP	1	700	1200	25	2	
		2	700	1200	25	2	
		3	500	1000	10	2	
		4	500	900	5	4	
		5	500	1000	5	2	
		6	750	1000	5	10	
		7	750	1600	10	2	Trip/1350
		8	750	1600	10	2	Trip/1100

The J-E curves in Figure 99, all appear to have a common theme. The curves show a turn increase and then stop a certain current density. The lack of increased emission may be because of graphitic layers or other impurities inside or on top of the CNT structures. Run 7, which tapers between 9.1 and 12 V/ $\mu\text{m}$ , is the only sample that increased after stopping at certain current. A zoomed in view of the data, shown by the inset of Figure 99, shows the turn-on field and increasing current density curves common to CNT field emission.

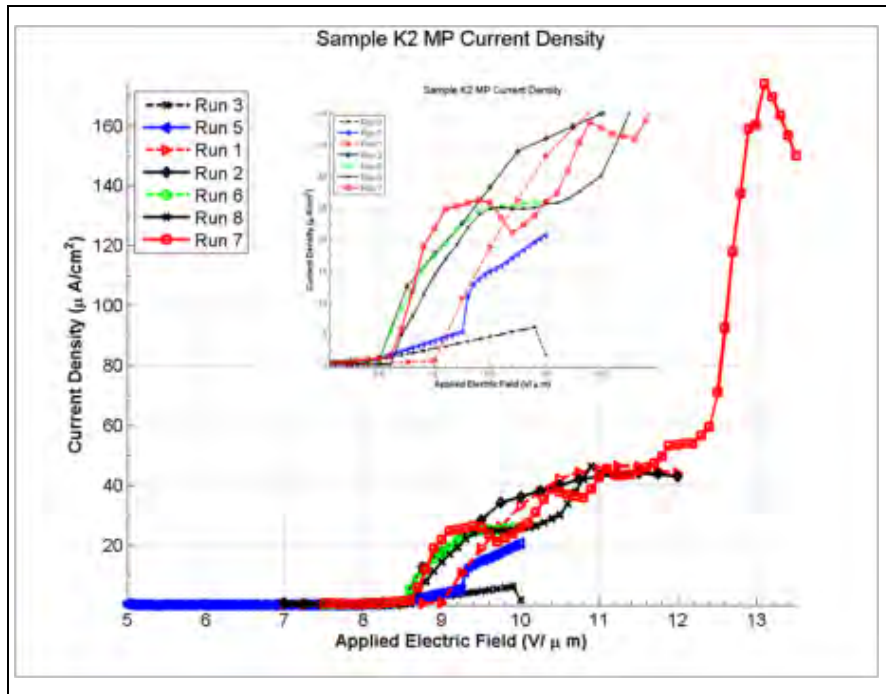


**Figure 99 – Field emission testing current density (J-E) curves for sample K2, MP setup runs 1-3 and 5-8**

The turn-on fields for each on the runs shown in Figure 99 are: 9.25 V/ $\mu\text{m}$  for run 1, 8.75 V/ $\mu\text{m}$  for run 2, 8.6 V/ $\mu\text{m}$  for run 3, 8.55 V/ $\mu\text{m}$  for run 5, 8.6 V/ $\mu\text{m}$  for run 6, 8.9 V/ $\mu\text{m}$  for run 7, and 8.4 V/ $\mu\text{m}$  for run 8. With the exception of run 7, the trend of the  $E_{\text{TO}}$  for the samples decreased. The F-N plots in Figure 100 also shows the current remaining near constant after a certain applied voltage. To obtain the field enhancement factor, the linear fit was taken from the lower applied voltage region of the plot. In the case of sample K2, this region is between  $E_{\text{TO}}$  and 9 to 10 V/ $\mu\text{m}$ . The results of the  $\beta$  calculations range between 250 to 1700 with no apparent correlation between runs. Sample K2 can therefore be characterized as a poor emitter which can be attributed to its poor structure. This result also confirms that the data collected using the AT setup.

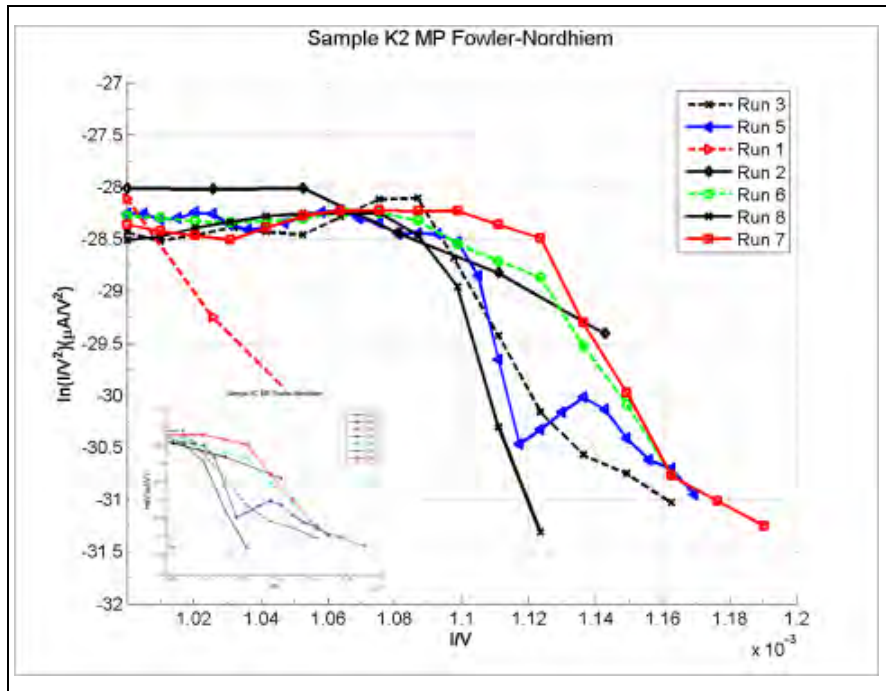


**Figure 100 – Field emission testing Fowler-Nordheim plots for sample K2, MP setup runs 1-3 and 5-8**

#### **4.4.2.3. Sample K3 – Field Emission**

Sample K3 was test using only the MP setup. The parameters of all the completed runs are highlighted in Table 14. Run 1 was used to test the stability of the current over time and is not used in the J-E and F-N plots. During runs 7 and 8, the sample was run until it tripped to find the current and voltage limits. These two runs provide delineation between two set of data, a pre-trip set and a post-trip set.

**Table 14 – Sample K3 MP Setup Parameters**

Sample	Apparatus	Run	Start Voltage	Stop Voltage	Step	Dwell	Trip/Off/Hold
K3	MP	1	100	350	10	4	Hold/310
		2	100	350	10	4	
		3	50	300	5	2	
		4	50	300	5	1	
		5	50	600	10	2	
		6	200	500	25	2	
		7	300	700	20	2	Trip/630
		8	250	650	20	2	Trip/630
		9	250	500	15	2	
		10	250	500	10	4	
		11	250	500	10	2	
		12	250	500	25	4	

Runs 2-5 are lumped into the pre-trip runs. The J-E curves for these runs are shown in the left side of Figure 101. While the post-trip runs 9-12 are shown on the right side. Both curves show K3 as relative inconsistent performer as an emitter surface. With the exception of run 4 in the pre-trip plot and run 10 in the post trip plot, the sample does not appear to reach stable emission. The result of the turn-on voltages show that the device reached the turn-on current density of  $1 \mu\text{A}/\text{cm}^2$  at much earlier fields than after the setup experience and over-current trip. The  $E_{\text{TO}}$  for the pre-trip region ranged from 1-1.5  $\text{V}/\mu\text{m}$ , while the  $E_{\text{TO}}$  for the post trip ranged from 3.2 to 4.6  $\text{V}/\mu\text{m}$ . The increase in  $E_{\text{TO}}$  from pre-trip to post-trip is most likely the degradation of the emitter surface during the over-current trip.

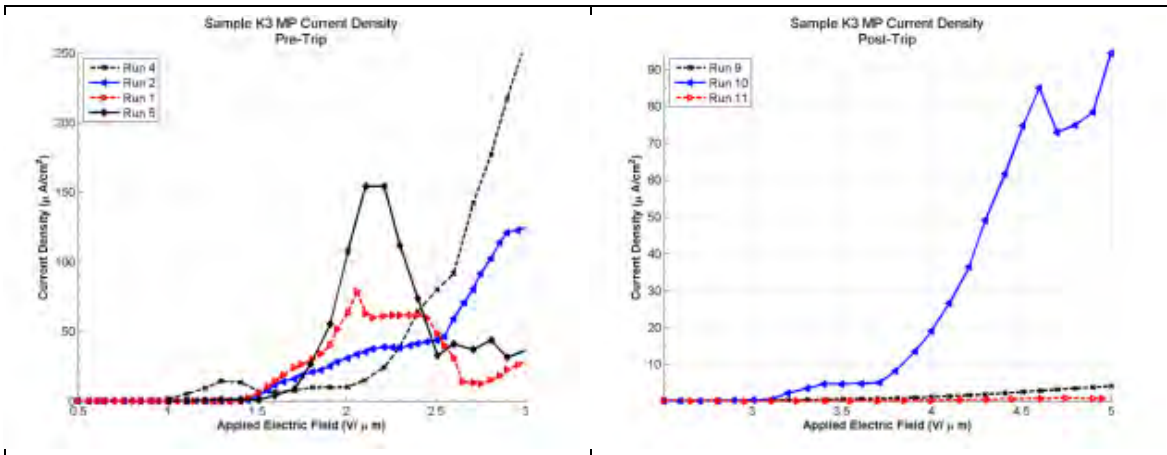


**Figure 101 – Field emission testing current density (J-E) curves for sample K3, MP setup runs (left) 1, 2, 4, and 5 (right) runs 9-11**

Like the J-E curves, the F-N plots can be compared side by side to examine the difference between pre and post-trip runs. The pre-trip F-N plot in the left-side of Figure 102 again shows the inconsistent field emission from the sample prior to the setup reaching over-current and tripping. Since the pre-trip F-N plot does not show a definitive linear trend, it is difficult to say that the electron emission from the surface is from field emission. As such, a field enhancement factor could not be determined. The F-N plot of the post-trip runs shows more consistency with F-N field emission. Although in the J-E plot on the right side of figure does not clearly show the increase in current density for run 9 and 11, the F-N plot of these two runs, even with the limited number of data points, shows a linear trend. The F-N plot for run 10 is the most linear of all the plots for K3 over all test setups. From the slope of the linear best fit of the F-N plots,  $\beta$  was found to be 1161 for run 9, 1001 for run 10, and 2046 for run 11.

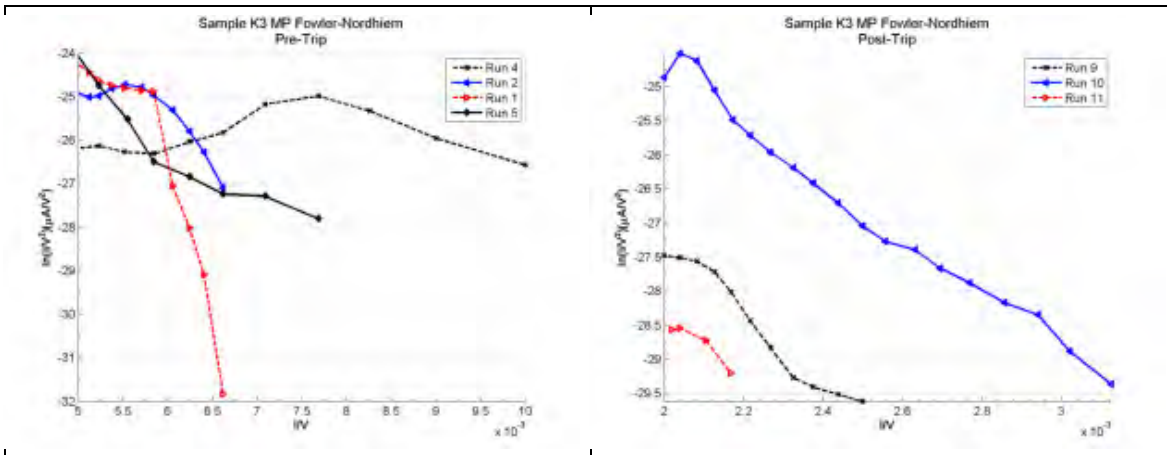


**Figure 102 – Field emission testing Fowler-Nordheim plots for sample K3, MP setup (left) 1, 2, 4, and 5 (right) runs 9-11**

#### 4.4.3. Sample Set L – Field Emission

Sample set L, containing two samples L1 and L2, was subjected to 19 different runs using the three different test setups. This sample set is presented by sample and apparatus below.

##### 4.4.3.1. Sample L1 – Field Emission

Sample L1 was tested for field emission using both the AA and the MP test setups. The testing using the AA setup was the first accomplished for this entire work. The parameters of this test are outlined in Table 15, which shows that with exception of the first and last runs, all other runs tripped due to arcing or over-current in the system.

**Table 15 – Sample L1 AA Setup Run Parameters**

Sample	Apparatus	Run	Start Voltage	Stop Voltage	Step	Dwell	Trip/Off/Hold
L1	AA	1	200	1000	25	4	
		2	500	2000	25	4	Trip/1025
		3	500	2000	25	4	Trip/1750
		4	500	2000	25	2	Off/1800
		5	600	2000	25	2	Trip/1675
		6	600	1600	25	2	Trip/1550
		7	500	1500	10	2	

Since the emission area is unknown while using the AA setup, the IV curves are shown rather than the J-E curves in Figure 103. An observation of the runs shows that run-to-run they nearly parallel, which shows that the field emission is consistent from run-to-run. The curves also mimic other curve produced using the AA setup. The turn-on voltages can only be estimated to be between 800-900 V (3.75-4.25 V/ $\mu\text{m}$ ). These turn-on voltages are the most consistent values compared to other CNT growth methods.

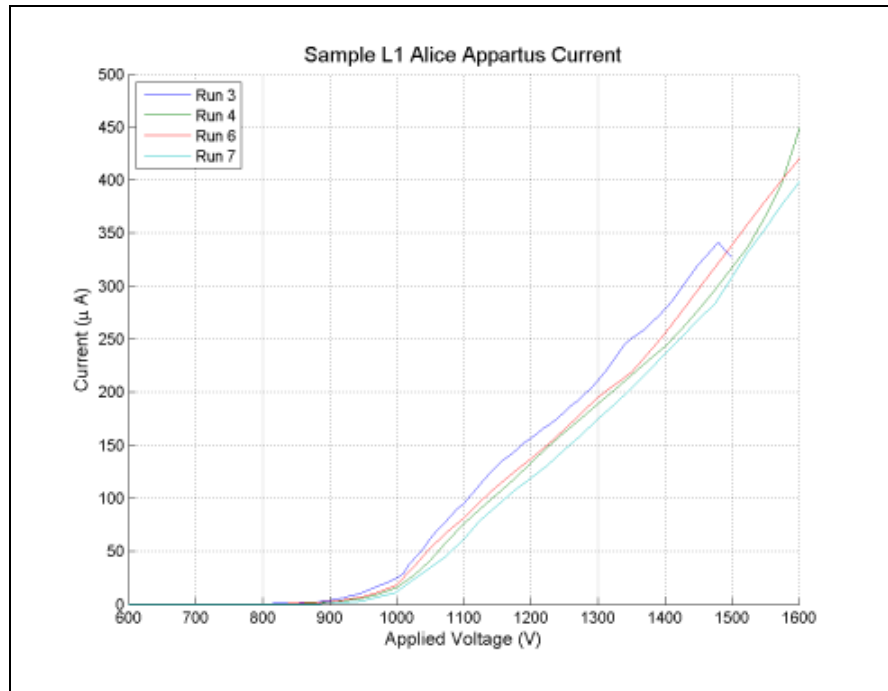


**Figure 103 – Field emission testing current (IV) curves for sample L1, AA setup runs 3, 4, 6, and 7**

The F-N plot for this sample, shown in Figure 104, is also consistent from run-to-run and has a shape similar to that describe by Fursey *et al*, where the field emission become non-linear at higher voltages [38]. Since the F-N plot was made independent of the current density,  $\beta$  can still be determined from the slope of the low voltage region. For runs 3, 4, 6, and 7,  $\beta$  is calculated as 14085, 3673, 4676, and 5050. With the

exception of run 3, the field enhancement factor increases with subsequent runs. This is consistent with runs from other samples.

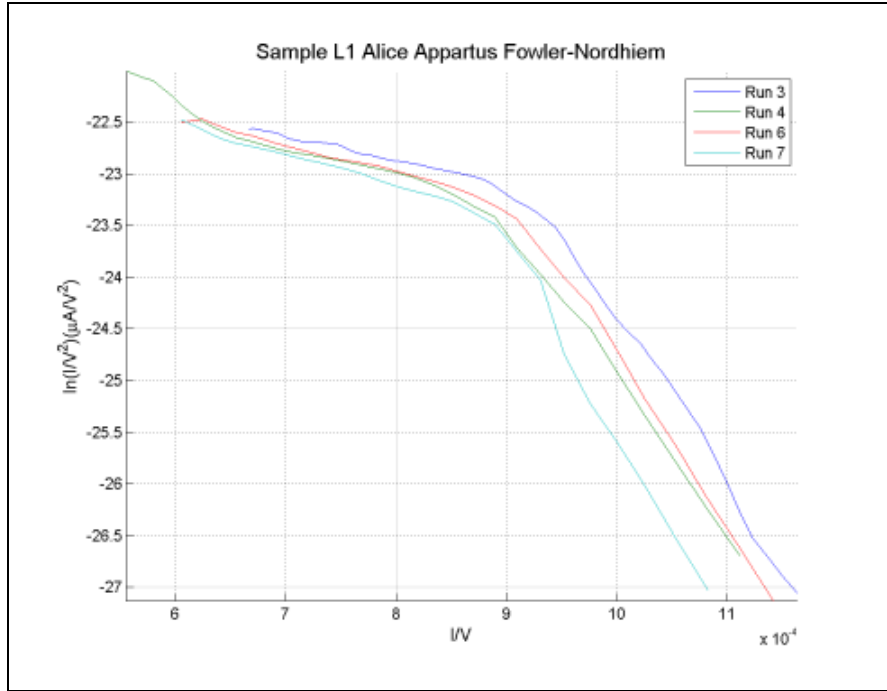


**Figure 104 – Field emission testing Fowler-Nordheim plots for sample L1, AA setup runs 3, 4, 6, and 7**

Sample L1 was also tested using the MP setup. The parameters used during these field emission runs are outlined in Table 16. Runs 1-3 and 5 were used in the analysis to determine the turn-on field and the field enhancement factor.

**Table 16 – Sample L1 MP Setup Parameters**

Sample	Apparatus	Run	Start Voltage	Stop Voltage	Step	Dwell	Trip/Off/Hold
L1	MP	1	100	900	10	2	Trip/790
		2	100	600	10	2	
		3	100	700	10	2	
		4	100	600	10	2	
		5	100	600	10	2	
		6	100	550	10	2	

The J-E curves for sample L1 are found in Figure 105. The plot shows that during runs 1 and 2 L1 turn on strongly with a rapid increase in current. While L1 turns on during run 3 and then turns off and only reaches  $E_{TO}$  at the maximum applied field. The inset in Figure 105 is useful in seeing  $E_{TO}$  for the runs since the large current densities achieved during runs 1 and 2 skew the scaling. The  $E_{TO}$  for sample L1 runs 1-3 and 5 were measured at 4.75, 4.3, 3.51, and 6.01 V/ $\mu\text{m}$ . These values are consistent with the estimated value found using the AA setup.

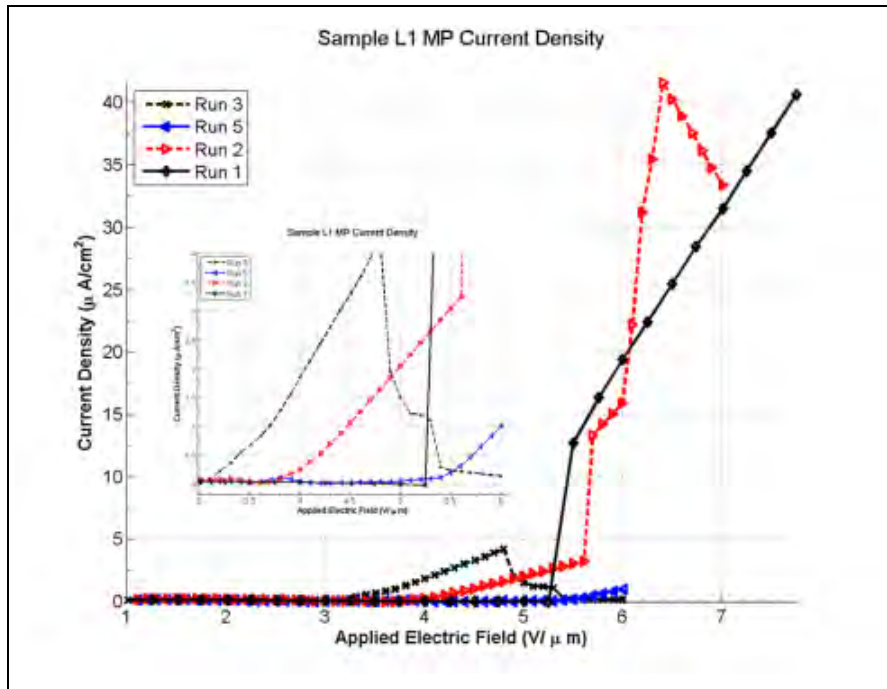


**Figure 105 – Field emission testing current density (J-E) curves for sample L1, MP setup runs 1, 2, 3, and 5**

The corresponding F-N plots in Figure 106 for runs 1-3 and 5 of sample L1 using the MP setup have about the same qualitative aspect as the J-E curves. The plots are not very clean, and provide only a glimpse of the linearity correlation to determine whether or not the sample is emitting in according to F-N theory. The plot shows data for all three data runs, however, since run 5 achieved  $E_{TO}$  at the maximum applied voltage it is

shows only one point. Using a linear fit to the data between  $E_{TO}$  and the first major bend in the J-E plot, the calculated  $\beta$  for sample L1 was 3133 for run 1, 2593 for run 2, 1838 for run 3, and 3128 for run 5. These follow closely to the values calculated early using the AA setup, which indicates that even with noisy data sample L1 maintains consistent field emission.

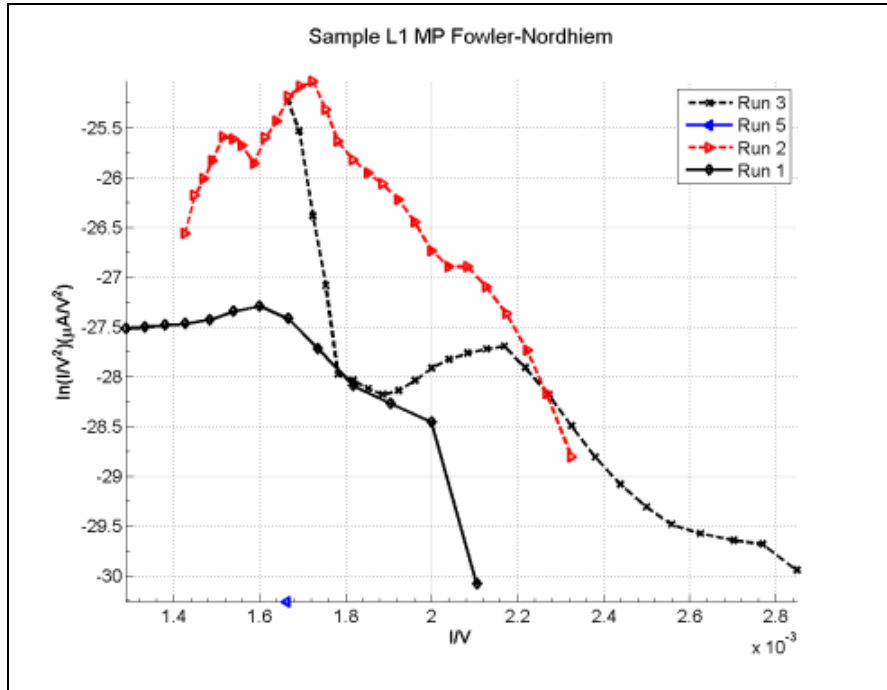


**Figure 106 – Field emission testing Fowler-Nordheim plots for sample L1, MP setup runs 1, 2, 3, and 5**

#### 4.4.3.2. Sample L2 – Field Emission

Sample L2 was tested over 6 runs using both the AT setup and the MP setup. This was the least amount of runs conducted for any sample. L2 was tested 4 times using the AT setup with the parameters in Table 17. Of those 4 runs, only runs 1-3 produced data useful for analysis as L2 did not reach the turn-on threshold during run 4.

**Table 17 – Sample L2 AT Setup Run Parameters**

Sample	Apparatus	Run	Start Voltage	Stop Voltage	Step	Dwell	Trip/Off/Hold
L2	AT	1	500	1500	25	4	Trip/1375
		2	700	1200	10	2	
		3	500	1300	10	2	Trip/1170
		4	200	1200	10	2	Trip/980

The J-E curves in Figure 107 show L2 response to an applied field. A visual observation of the curves reveals that the sample performs better as additional runs. This observation is consistent with other samples which show decreasing turn-on fields as more run are completed. The culprit for this behavior can be contributed to the emitter's surface being condition and interfering impurities being removed by the electrons as they move through the emitters. The  $E_{TO}$  for runs 1-3 were measured at 11, 9.9, and 5.7 V/ $\mu\text{m}$ .

The F-N plots for sample L2 in Figure 108 are nearly linear, which is indicative of field emission according to F-N theory. From the linear fit of the plots,  $\beta$  can be calculated as 800, 3505, and 3830. The surface condition effect is shown again here by the increase in  $\beta$ .

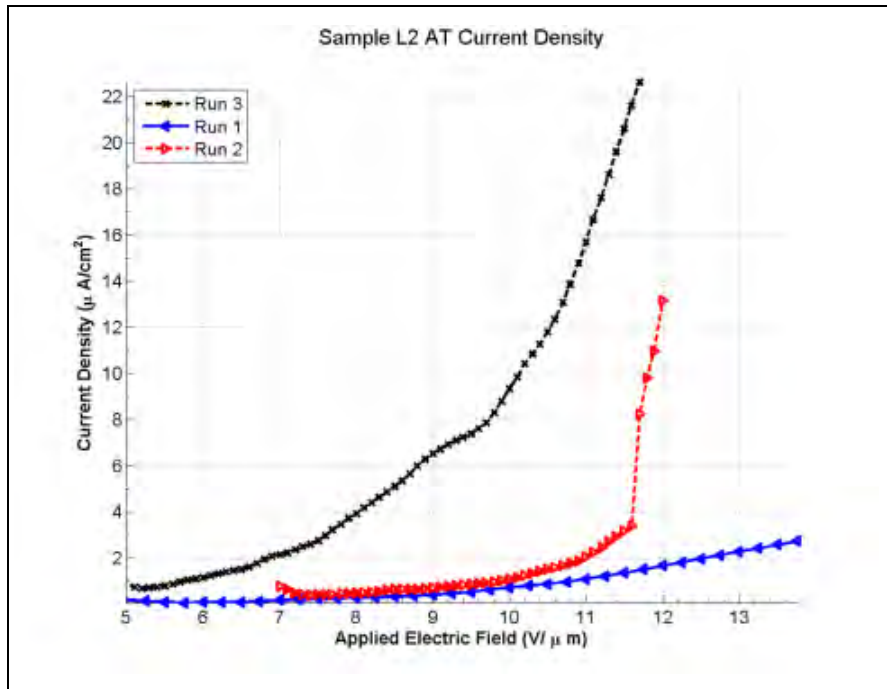


Figure 107 – Field emission testing current density (J-E) curves for sample L2, AT setup runs 1-3

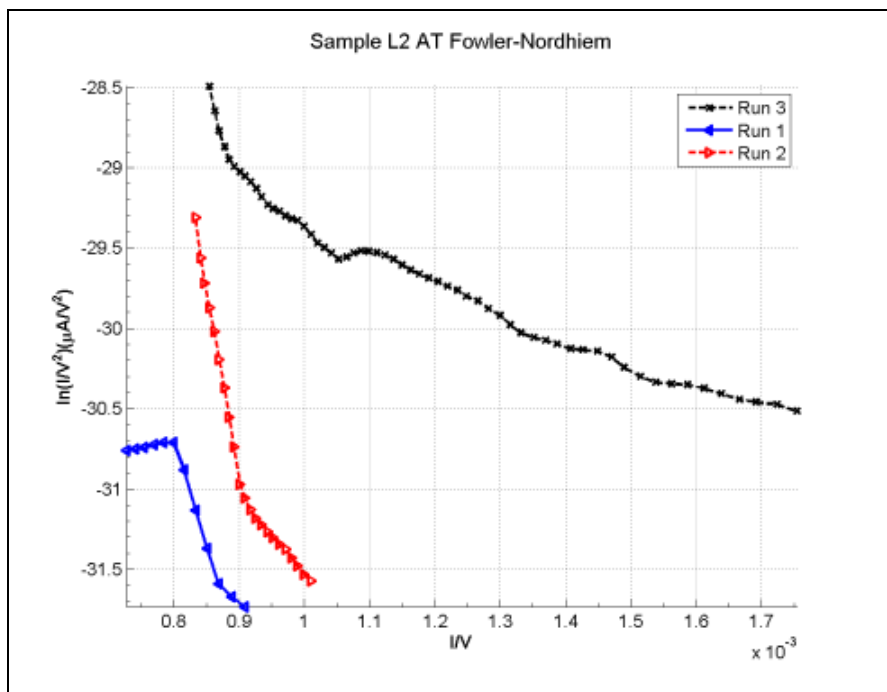


Figure 108 – Field emission testing Fowler-Nordheim plots for sample L2, AT setup runs 1-3

Sample L2 was also test with 2 runs using the MP setup. The parameters used for this setup are found in Table 18.

**Table 18 – Sample L2 MP Setup Parameters**

Sample	Apparatus	Run	Start Voltage	Stop Voltage	Step	Dwell	Trip/Off/Hold
L2	MP	1	50	900	25	2	Trip/450
		2	50	500	10	2	Trip/440

Because the runs performed drastically different, their J-E curves have been plotted separately. The curves are shown in Figure 109. The plots show that for run 1 the sample emits until 2.5 V/μm decrease then increases until 3.25 V/μm before decreasing finally until it trips at 4.5 V/um. Run 2, shown without filter, turns on at 1.75 V/μm, then increased until 3 V/μm where the current increase rapidly until the emission current ceased to be stable eventually tripping the power supply. No further runs were completed because of continued operation of the sample in this manner.

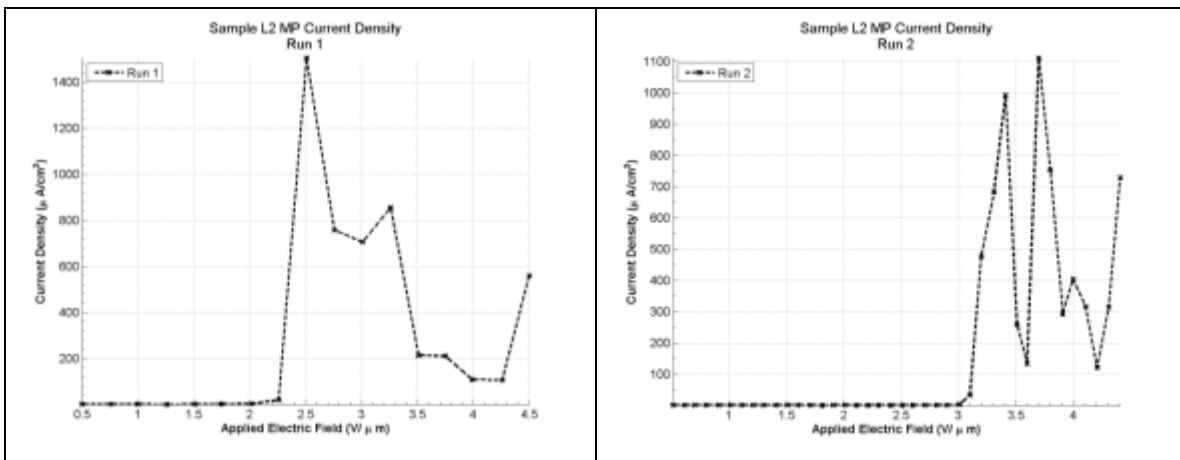


**Figure 109 – Field emission testing current density (J-E) curves for sample L1, MP setup (left) runs 1-2 with filter, (right) runs 1-2 using raw data**

The F-N plots of the two plots, in Figure 110, are plotted below using both a curve-fitting filter on the left and the raw data on the right. The field enhancement factor extracted

from a linear best fit of smoothed curves was calculated at 4195 for run 1 and 7089 for run 2. These value inconsistently high for this sample which has a  $\beta$  valued 1.5 to 2 times lower using the AT apparatus.

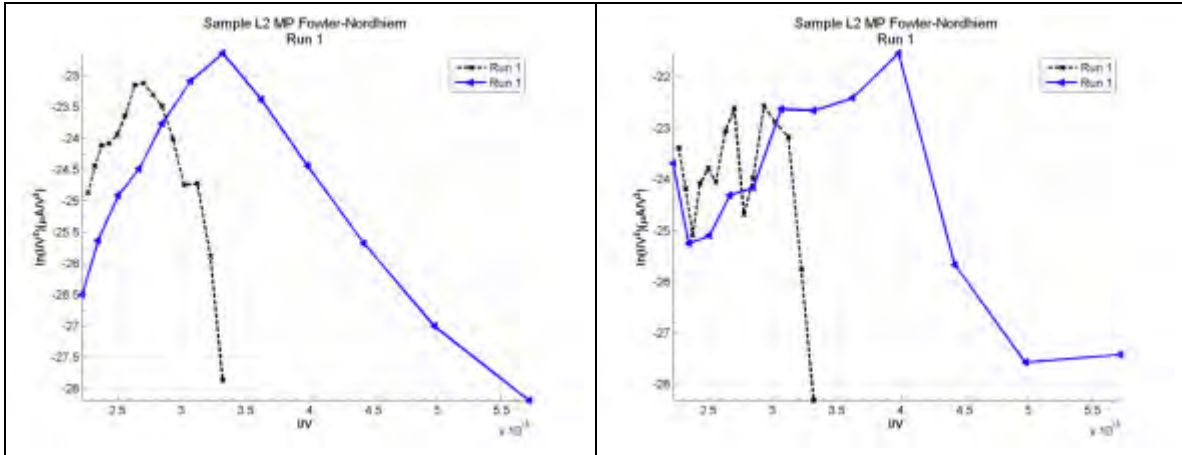


**Figure 110 – Field emission testing Fowler-Nordheim plots for sample L1, MP setup runs (left) runs 1-2 with filter, (right) runs 1-2 using raw data**

#### 4.4.4. Sample Set H – Field Emission

Sample set H, containing four samples labeled H1-H4, was subjected to 72 different runs using the MP test configuration.

##### 4.4.4.1. Sample H1: All RIE Surface – Field Emission

Sample H1, which an entire etched surface, was tested using only the MP setup over the course of 16 runs. The run parameters for sample H1 are given in. Runs 1-5 were conditioning runs during no emission was present, or the sample turned on and quickly tripped the power supply. In an attempt to obtain a higher stopping voltage, the high voltage power supply was swapped for a power supply with a lower voltage limit but higher current limit. Runs 9-12 used this power supply, but produced limited quality data. Run 16 contained current spikes and had a positive slope on the linear curve fit to

its F-N plot. After eliminating the above runs, analysis can be completed on runs 6-8 and 15.

**Table 19 – Sample H1 MP Setup Run Parameters**

Sample	Apparatus	Run	Start Voltage	Stop Voltage	Step	Dwell	Trip/Off/Hold
H1	MP	1	100	600	25	10	
		2	500	1000	25	10	
		3	500	1500	25	2	Trip/1475
		4	500	1500	25	2	Trip/1075
		5	500	1000	25	2	Trip/925
		6	300	800	25	2	
		7	300	800	25	2	
		8	300	800	10	2	Trip/750
		9	300	800	10	2	Trip/680
		10	300	800	10	2	Trip/680
		11	100	500	10	2	
		12	100	500	10	2	Trip/725
		13	600	1000	25	2	Trip/850
		14	300	600	10	2	
		15	450	700	10	2	Off/560
		16	450	750	10	2	Off/460

The J-E curves for runs 6-8 and 15 are shown in Figure 111. The inset of Figure 111 shows in more detail the turn-on regime for run 6-8. The curves show that the sample turns-on and has an increase in current density as the electric field is increased. Without run 15 being stopped it would have tripped the power supply. Using the  $1 \mu\text{A}/\text{cm}^2$  criteria for  $E_{\text{TO}}$ , the measured  $E_{\text{TO}}$  for runs 6-8 and 15 is 7.25, 6.60, 6.20, and 5.50 V/ $\mu\text{m}$ . The trend of decreasing  $E_{\text{TO}}$  is consistent with previous sample set. The maximum current density for the analyzed runs, extracted from the raw data, was 31.9  $\mu\text{A}/\text{cm}^2$  for run 6, 167.5  $\mu\text{A}/\text{cm}^2$  for run 7, 128.0  $\mu\text{A}/\text{cm}^2$  for run 8, and 358.1  $\mu\text{A}/\text{cm}^2$  for run 11.

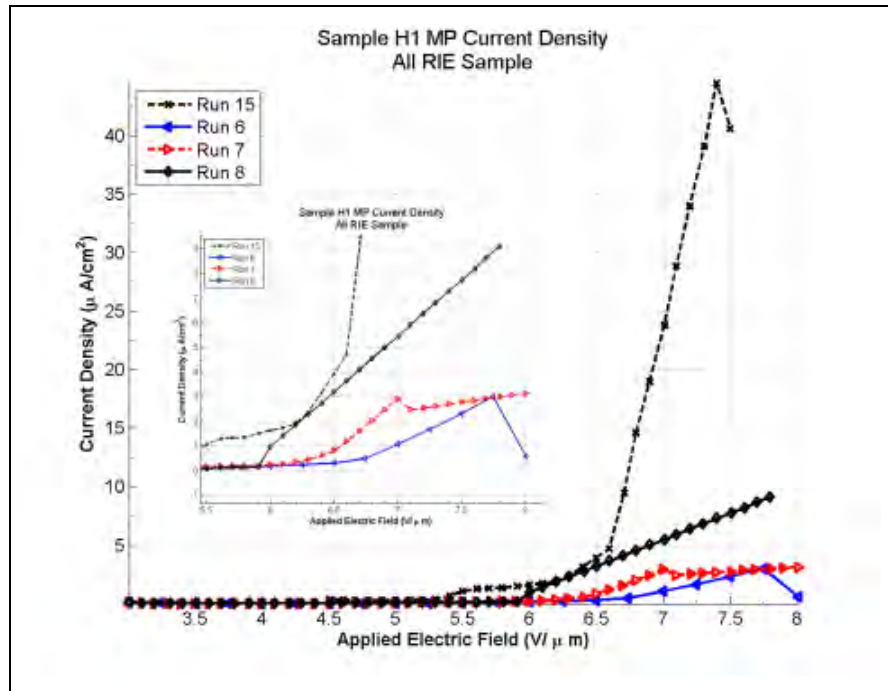


**Figure 111 – Field emission testing current density (J-E) curves for sample H1, MP setup runs 6-8 and 15**

To determine if the current from the sample was from field emission, the F-N plots were analyzed for linearity. With the exception of run 7, all the runs shown in Figure 112 show a linear trend at least over the lower voltage regions of the plot. Using a linear fit,  $\beta$  for the runs was calculated at 735 for run 6, 585 for run 8, and 1190 for run 15.

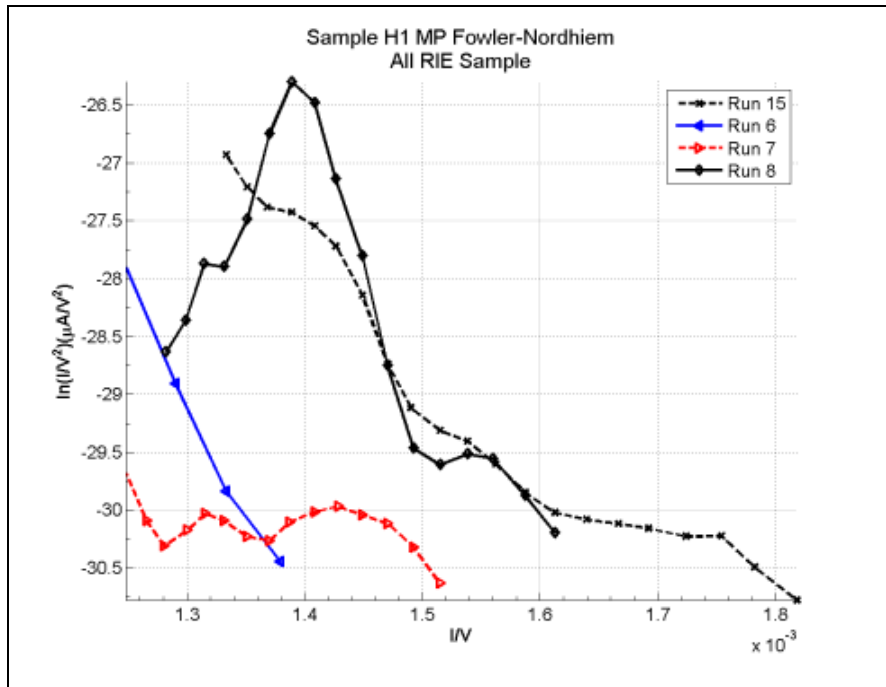


**Figure 112 – Field emission testing Fowler-Nordheim plots for sample H1, MP setup runs 6-8 and 15**

#### 4.4.4.2. Sample H2: Patterned Surface – Field Emission

Sample H2, which has 6 μm pillars, was tested using only the MP setup over the course of 22 runs. The test parameters for each run are given in Table 21. The emitter area was conditioned during runs 1-6, run 12 contained unstable current measurements, run 14 included a hold a 525 V, and the emission stability started to degrade over runs 17-21. The remaining runs, 7-11, 13, 15, and 16, are then used to perform field emission analysis of the sample. The quality of the collected data was enhanced by turning off the data collection before the setup had a chance to arc and trip the power supplies.

**Table 20 – Sample H2 MP Setup Run Parameters**

Sample	Apparatus	Run	Start Voltage	Stop Voltage	Step	Dwell	Trip/Off/Hold
H2	MP	1	100	600	25	2	Off/525
		2	100	450	10	2	
		3	200	700	25	2	
		4	500	1000	25	2	Trip/875
		5	600	900	25	2	
		6	600	900	25	2	Trip/875
		7	400	800	10	2	
		8	400	600	10	2	Off/600
		9	400	600	10	2	Off/580
		9.1	400	600	10	2	Off/590
		10	400	600	10	2	Off/600
		11	300	600	5	2	
		12	300	800	10	2	
		13	300	550	5	2	
		14	300	550	15	2	Hold/525
		15	300	550	15	2	Off/530
		16	300	550	15	2	Off/520
		17	250	650	15	2	Off/630
		18	500	800	10	2	Off/790
		19	750	1000	10	2	Trip/930
		20	300	550	10	2	Off/490
		21	300	900	10	2	Trip/880

The J-E curves, shown in Figure 113, are from runs starting near the beginning of the test cycle all the way to the end of the test cycle. The curves show the variability of the samples emitting surface as it is repeatedly put under an applied field. Two runs to note are runs 15 and 16. Both of these runs occurred after the sample was held at 5.25 V/ $\mu\text{m}$  for nearly 15 hours. The inset of figure () shows a refined view of the curves near the turn-on voltages. The measured  $E_{\text{TO}}$  for runs 8-9.1, 11, 15, 16, and 18 are 4.60, 4.00, 4.40, 5.50, 3.50, 3.61, and 5.20 V/ $\mu\text{m}$ . The general trend for  $E_{\text{TO}}$  decreased as a set of runs is completed. For example runs 8-9.1. The best achieved  $E_{\text{TO}}$  for these runs was

achieved after the hold run. The maximum measured raw current density for the plotted runs is 159.4, 44.11, 71.6  $\mu\text{A}/\text{cm}^2$  for runs 8-9.1; 23.0  $\mu\text{A}/\text{cm}^2$  for run 11; 149.2 and 216.5  $\mu\text{A}/\text{cm}^2$  for runs 15 and 16; and 735.6  $\mu\text{A}/\text{cm}^2$  for run 18.

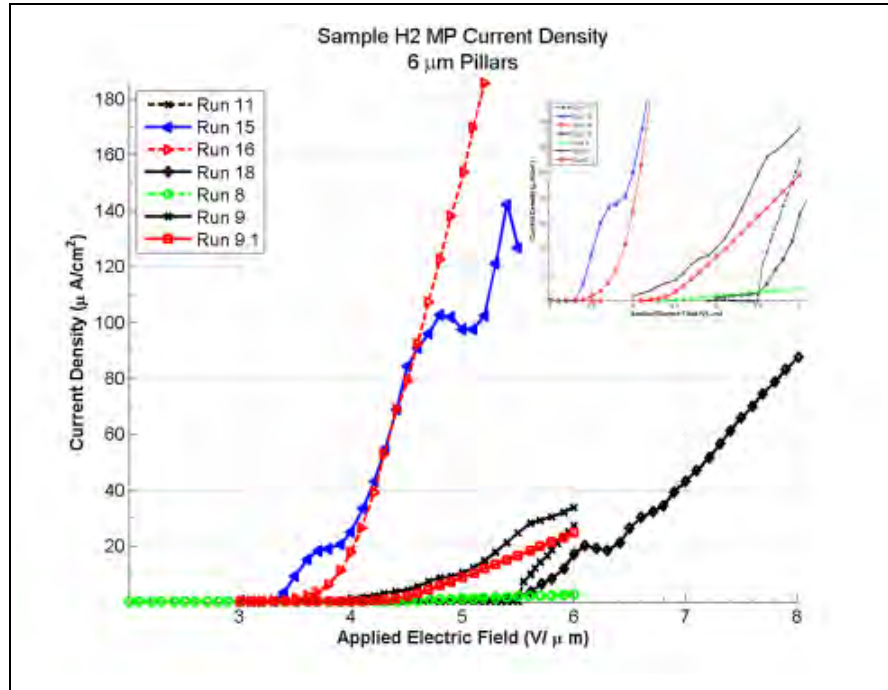


**Figure 113 – Field emission testing current density (J-E) curves for sample H2, MP setup runs 8-9.1, 11, 15, 16, and 18**

The F-N plots for H2 are found in Figure 114. A qualitative look at the curves reveals that they are linear in nature. From that correlation, it can be deduced the sample emits according to F-N theory. Using a linear fit the curves,  $\beta$  can be calculated for as 721, 1987 and 1009 for runs 8-9.1; 4883 for run 11; 4137 and 1434 for runs 15 and 16; and 1225 for run 18.

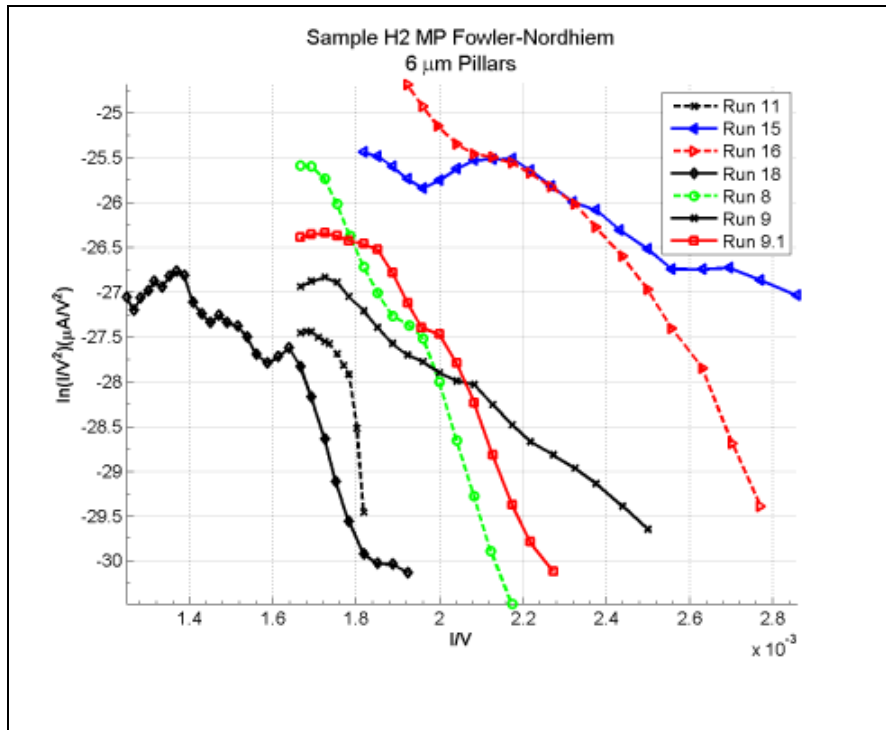


**Figure 114 – Field emission testing Fowler-Nordheim plots for sample H2, MP setup runs 8-9.1, 11, 15, 16, and 18**

#### 4.4.4.3. Sample H3: Patterned Surface – Field Emission

Sample H3, which is patterned with 6  $\mu\text{m}$  pillars, was tested over 14 runs using the parameters in Table 21. The first 5 runs were used to find an operating region for the sample. After which the remaining runs were conducted in such a way as to not trip the power supply with an over-current or breakdown between the anode and the sample. Run 11 was held at 8.3  $\text{V}/\mu\text{m}$ , but tripped after 3 minutes. Runs with frequent spikes in current are also omitted from the emission analysis. These runs include runs 10 and 13.

**Table 21 – Sample H3 MP Setup Run Parameters**

Sample	Apparatus	Run	Start Voltage	Stop Voltage	Step	Dwell	Trip/Off/Hold
H3	MP	1	100	500	25	2	
		2	400	800	25	2	
		3	600	1000	25	2	Trip/975
		4	600	900	25	2	Trip/900
		5	400	900	25	2	
		6	400	800	25	2	Off/750
		7	400	850	10	2	
		8	400	800	10	2	Off/800
		9	300	800	10	2	Off/800
		10	300	850	10	2	
		11	300	900	10	2	Hold/860
		12	300	850	10	2	Off/840
		13	400	850	10	2	Trip/860
		14	300	900	10	2	Trip/840
		15	300	900	10	2	Off/900

The J-E curves for H3 are shown in Figure 115. The inset to the figure show a comparison between the early runs and later runs near their respective turn-on field. The early runs, 6-9, produced far lower current densities at the same applied fields. The applied field to obtain the turn-on current of  $1 \mu\text{A}/\text{cm}^2$  for runs 6-9 is measured at 6.5, 7.0, 6.2, 6.3  $\text{V}/\mu\text{m}$ . For this span of runs,  $E_{TO}$  was more constant than trending up or down. The difference between the highest and lowest  $E_{TO}$  is just over 10%. The maximum currents for these runs are 6.3, 60.3, 14.3, and 17.3  $\mu\text{A}/\text{cm}^2$ . For the later runs,  $E_{TO}$  measured at 5.4, 5.2, 4.9  $\text{V}/\mu\text{m}$  respectively for runs 12, 14, and 15, with  $J_{MAX}$  of 272.3, 393, and 465.5  $\mu\text{A}/\text{cm}^2$ . The current density for the later runs is upwards of 20 times greater than the earlier runs.

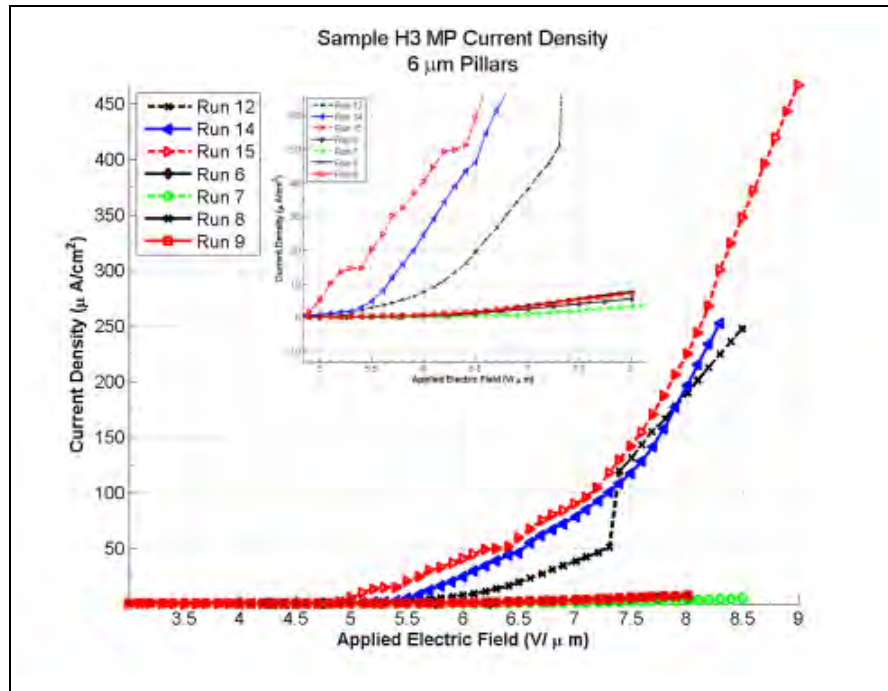


**Figure 115 – Field emission testing current density (J-E) curves for sample H3, MP setup runs 6-8, 12, 14, and 15**

The F-N plot in Figure 116 mirrors the trends found in the J-E curves. The later runs outperform the earlier runs. All the runs, however, show the linear trend which is indicative of F-N field emission. As such,  $\beta$  can be deduced from a linear fit of the data. For the early runs, 6-9,  $\beta$  is calculated to be 1305, 481, 1176, and 1008. With the exception of run 7,  $\beta$  for these runs is within 10% from run-to-run. Runs 12, 14, and 15 have a  $\beta$  of 1162, 1849, and 1346. The overall average of the later runs is greater than the earlier runs. The increased current density, lower turn-on field, and greater field enhancement show that the emission from the later runs is coming from a more and more conditioned emitting surface much like the other samples. This sample also shows how controlling the runs in a specific operating region can enhance the run-to-run consistency.

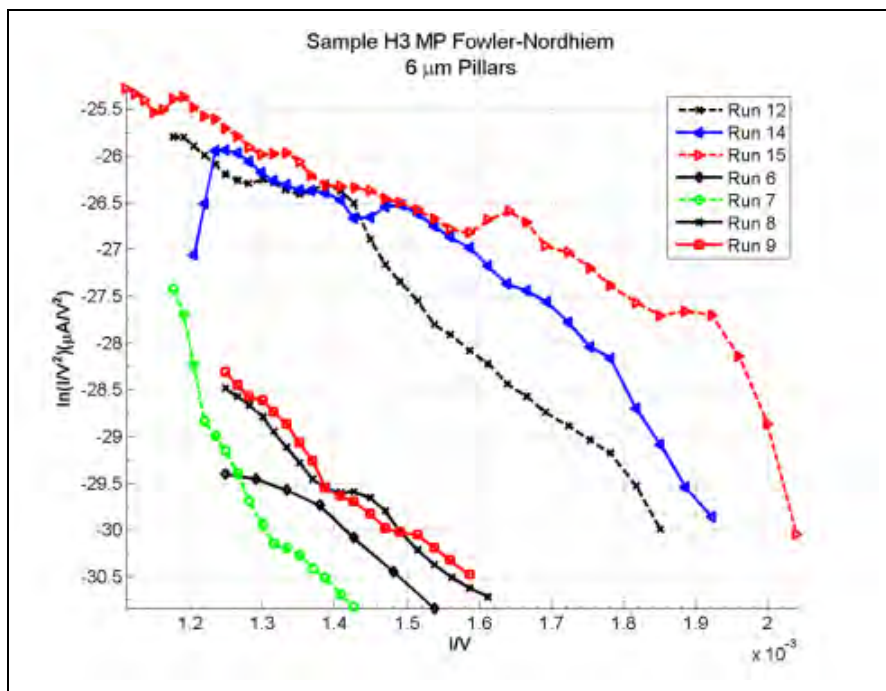


**Figure 116 – Field emission testing Fowler-Nordheim plots for sample H3, MP setup runs 6-8, 12, 14, and 15**

#### **4.4.4.4. Sample H4: Unpatterned Surface – Field Emission**

Sample H4, with a planar CNT surface, was tested over 19 runs using the MP setup. The test parameters are listed in Table 22. Although there are many run the first 10 were required to condition and find a stable range without the current becoming unstable or the power supply tripping due to an over-current. Stable currents were obtained in runs 11-13, but after run 13, the current become unstable at voltages above 650 for runs 14 and 15. The test parameters were adjusted again to find another stable regime, and the test was completed with runs 16-19.

**Table 22 – Sample H4 MP Setup Run Parameters**

Sample	Apparatus	Run	Start Voltage	Stop Voltage	Step	Dwell	Trip/Off/Hold
H4	MP	1	500	1000	25	2	Trip/840
		2	500	1000	25	2	
		3	500	1000	25	2	
		4	500	1000	25	2	Off/800
		5	500	1000	25	2	Trip/975
		6	500	800	25	4	
		7	400	800	25	2	
		8	400	800	25	2	
		9	500	900	10	2	
		10	500	900	10	2	
		11	600	900	10	2	Off/860
		12	600	9000	10	2	Off/890
		13	600	900	10	2	Off/900
		14	600	1000	10	2	Off/900
		15	300	700	10	2	Off/660
		16	200	650	10	2	Off/630
		17	200	650	10	2	
		18	200	650	10	2	
		19	200	650	10	2	

Because of the change in test parameter between runs 11-13 and runs 16-19, the J-E curves could not be plotted on the same axis together for a direct comparison. They are, however, plotted side by side in Figure 117. The left side of Figure 117 shows the plots from runs 11-13, while the right side shows runs 16-19. From the plots, it is easy to see that the performance of the sample improved during runs 14 and 15. The current instability and voltage breakdown which occurred during those runs most likely altered the surface of the sample, by removing impurities or destroying the dominant CNTs, and allowing others to become the dominant emission source. The first set, runs 11-13, had turn-on fields of 8.2, 8.2, and 7.6 V/ $\mu\text{m}$ . The second set, runs 16-19, had  $E_{\text{TO}}$  of 5, 3.8, 3.8, and 3.61 V/ $\mu\text{m}$ , which is approximately a 50% reduction on average. A comparison

of the J-E curve also shows that the measure current density of the later runs is nearly 10-20 times greater than the current density measure earlier.

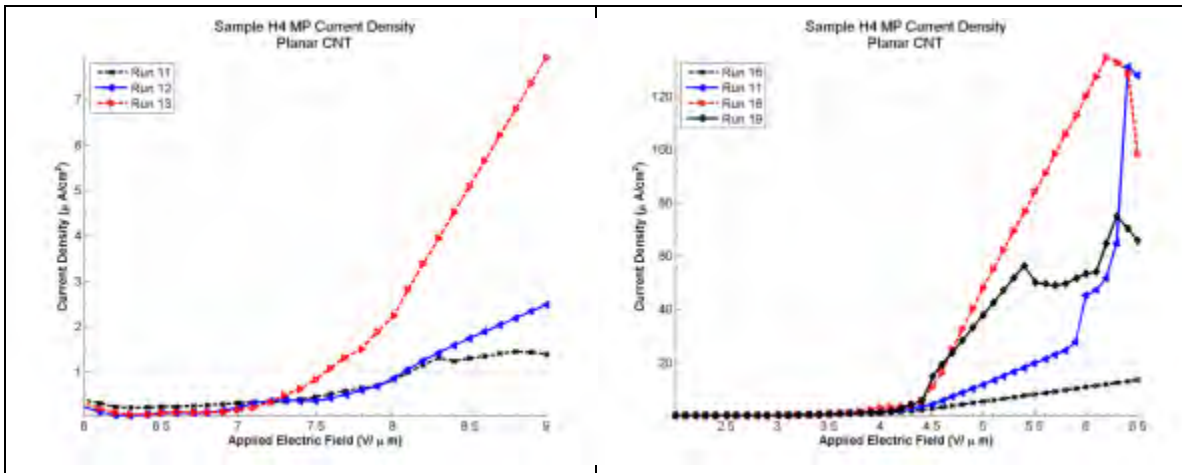


**Figure 117 – Field emission testing current density (J-E) curves for sample H4, MP setup runs (left) 11-13, (right) 16-19**

The F-N plots for H4 are presented the same manner as the J-E curves. In Figure 118, the F-N plots for runs 11-13 are shown on the left, while the F-N plots for runs 16-19 are shown on the right. Both sets of runs have near linear curves, or at a minimum a region in which the curve appears linear, so it can be assumed that the field emission follows F-N theory. The plots for runs 11-13 have similar feature with a peak separating regions of high and low voltages. Using the low voltage regions,  $\beta$  can be extracted from a linear curve fit. For runs 11-13,  $\beta$  is found to be 2793, 407, 613. Of those values run 11 appears to be outlier caused by errant spikes in the original data. The later runs, 16-19, have consistent nearly identical curve shapes. For runs 16-19,  $\beta$  is 1148, 1394, 1771, and 1744. The values for  $\beta$  for these run are 2-3 times the values for the earlier runs. They also have a generally upward trend, resulting from the emitter surface improving with each run.

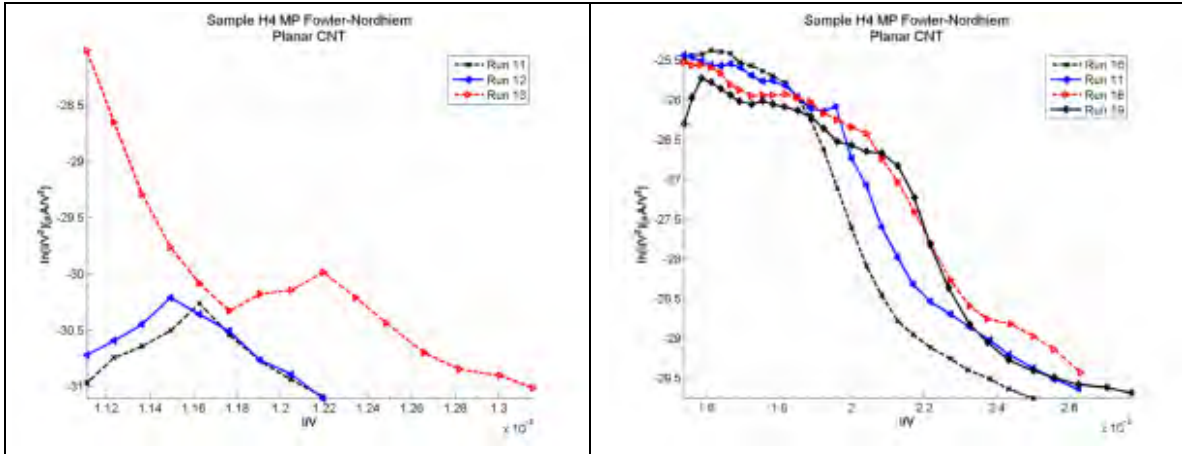


**Figure 118 – Field emission testing Fowler-Nordheim plots for sample H4, MP setup runs (left) 11-13, (right) 16-19**

#### 4.4.5. Field Emission Results Comparison

##### 4.4.5.1. Sample Sets J through L

To compare the results between different sets, the results for the turn-on voltage and field enhancement factors were tabulated and the minimums and maximums were extracted. The turn-on field and field enhancement factors were then analyzed to find whether or not they trend up or down. In some cases, it was determined that  $E_{TO}$  or  $\beta$  would fluctuate between runs. For these cases the trend was marked as undetermined. The final tabulated results are found in Table 23 below. The common trends for the field emission test are a decrease in  $E_{TO}$  and an increase in  $\beta$ . Skipping the AA runs since they have an unknown area,  $E_{TO}$  decreased in 60% of the samples. Over all 12 of the samples/run combinations,  $\beta$  increased 66% of the time. The values for  $E_{TO}$  for all samples are generally higher than reported values from Bonard *et al* . However, the calculated  $\beta$  values are comparable with reported values.

**Table 23 – Sample to Sample Comparison of Performance Factors**

Sample	Run	Min E <sub>TO</sub>	Max E <sub>TO</sub>	Trend E <sub>TO</sub>	Min b	Maximum □	Trend □	Note
J1	MP	6.2	6.6	Dec	714	975	Inc	
J1	AT	8.01	6.5	Dec	635	1039	Inc	
J2	AA	n/a	n/a	n/a	792	2384	Inc	Unknown Area
J2	AT	8.01	6.3	Dec	593	1305	Inc	
J2	MP	2.5	7.5	Dec	2423	8007	Inc	
K1	AA	n/a	n/a	n/a	1523	4143	Inc	Unknown Area
K1	MP	2.9	3.7	Inc	1160	3790	Und	
K2	AT	10	14	n/a	n/a	n/a	n/a	Did not exhibit FE
K3	MP	3.2	4.6	Dec	1162	2046	Inc	Post-trip data
L1	AA	n/a	n/a	n/a	3673	5040	Inc	Unknown Area
L1	MP	3.51	6.01	Dec	1838	3129	Dec	
L2	AT	5.7	9.2	Und	800	3831	Und	
L2	MP	1.75	3.01	Und	4196	7090	Und	2 Runs only

#### 4.4.5.2. Sample Set H Comparisons

Sample set H brings a unique opportunity to compare differently prepared sample that were processed using the same SiC wafer. To compare the samples, the best runs were selected from each and plotted against each other in both J-E plots in Figure 119 and F-N plots in Figure 120. The average values for both E<sub>TO</sub> and β are also tabulated in Table 24. Both the plots and the table show the patterned sample H2 as the best sample for field emission with a lower E<sub>TO</sub> and higher β. However, the unpatterned sample H4 performed better than the other patterned sample H3. The expected result would have both patterned sample outperforming the unpatterned sample. Sample H4, which had the all RIE surface, performed the worst. There could be several reasons for one pillared sample performing better than the all CNT surface and one not. One reason is the condition of the emitter surface. The emitter surface of the underperforming pillared sample may have more impurities or amorphous carbon present inside the emission area than the better performing sample. The better performing pillared sample may also have

larger quantity of stronger emission sites than the underperforming site. Although the total measured emission area is  $1.86 \times 10^6 \mu\text{m}^2$  contains the pillared structures and the etched area, the area of the pillars is approximately 9% of the total area with approximately 6000 pillars inside the total emission area. The distance between the pillars also mean that each pillars is independent of the rest. The independency of the site could result in stronger emitter in one part of the sample compare to the remaining sample.

**Table 24 - Sample to Sample Comparison for Sample Set H**

Sample	Configuration	Average $E_{TO}$	Average $\beta$
H1	All RIE	6.39	837
H2	6 um Pillars	4.40	2199
H3	6 um Pillars	5.93	1190
H4	All CNT	5.60	1410

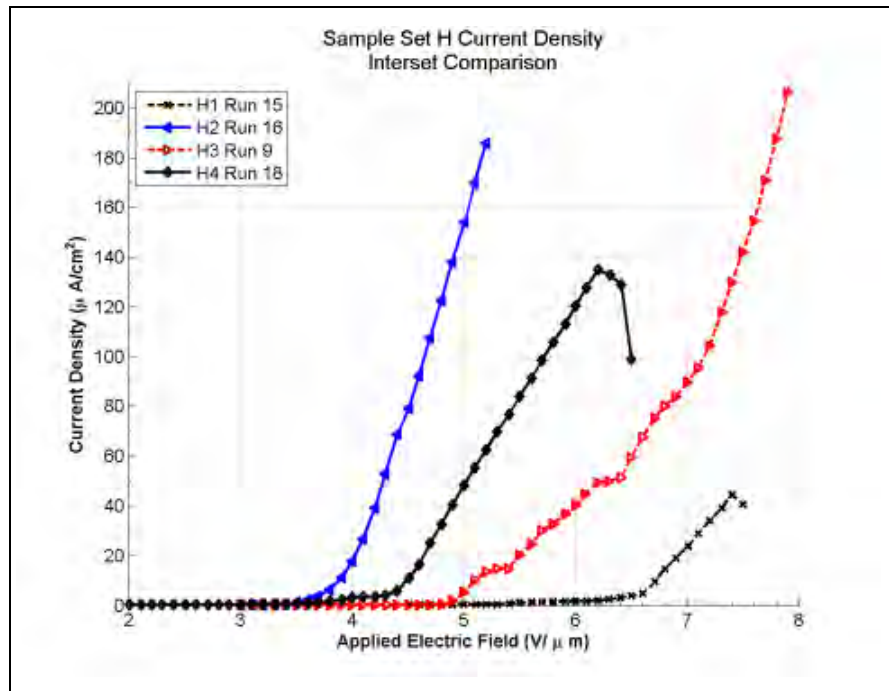


**Figure 119 – Field emission testing current density (J-E) curves comparing sample H1 run 12, sample H2 run 16, sample H3 run 9, and sample H4 run 18**

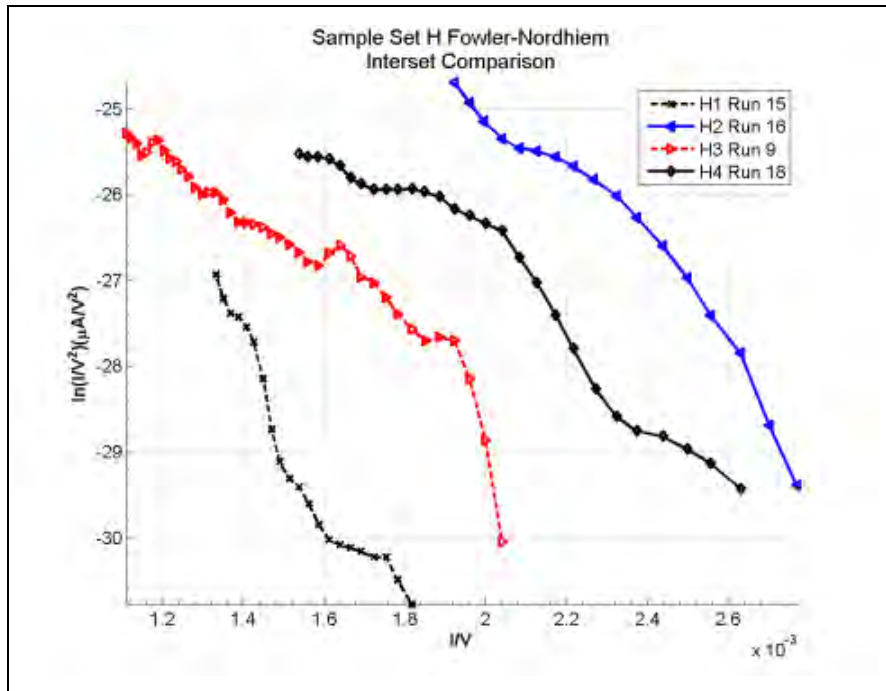


**Figure 120 – Field emission testing Fowler-Nordheim plots comparing sample H1 run 12, sample H2 run 16, sample H3 run 9, and sample H4 run 18**

#### 4.4.6. Field Emission Stability Results

In order to test the field emission stability select samples were subjected to extended runs at given applied fields. The pause time for the selected samples varied which affected the comparison between the samples. Also, because the mean, maximum, minimum and standard deviations are based off the measured currents, the stability between samples cannot be compared directly. To normalize the results, the standard deviation is taken as a percentage of the mean. The results of the stability comparison are shown in Table 25. Plots of the runs showing the linear trend are found in Figure 121, Figure 122, and Figure 123. The stability had a percentage standard deviation in the measured current ranging from 0.17% to 12.3% on samples that continued to emit for the entire period.

**Table 25 – Current Stability Testing Results**

Sample / Run	Mean Current (μA)	Min/Max Current (μA)	Standard Deviation Current (μA)	% of Std Dev to Mean Current	Overall Stability Trend	Notes
<b>J2 / AA Run 5</b>	5.17	3.09 / 6.67	0.5844	11.3	Dec	21+ min run
<b>J2 / AA Run 7</b>	5.51	4.69 / 6.34	0.3389	6.15	Inc	21+ min run
<b>K1 / MP Run 8</b>	1.08	0.0564 / 17	1.475	136	Dec	Current Stepped down after 6 hrs during 15 hr run
<b>H2 / MP Run 14</b>	18.7	12.9 / 31	3.167	0.169	Dec	Average of 6 hrs of 15+ hr run
<b>H3 / MP 11 Run</b>	93.9	70 / 116	11.59	12.3	Dec	Tripped after 1 min 45 seconds

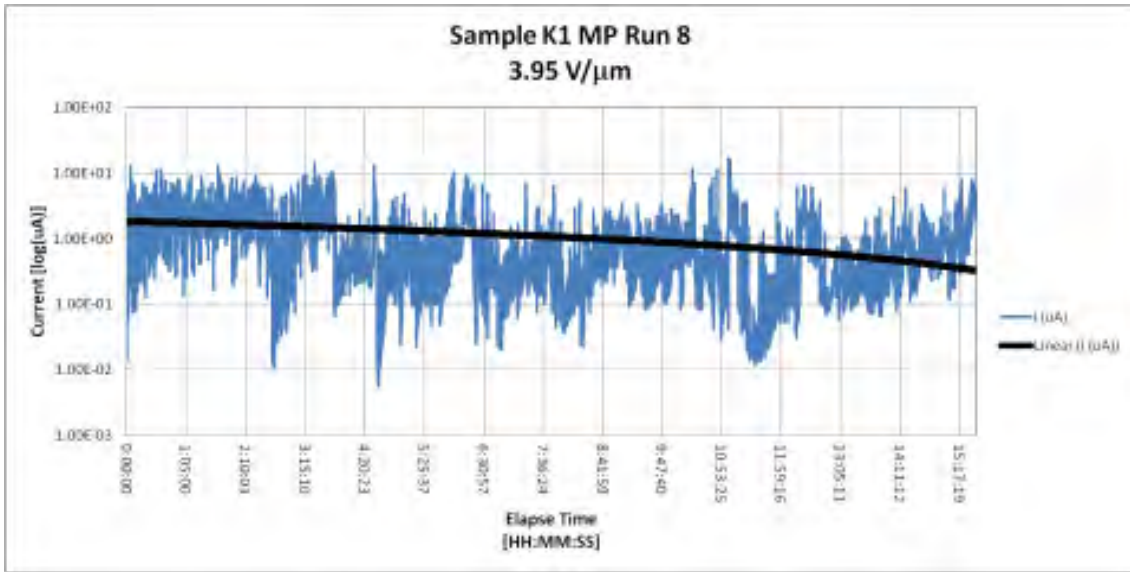


**Figure 121 – Current stability plots for sample K1 MP run 8**

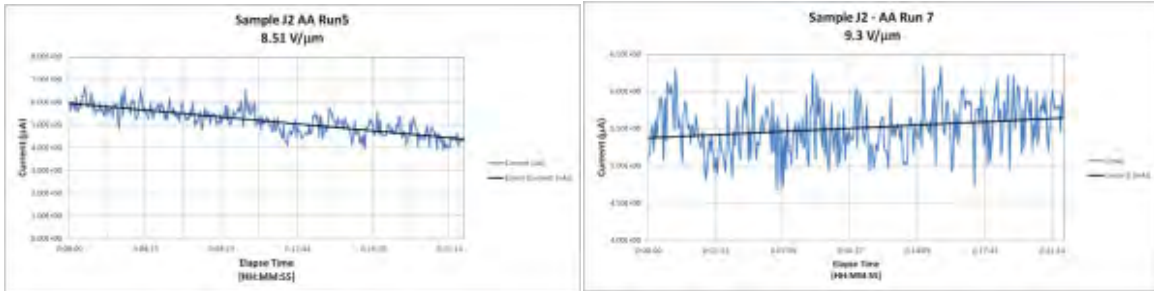


**Figure 122 – Current stability plots for sample J1 AA runs (left) 5 and (right) 7**

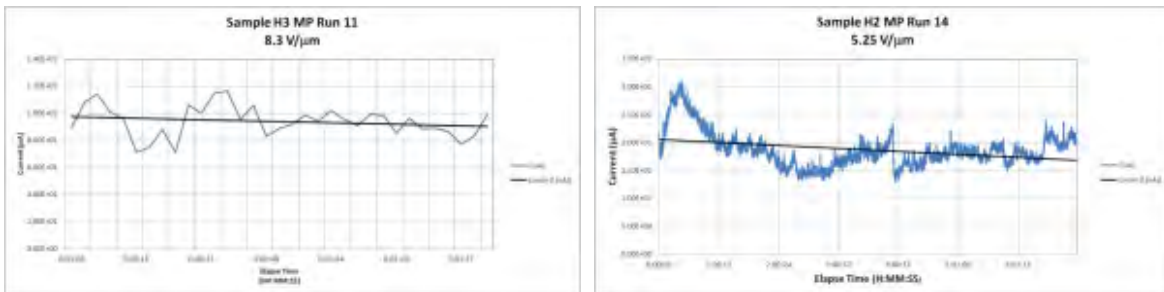


**Figure 123 – Current stability plots for (left) sample H2 MP Run 11 and (right) sample H2 MP Run 14**

#### 4.5. Chapter Summary

Chapter 4 discussed the results found during both the processing of the SiC sample and CNT growth, and the field emission testing. The results of the SiC processing and patterning showed the limits of the nickel etch process as well as the inconsistency with etching using the RIE. The analysis of the CNT growth process found that CNTs grew not only on the top of the pillared structures, but on the sides of the structures and surprisingly on the etched surface. The field emission testing showed that all the samples achieved some degree of field emission. It was found that the samples frequently performed better with each consecutive run. In a direct comparison between samples in the H set, with its varied surface morphologies, the results showed a mixed conclusion with one pillared sample outperforming the unpatterned sample, while the other pillared sample did not. A result caused by surface impurities or the independence

of each pillar inside the total emission area. If the CNT carpet of the all CNT sample was perfectly uniform it would have been subjected to near complete screening because of the density of the CNTs. However since the original SiC surface was not completely uniform the all CNT sample has an unknown number of emission sites, and therefore unpredictable field emission properties. Samples subjected to stability testing showed a general decreasing trend in current with time and had percentage of standard deviation between 0.17% and 12.3% for completed runs.

## **Chapter V: Conclusions and Recommendations**

The research presented in this thesis was completed to investigate the field emission effects of carbon nanostructures (CNTs) pillars grown by surface decomposition on a patterned silicon carbide substrate. A conclusion about the overall results as well as possible future research is presented in this chapter.

### **5.1. Thesis Summary**

The objective of this research was to pattern a SiC substrate to create pillars for CNT growth and then measure the patterned CNT's field emission characteristics. The collected data from different samples were first compared to each other then compared to values found in literature. The uniqueness of this research however limited sample comparison of pillared structures in literature to only samples grown by catalyst enhanced CVD methods. After some of the samples were tested, they were subjected to constant voltage hold to determine their current stability.

The results from the SiC processing and patterning process confirmed that patterning SiC is a difficult process. Since normal semiconductor wet etching techniques are ineffective on SiC, the sample had to be reactive-ion-etched (RIE). To prevent the entire surface from being etched, a method had to be developed to mask the surface. The surface masking was complete by depositing a thin 220 nm layer of nickel on the SiC, followed by a photoresist layer. The photoresist was then patterned using photolithography. Once the photoresist layer was exposed and developed, the exposed nickel was etched to create a pattern to mask the SiC. The final steps used to pattern the SiC involve placing the sample in an RIE using a gaseous mixture of carbon-tetrafluoride

(CF<sub>4</sub>) and oxygen (O<sub>2</sub>) for preset amount of time followed by a final nickel etch to remove the nickel mask. The resulting pillar ranged in height from 1.25 μm and 2 μm.

CNT growth was conducted using thermal decomposition in an OXY-GON Furnace (Epsom, NH) located at AFRL/RX. The thermal decomposition method developed by Kusunoki [17] grows CNTs without the use of a catalyst found in other growth method. The CNT grown in this research effort were grown at 1700 °C for 3 – 4.5 hours for Si-face samples and 1 hour for C-face samples. The growth rates were consistent with research published by Mitchel *et al* using the same chamber with CNT layer heights were 280 - 300 nm and 640 nm for 3 and 4.5 hour growths on the Si-face and 270-280 nm for 1 hour growths on the C-face [19]. CNTs are found to grow throughout the entire surface, including on the sides of the pillars and the etched surface.

After CNT growth, the samples were subjected to field emission testing using an vacuum apparatus at AFIT. All sample tests exhibited some sort of electron emission. By utilizing F-N plots it was confirmed, with exception of one or two samples, that the electron emission exhibit field emission characteristics. Common themes from the data, was decrease in the turn-on field  $E_{TO}$  (taken at 1 μA/cm<sup>2</sup>) and an increase in the field enhancement factor  $\beta$ . The lowest measured value for  $E_{TO}$  was 2.5 V/μm and the highest  $\beta$  was 8007. These values are consistent with literature values but generally higher. These however came from the same sample. A direct comparison was also made between a patterned sample, an unpatterned sample, and an all etched surface sample. This comparison gave both expected and unexpected results. The comparison showed that a patterned sample can outperform an unpatterned sample where the patterned sample had an  $E_{TO}$  of 4.4 V/μm and  $\beta$  of 2199, while the unpatterned sample had a  $E_{TO}$  of

5.6 V/ $\mu\text{m}$  and  $\beta$  of 1490. In contrast, a patterned sample from the same set had an  $E_{\text{TO}}$  of 5.93 V/ $\mu\text{m}$  and  $\beta$  of 1190.

The decrease in  $E_{\text{TO}}$  and increase in  $\beta$  of the sample can be attributed to conditioning of the emitter surface as run progressed. The conditioning of the surface removes adsorbents and amorphous carbon from the emitter surface improving the overall emission quality. The result showed that nearly 66% of the time emission characteristics improved with each run. Conversely, in other case the sample stop emitting or become unstable as the applied field was increased. This can be attributed to microarcing with can cause significant damage to the CNT films [53]. This microarcing may be the reason for the decrease in current density over time during current stability testing.

## **5.2. Recommendation for Further Work**

This iteration of field emission from CNT grown SiC by thermal decomposition shows that it is possible to pattern a structure on SiC and produce field emission. The method of CNT growth does not require a catalyst which means it does not require post processing to remove impurities. However, the temperatures required to grow the CNTs is a limiting factor. To create any other structure, like an integrated diode or triode, would require either material of similar thermal characteristics of SiC, or post-processing of the structure. These structures could be further explored through the use of flip-chip bonding.

Further testing needs to be accomplished with different pillar parameters including: diameter, height, spacing and shape. These tests could include growing the CNTs the entire length of the pillar. Further iteration of the photolithography and

masking techniques also need to be explored to create more refined and consistent structure. Since no post processing was completed on the patterned CNT prior to field emission this should be also be explored. Field emission should also be explored using scanning anode field emission microscopy.

Finally, since one use for field emission is as a source for HPM system, a program should be explored to integrate CNT field emission research at AFIT with HPM source research at AFRL/RD or other HPM research sites.

## Appendices

### Appendix A: CNT Synthesis Processes

Carbon nanotube fabrication development has evolved into three different categories since Iijima's discovery in 1991: arc discharge synthesis, laser ablation synthesis, thermal synthesis.

#### A.1 Arc Discharge

Because arc discharge synthesis was the method used by Iijima's fullerenes work and subsequent CNT discovery, much of the early CNT growth is documented using this method and was the first method used to reliably produce both MWCNTs and SWCNTs [54]. CNT synthesis using this method is accomplished by igniting a plasma between two graphite electrodes in a low pressure (100 to 1000 torr) inert atmosphere (using He or Ar) [55] using a low voltage, high current power supply, as shown in Figure 124. The plasma contains vaporized carbon from the electrodes which then forms carbon nanotubes as it is deposited on the cathode and other areas of the reactor. The production of CNTs by arc discharge relies on the evaporation of a graphite target to create gas-phase carbon fragments that recombine to form the CNTs[10]. To form SWCNTs using arc-discharge, a metal catalyst must be added to the system. Early catalysts include iron (Fe) and cobalt (Co); however, recent techniques are now producing SWCNTs, with diameters of 1.2 to 1.4 nm and yields around 90%, using a mixture of yttrium (Y) and nickel (Ni) [55]. Synthesis using arc discharge includes a product that contains significant amounts of other graphitic and amorphous material that must be cleaned away before the CNTs can be used. Once the CNTs have been cleaned, they must then be

suspended in a solvent and deposited onto the intended surface by spraying, dipping, or spin-coating.

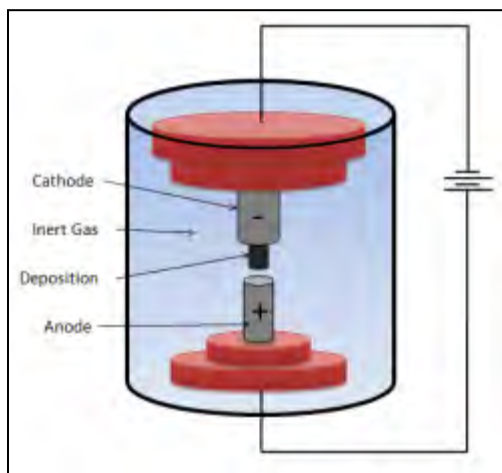


**Figure 124 – Arc Discharge Chamber [55]**

## **A.2 Laser Ablation**

The product of laser ablation is similar to arc discharge, both produce MWCNTs when a pure graphite target or anode is used and both produce SWCNTs when the proper metal catalyst is present [56]. During synthesis, laser ablation uses a continuous-wave (CW) or pulsed-wave (PW) laser to vaporize a graphite or catalyst metal infused composite graphite target in a quartz furnace at 1200° C with a constant flow of inert gas (He or Ar) . The inert gas flow moves the vaporized graphite nanoparticles and metal catalyst through the tube collecting them on a cooled copper condenser, as shown in Figure 125, where the cooled graphite nanoparticles synthesize into CNTs. Laser ablation produces SWCNTs with diameters between 1.0 – 1.6 nm [55]. Like arc-discharge, laser ablation synthesis contains the presence of graphitic and amorphous material which requires purification and suspension in solvent prior before application.

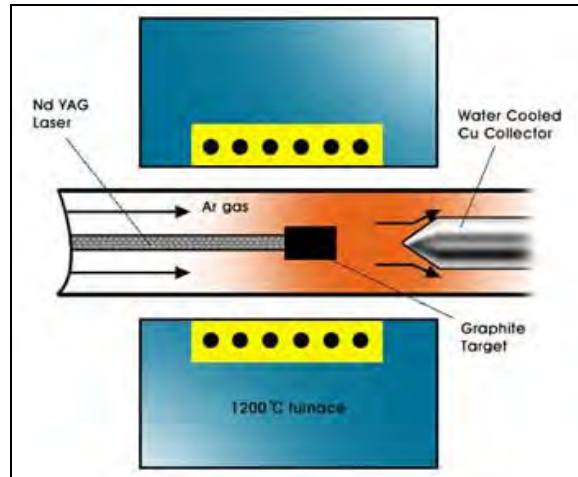


**Figure 125 – Laser Ablation Process [55]**

### **A.3 Thermal synthesis**

Thermal synthesis is a broad category of synthesis methods that rely on thermal energy to produce CNTs. Included in this category is plasma enhanced chemical vapor deposition (PE-CVD), which is a hybrid of plasma based and thermal based synthesis, and SiC surface decomposition which, though a true thermal process, is not often included in discussions of thermal synthesis methods. Due to the wide variety of options and precise control offered by thermal synthesis, chemical vapor deposition methods have received the most attention from researchers and yielded promising results for controlled CNT fabrication.

CVD as a synthesis method has variations including thermal CVD (T-CVD) and plasma-enhanced CVD (PECVD). All CVD methods require a metal catalytic nanoparticle to facilitate the growth of CNTs with Fe, Co, and Ni being the most common. Other catalyst, including yttrium (Y), molybdenum (Mo), ruthenium (Ru), and platinum (Pt), have been used in the synthesis of CNTs [55]. The general CVD process,

shown in Figure 126, involves small metal catalyst structures in the gas phase or on the surfaces to decompose a carbon containing gas [55].

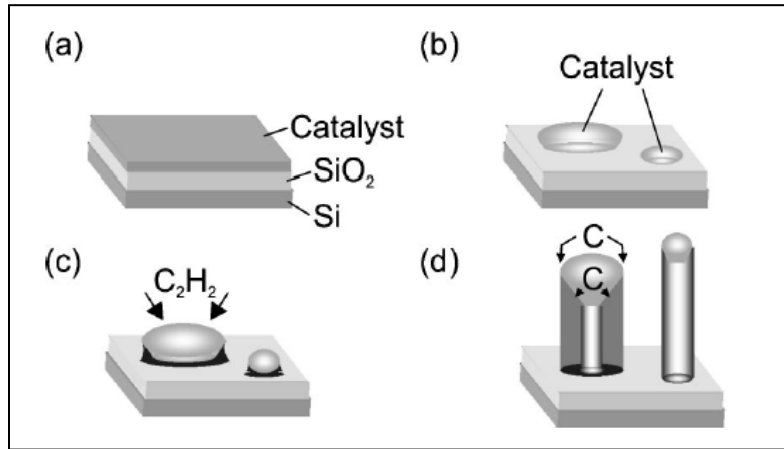


**Figure 126 – CVD CNT Growth with Catalyst [57]**

The carbon is dissolved or absorbed by the catalyst particle and released in the form a nanotube. The nanotube formation starts with a buckyball cap and continues to grow as long as carbon is delivered at specified rate and the catalyst does not change. An advantage to CVD is the ability to structure the catalyst particles and effectively pattern the nanotube growth. Control of the diameter, length, and density of CNTs can be controlled by the initial size of the catalyst, as demonstrated in Figure 127 and Figure 128 [57]. Using CVD, the growth of patterned MWCNT with uniform length and diameter has been demonstrated on a 6-inch wafer [10].

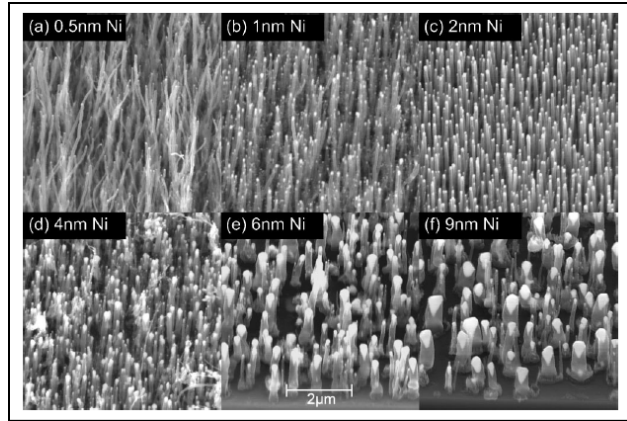


**Figure 127 – CVD Grown CNT with Varied Catalyst Thickness [57]**

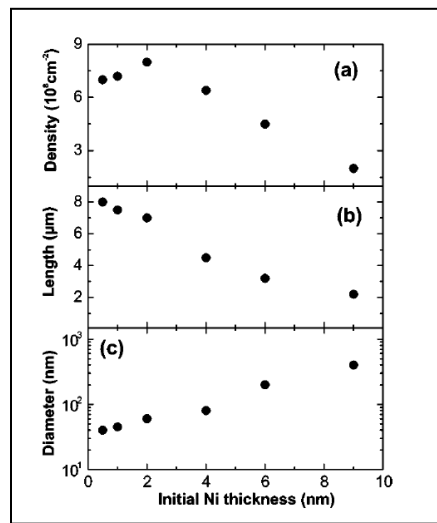


**Figure 128 – CNT Density, Length, Diameter Catalyst Dependence [57]**

A typical thermal CVD system, shown in Figure 129, consists of a furnace, feedstock gasses, and a vacuum pump. Depending on the process T-CVDs operate at a range from 500 (deg) C to 1200 (deg) C. As with the catalyst thickness, the deposition temperature also effects CNT growth [57]. The substrate is annealed in a non-volatile gas to form the catalytic nanoparticles and then placed in the furnace. A carbon feedstock gas, methane ( $\text{CH}_4$ ) or carbon monoxide ( $\text{CO}$ ) for SWCNTs, or acetylene ( $\text{C}_2\text{H}_2$ ), ethylene ( $\text{C}_2\text{H}_4$ ), or benzene ( $\text{C}_6\text{H}_6$ ) for MWCNTs is flowed across the substrate reacting with the catalytic nanoparticles to synthesize CNTs [58].

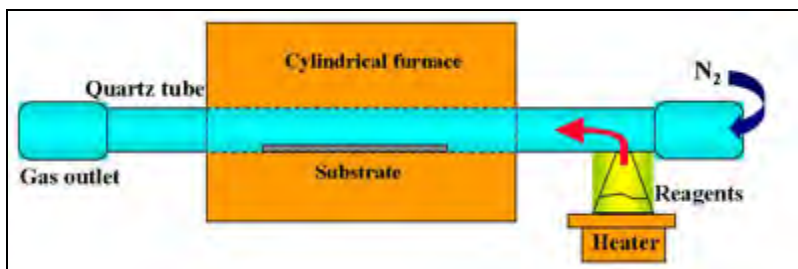


**Figure 129 – Thermal CVD Furnace [58]**

CVD synthesis occurs at relatively low temperatures that allow conventional substrates, such as silicon, to be used, and allow for integration of CNTs with conventional electronics, optoelectronics, and other applications. With the proper growth conditions, pure CNTs can be produced with yield rates as high as 99% [55]. Thus no purification or post processing is necessary unless the catalyst metal must be removed. As a result thermal CVD and its many derivatives are the most widely used and researched carbon nanotube synthesis methods.

Another method of CVD is PE-CVD. PE-CVD uses a DC, radio frequency (RF), or microwave power supply to generate a  $H_2$  plasma, as shown in Figure 130. The plasma breaks down the carbon feedstock gas and facilitates CNT growth at lower temperatures and pressures compared to T-CVD with substrate temperatures ranging from  $400^\circ C$  to  $900^\circ C$  [55].

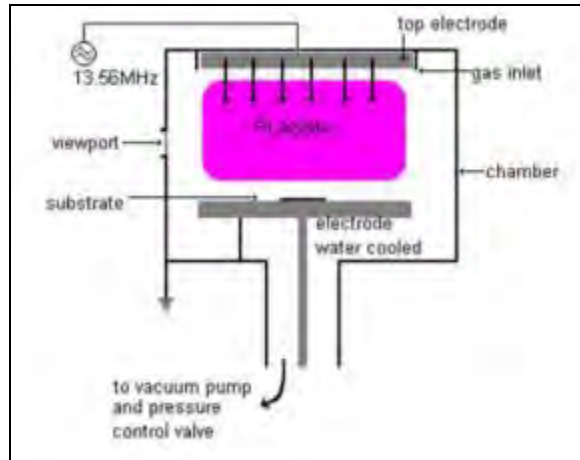


**Figure 130 – PE-CVD Chamber.**

PE-CVD synthesis is capable of growing patterned, vertically aligned SWCNTs and MWCNTs on different substrate materials. Remote PE-CVD, which uses a low power plasma away from the substrate, can produce higher percentage of a particular CNT chirality [55].

## Appendix B: Silicon Carbide Structure

Silicon carbide is the only stable compound found in the carbide system [49]. During formation, silicon carbide crystallizes into different polytypes from packed Si-C tetrahedrons. The tetrahedral structures consist of a carbon atom surrounded by four silicon atoms, and each silicon atom surrounded by four carbon atoms. The Si-C crystal consists of the elementary tetrahedral that are aligned such that all the atoms lie in parallel planes on the nodes of the hexagonal network [49]. The difference of the Si-C polytypes comes from stacking order of the elementary tetrahedra. The stacking sequence of three common polytypes is found in Figure 131.

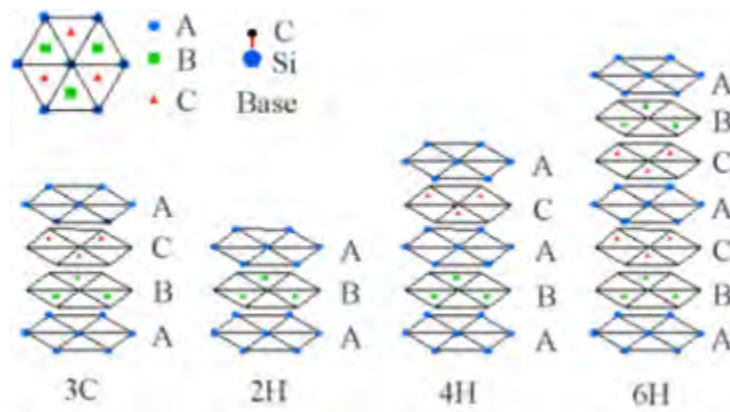


**Figure 131 – Planar view of stacking sequence of SiC**

This sequence starts with a double layer called the A position. Following a closed packed structure, the next layers are either the B or the C position. All Si-C polytypes are constructed by alternating the A, B, and C layers. Figure 132 shows alternative views of the stacking sequence [49].

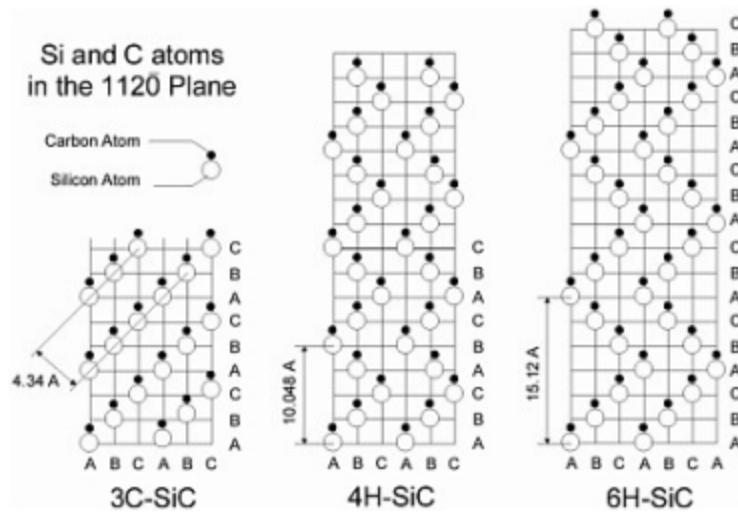


**Figure 132 – Stacking sequence of 3C, 4H, and 6H SiC [49]**

The layer sequence of the Si-C crystal can be determined from using the bottom lettering in Figure 132. For example, 3C-SiC has a sequence of ABC, 4H has a sequence of ABCB, and 6H has a sequence of ABCACB. Silicon carbide wafers are usually produced using a bulk manufacturing process or epitaxial growth [49].

**Table 26 – Summary of RIE on SiC polytypes [50]**

polytypes etched	source gas(es)	process type	typical process conditions: pressure, power, dc bias, flow rates	etch rate (Å/min)
3C	CF <sub>4</sub> /O <sub>2</sub>	plasma/RIE (rf)	180 to 200 mT, 0.8 W/cm <sup>2</sup> , 67% O <sub>2</sub> , 33% CF <sub>4</sub>	60 to 260
4H, 6H	SF <sub>6</sub>	RIE (rf)	20 mT, 250 W, -220 to -250 V, 20 sccm 35 sccm	490, 420 570, 530
6H	SF <sub>6</sub> /O <sub>2</sub> NF <sub>3</sub> /O <sub>2</sub>	RIE (rf)	20 mT, 200 W, -220 to -250 V, SF <sub>6</sub> : O <sub>2</sub> = 18 : 2 (sccm) NF <sub>3</sub> : O <sub>2</sub> = 18 : 2 (sccm)	450 570
6H	SF <sub>6</sub> /O <sub>2</sub>	RIE (rf)	50 mT, 200 W, -250 V, SF <sub>6</sub> : O <sub>2</sub> = 5 : 5 (sccm)	360
6H	SF <sub>6</sub> /O <sub>2</sub> , CF <sub>4</sub> /O <sub>2</sub> with N <sub>2</sub> additive	RIE (rf)	190 mT, 300 W, CF <sub>4</sub> : O <sub>2</sub> : N <sub>2</sub> = 40 : 15 : 10 (sccm) SF <sub>6</sub> : O <sub>2</sub> : N <sub>2</sub> = 40 : 2 : 0 (sccm)	2200 3000
4H, 6H	NF <sub>3</sub>	RIE (rf)	20 mT, 250 W, -220 to -250 V, 20 sccm 35 sccm	565, 540 630
4H, 6H	NF <sub>3</sub>	RIE (rf)	225 mT, 275 W, -25 to -50 V, 95 to 110 sccm	1500
6H	Cl <sub>2</sub> /SiCl <sub>4</sub> /O <sub>2</sub> and Ar/N <sub>2</sub>	RIE (rf)	190 mT, 300 W, Cl <sub>2</sub> : SiCl <sub>4</sub> : O <sub>2</sub> : N <sub>2</sub> = 40 : 20 : 8 : 10 (sccm) Cl <sub>2</sub> : SiCl <sub>4</sub> : O <sub>2</sub> : Ar = 40 : 20 : 0 : 10 (sccm)	1600 1900
3C, 6H	SF <sub>6</sub> /O <sub>2</sub>	ECR (μwave)	1 mT, 1200 W, -20 to -110 V SF <sub>6</sub> : O <sub>2</sub> = 4 : 0 to 8 (sccm) SF <sub>6</sub> : O <sub>2</sub> = 4 : 0 to 6 (sccm)	1000 to 2700
4H, 6H	CF <sub>4</sub> /O <sub>2</sub>	ECR (μwave)	1 mT, 650 W, -100 V, CF <sub>4</sub> : O <sub>2</sub> = 41.5 : 8.5 (sccm)	700

## Appendix C: SiC Decomposition Procedure

SiC Decomposition Procedure: The following steps are performed using AFRL/RXPS's Oxy-Gon graphite resistance heating furnace to decompose the SiC samples to form CNTs (courtesy of Dr. John Boeckl, AFRL/RXPS).

System Start-up (process selection switch in STANDBY):

1. Turn ON the 80 psi house air (the vent and vacuum valves are air pressure activated).
2. Turn ON the Main Power switch (the handle is on the lower front of the main panel).
3. Turn the Roughing Pump ON (green button). The Roughing Pump will pull on the turbo-molecular pump – to  $\sim 10^{-3}$  Torr on TC1 (this will take  $\sim 15$  minutes).
4. Turn ON the ion gauge controller to read TC1 (it is the left switch on the gauge panel).
5. Turn the turbo-molecular pump ON (green button); it will pull on itself.
6. If the chamber is under vacuum, turn the process selection switch to VENT GAS, otherwise go to step 8.
7. Turn ON the low-O<sub>2</sub>, N<sub>2</sub>, or Ar at the tank and regulator; open the ball valve on the furnace to 25 (this step vents the chamber, allowing it to open).
8. When the chamber vents, turn OFF the low-O<sub>2</sub>, N<sub>2</sub>, or Ar ball valve, tank, and regulator.
9. OPEN the chamber, load the samples on the graphite cylinder, and SECURE the chamber door.

Chamber Evacuation Process:

10. Turn the process selection switch to STANDBY; then to ROUGH.
  11. Run the roughing pump until chamber is in the mid  $10^{-2}$  Torr range (read TC2); this will take several minutes, and the pressure will slightly increase at TC1 ( $\sim 15$  minutes).
  12. Turn process selection switch to HI VACUUM (turbo-molecular pump will pull on the chamber, roughing pump pulls on the turbo-molecular pump; TC2 will drop quickly; TC1 increases, then drops more slowly).
  13. Turn ON the ion gauge filament when TC2 is in the  $10^{-3}$  Torr range. Continue pumping until it is in the  $\sim 1 \times 10^{-4}$  Torr range (note: ion gauge will not light if the pressure is too high).
  14. OPEN the H<sub>2</sub>O outlet and inlet hand valves (note: do this only if the chamber is under vacuum or filled with an inert gas).
  15. Ensure the yellow H<sub>2</sub>O handles are open and that the flow meters are turning.
- Nanocap Formation Process (if desired else skip to step 19)
16. Ramp up AUTO/MAN power controller to obtain 1250°C (set A to 32%; then adjust A when  $\sim 1225$ °C).
  17. Decompose samples for 30 minutes (adjust AUTO/MAN controller as needed).

Decomposition Process:

19. Ramp up AUTO/MAN power controller to obtain target temperature (set A to 39%; then adjust A when  $\sim 25$ °C below target value).
20. Decompose the sample for desired time (adjust AUTO/MAN controller as needed).

21. At the desired time, ramp down AUTO/MAN controller to 1%.
22. After 5 minutes into ramp down, set AUTO/MAN controller to 0%, and turn OFF the Heat Zone
23. When the temperature is  $\leq 150^{\circ}\text{C}$ , CLOSE the H<sub>2</sub>O inlet and outlet hand valves.  
(note: chamber cools quicker with H<sub>2</sub>O)
24. Turn OFF the ion gauge filament (same switch used to turn it on).
25. Turn ON the low-O<sub>2</sub>, N<sub>2</sub>, or Ar at tank and regulator; open the ball valve on the furnace to 25.
26. Turn the process selection switch to VENT GAS to backfill the chamber.
27. When the chamber temperature is  $\sim 30^{\circ}\text{C}$ , CLOSE the low-O<sub>2</sub>, N<sub>2</sub>, or Ar at the tank and regulator; OPEN the chamber; UNLOAD the samples; SECURE the chamber door.
28. If additional runs will be completed in the same day, load the new sample and return to step 10.

System Shutdown:

30. Turn process selection switch to STANDBY; then to ROUGH.
31. Turn ON the ion gauge controller to read TCs.
32. Run the roughing pump until TC2 reads approximately  $10^{-2}$  Torr, then turn the process selection switch to HI VACUUM until TC2 reads approximately  $10^{-3}$  Torr.
33. Turn the process selection switch to STANDBY; turn OFF the turbo-molecular pump.
34. Turn OFF the vacuum interlock bypass.
35. Turn OFF the roughing pump.

## Appendix D: Field Emission Chamber Procedures

SiC Decomposition Procedure: The following steps are performed using AFIT vacuum chamber (courtesy of Maj Nathan Glauvitz, AFIT).

The chamber is nominally left under high vacuum when samples are not being tested to maintain a clean environment in the chamber.

### 1. Day-to-day configuration for each pump, valve, and electronics while the entire chamber is under high vacuum:

Sample exchange rough pump: ON

Sample exchange turbo pump: ON

Chamber rough pump: ON

Chamber turbo pump: ON

**Caution: Never have the sample exchange roughing valve and sample exchange rough backing valve open at the same time.**

Sample exchange roughing valve: CLOSED

Sample exchange rough backing valve: OPEN

Sample exchange Turbo pump gate valve: OPEN

Sample exchange chamber gate valve: OPEN

Chamber rough backing valve: OPEN

Chamber Turbo pump gate valve: OPEN

Ion gauges: OFF

Power supplies & voltmeters: OFF

### 2. Loading or Unloading a sample when the chamber is under high vacuum:

- Ensure sample holder rod is retracted into the sample exchange chamber
- Close sample exchange chamber gate valve
- Close sample exchange Turbo pump gate valve
  - Sample exchange rough backing valve can be left open
- Sample exchange roughing valve should remain closed
  - Sample exchange chamber should now be completely isolated
- Open green N2 knob to bleed N2 into the sample exchange chamber
  - Once the lid has opened, reduce N2 to a trickle
- Remove carrier with small hex tool, load specimen into the carrier, then reinstall carrier onto extending rod
- Close lid
- Close green N2 knob completely
  
- Close sample exchange rough backing valve
- Open sample exchange roughing valve to rough down the chamber
- When vacuum gauge for the sample exchange chamber goes to  $1 \times 10^{-3}$ , the chamber is completely roughed down
- Close sample exchange roughing valve

- Open sample exchange rough backing valve and allow to pump for a minute or so
- Then open sample exchange Turbo pump gate valve
- Turn on both ion gauges
- When the sample exchange chamber pressure is on the same order of magnitude (~30 min) as the main chamber, open the sample exchange chamber gate valve
- Extend rod so carrier is seated into carrier holder

### **3. Shutting down the chamber for a power outage or maintenance:**

- Ensure ion gauges and power supplies are off
- Close sample exchange chamber gate valve
- Close sample exchange Turbo pump gate valve
- Close chamber Turbo pump gate valve
- Close sample exchange roughing valve (if not closed already)
- Unplug sample exchange Turbo pump
- Unplug chamber Turbo pump
- Close sample exchange rough backing valve
- Close chamber rough backing valve
- Turn switch off on the sample exchange rough pump
- Turn switch off on the chamber rough pump

### **4. Chamber start-up if all pumps are off and the chamber is atmospheric pressure:**

- Open sample exchange chamber gate valve
- Close sample exchange Turbo pump gate valve
- Close chamber Turbo pump gate valve
- Close sample exchange rough backing valve
- Close chamber rough backing valve
- Close sample exchange roughing valve
- Turn on the sample exchange rough pump
- Turn on the chamber rough pump
- Wait here until rough pumps have been on for a few minutes
- Plug in chamber Turbo pump
- Open sample exchange roughing valve
  - Allow to pump entire chamber down until pressure reads  $1 \times 10^{-3}$  (~10-30 minutes)
- Close sample exchange roughing valve
- Open sample exchange rough backing valve
- Open chamber Turbo pump gate valve
- ~5 minutes after the sample exchange rough backing valve was opened, plug in sample exchange Turbo pump
- After additional ~5 minutes for the turbo to get up to speed
  - Open the sample exchange Turbo pump gate valve
- Allow chamber to pump down over night before testing any samples.

## References

- [1] E. Schamiloglu. High power microwave sources: Where do we go from here? Presented at Power Modulator Symposium, 2002 and 2002 High-Voltage Workshop. Conference Record of the Twenty-Fifth International. 2002.
- [2] D. Shiffler, M. Haworth, K. Cartwright, R. Umstattd, M. Ruebush, S. Heidger, M. LaCour, K. Golby, D. Sullivan, P. Duselis and J. Luginsland. "Review of Cold Cathode Research at the Air Force Research Laboratory". *IEEE Trans. Plasma Sci.*, (3), 2008.
- [3] Liu Lie, Wan Hong, Zhang Jun, Wen Jian-Chun, Zhang Ya-Zhou and Liu Yong-Gui. "Fabrication of Carbon-Fiber Cathode for High-Power Microwave Applications". *Plasma Science, IEEE Transactions on*, (4), 2004.
- [4] R. B. Miller. "Mechanism of Explosive Electron Emission for Dielectric Fiber (Velvet) Cathodes". *J. Appl. Phys.*, (7), 1998.
- [5] R. J. Ulmstadd, "Advanced Electron-Beam Sources," in *Modern Microwave and Millimeter-Wave Power Electronics*, 1st ed., Barker R. J., J. H. Booske, N. C. Luhmann Jr and G. S. Nusinovich, Eds. Piscataway, NJ: IEEE Nuclear and Plasma Sciences Society, 2005, pp. 393.
- [6] K. L. Jensen and M. Cahay. "General Thermal-Field Emission Equation". *Appl. Phys. Lett.*, (15), 2006.
- [7] R. H. Fowler and L. Nordheim. "Electron Emission in Intense Electric Fields". *Proc. R. Soc. A*, (781), 1928.
- [8] T. Utsumi. "Vacuum Microelectronics: What's New and Exciting". *IEEE Trans. Electron Devices*, (10), 1991.
- [9] S. Iijima. "Helical Microtubules of Graphitic Carbon". *Nature*, (6348), 1991.
- [10] Graham A.P., G. S. Duesberg, W. Hoenlein, Kreupl F., M. Liebau, R. Martin, Rajasekharan B., W. Pamler, R. Seidel and W. Steinhoegl, "How do Carbon Nanotubes Fit into the Semiconductor Roadmap?". *Appl Phys Mater Sci Process*, vol. 80, pp. 1141-1151, 2005.
- [11] N. S. Xu and S. E. Huq. "Novel Cold Cathode Materials and Applications". *Mater. Sci. Eng. , C*, (2), 2005.

- [12] G. Chen, W. Wang, J. Peng, C. He, S. Deng, N. Xu and Z. Li. "Screening Effects on Field Emission from Arrays of (5,5) Carbon Nanotubes: Quantum Mechanical Simulations". *Phys. Rev. B*, (19), 2007.
- [13] M. Zidour, K. H. Benrahou, A. Semmah, M. Naceri, H. A. Belhadj, K. Bakhti and A. Tounsi. "The Thermal Effect on Vibration of Zigzag Single Walled Carbon Nanotubes using Nonlocal Timoshenko Beam Theory". *Comput. Mater. Sci.*, (1), 2012.
- [14] S. Rai, "Carbon Nanotubes (www.nd.edu/~gsnider/EE698A/shishir-rai-carbonnanotubes.ppt)".
- [15] M. S. Dresselhaus, G. Dresselhaus, J. C. Charlier and E. Hernández. "Electronic, Thermal and Mechanical Properties of Carbon Nanotubes". *Phil. Trans. R. Soc. A*, (1823), 2004.
- [16] L. Chico, V. H. Crespi, L. X. Benedict, S. G. Louie and M. L. Cohen. "Pure Carbon Nanoscale Devices: Nanotube Heterojunctions". *Phys. Rev. Lett.*, (6), 1996.
- [17] M. Kusunoki, J. Shibata, M. Rokkaku and T. Hirayama, "Aligned Carbon Nanotube Film Self-Organized on a SiC Wafer". *Jpn. J. Appl. Phys.* 2, vol. 37, pp. L605-L606, 15 May 1998, 1998.
- [18] M. Kusunoki, T. Suzuki, T. Hirayama, N. Shibata and K. Kaneko. "A Formation Mechanism of Carbon Nanotube Films on SiC(0001)". *Appl. Phys. Lett.*, (4), 2000.
- [19] W. C. Mitchel, J. Boeckl, D. Tomlin, W. Lu, J. Rigueur and J. Reynolds. Growth of carbon nanotubes by sublimation of silicon carbide substrates. Presented at Proceedings of SPIE. 2005.
- [20] Z. G. Cambaz, G. Yushin, S. Osswald, V. Mochalin and Y. Gogotsi. "Noncatalytic Synthesis of Carbon Nanotubes, Graphene and Graphite on SiC". *Carbon*, (6), 2008.
- [21] M. Kusunoki, C. Honjo, T. Suzuki and T. Hirayama. "Growth Process of Close-Packed Aligned Carbon Nanotubes on SiC". *Appl. Phys. Lett.*, (10), 2005.
- [22] T. Maruyama and S. Naritsuka, "Initial Growth Process of Carbon Nanotubes in Surface Decomposition of SiC," in *Carbon Nanotubes - Synthesis, Characterization, Applications*, S. Yellampalli, Ed. InTech, 2011, pp. 29-47.

- [23] H. Watanabe, Y. Hisada, S. Mukainakano and N. Tanaka. "In Situ Observation of the Initial Growth Process of Carbon Nanotubes by Time-Resolved High Resolution Transmission Electron Microscopy". *J. Microsc.*, (1), 2001.
- [24] M. Kusunoki, T. Suzuki, C. Honjo, H. Usami and H. and Kato, "Closed-Packed and Well-Aligned Carbon Nanotube Films on SiC," *J. Phys. D*, vol. 40, pp. 6278, 2007.
- [25] H. Bang, Y. Ito, Y. Kawamura, E. Hosoda, C. Yoshida, T. Maruyama, S. Naritsuka and M. Kusunoki. "Observation of Nanosized Cap Structures on 6H-SiC Substrates by Ultrahigh-Vacuum Scanning Tunneling Microscopy". *Jpn. J. Appl. Phys.*, (1A), 2006.
- [26] T Yamauchi and T Ueda and M Naitoh and S Nishigaki and M.Kusunoki. "Influence of Heating Rate upon the Growth of Carbon Nanotubes by the SiC Surface Decomposition Method". *J. Phys. Conf. Ser.*, (8), 2008.
- [27] Y. Song and F. W. Smith. "Phase Diagram for the Interaction of Oxygen with SiC". *Appl. Phys. Lett.*, (16), 2002.
- [28] R. G. Forbes. "Use of Energy-Space Diagrams in Free-Electron Models of Field Electron Emission". *Surf. Interface Anal.*, (5-6), 2004.
- [29] R. G. Forbes and J. H. B. Deane. "Reformulation of the Standard Theory of Fowler-Nordheim Tunnelling and Cold Field Electron Emission". *Proc. R. Soc. A*, (2087), 2007.
- [30] R. G. Forbes. "Physics of Generalized Fowler-Nordheim-Type Equations". *J. Vac. Sci. Technol. B*, (2), 2008.
- [31] E. L. Murphy and R. H. Good Jr. "Thermionic Emission, Field Emission, and the Transition Region". *Phys. Rev.*, (6), 1956.
- [32] R. D. Young. "Theoretical Total-Energy Distribution of Field-Emitted Electrons". *Phys. Rev.*, (1), 1959.
- [33] R. D. Young and E. W. Müller. "Experimental Measurement of the Total-Energy Distribution of Field-Emitted Electrons". *Phys. Rev.*, (1), 1959.
- [34] G. N. Fursey. "Field Emission in Vacuum Micro-Electronics". *Appl. Surf. Sci.*, 2003.

- [35] N. de Jonge. "Brightness of Carbon Nanotube Electron Sources". *J. Appl. Phys.*, (2), 2004.
- [36] A. V. Eletsii. "Carbon Nanotube-Based Electron Field Emitters". *Phys. -Usp.*, (9), 2010.
- [37] A. V. Eletsii and G. S. Bocharov. "Emission Properties of Carbon Nanotubes and Cathodes on their Basis". *Plasma Sources Sci. T.*, (3), 2009.
- [38] G. N. Fursey and D. V. Glazanov. "Deviations from the Fowler--Nordheim Theory and Peculiarities of Field Electron Emission from Small-Scale Objects". *J. Vac. Sci. Technol. B*, (2), 1998.
- [39] R. G. Forbes, C. J. Edgcombe and U. Valdrè. "Some Comments on Models for Field Enhancement". *Ultramicroscopy*, (0), 2003.
- [40] K. B. K. Teo, R. G. Lacerda, M. H. Yang, A. S. Teh, L. A. W. Robinson, S. H. Dalal, N. L. Rupesinghe, M. Chhowalla, S. B. Lee, D. A. Jefferson, D. G. Hasko, G. A. J. Amaratunga, W. L. Milne, P. Legagneux, L. Gangloff, E. Minoux, J. P. Schnell and D. Pribat. "Carbon Nanotube Technology for Solid State and Vacuum Electronics". *IEE Proc Circ Dev Syst*, (5), 2004.
- [41] W. A. de Heer, "Nanotubes and the Pursuit of Applications". *MRS Bulletin*, vol. 29, pp. 281-285, 2004.
- [42] J. Bonard, J. Salvétat, T. Stockli, W. A. de Heer, L. Forro and A. Chatelain. "Field Emission from Single-Wall Carbon Nanotube Films". *Appl. Phys. Lett.*, (7), 1998.
- [43] J. Bonard, F. Maier, T. Stöckli, A. Châtelain, W. A. de Heer, J. Salvétat and L. Forró. "Field Emission Properties of Multiwalled Carbon Nanotubes". *Ultramicroscopy*, (1-4), 1998.
- [44] L. Nilsson, O. Groening, C. Emmenegger, O. Kuettel, E. Schaller, L. Schlapbach, H. Kind, J. Bonard and K. Kern. "Scanning Field Emission from Patterned Carbon Nanotube Films". *Appl. Phys. Lett.*, (15), 2000.
- [45] J. S. Suh and J. S. Lee. "Highly Ordered Two-Dimensional Carbon Nanotube Arrays". *Appl. Phys. Lett.*, (14), 1999.
- [46] R. C. Smith and S. R. P. Silva. "Maximizing the Electron Field Emission Performance of Carbon Nanotube Arrays". *Appl. Phys. Lett.*, (13), 2009.

- [47] L. Tong, M. Mehregany and L. G. Matus, "Mechanical Properties of 3C Silicon Carbide," *Appl. Phys. Lett.*, vol. 60, pp. 2992-2994, 1992; 1992.
- [48] M. Mehregany, Lijun Tong, L. G. Matus and D. J. Larkin. "Internal Stress and Elastic Modulus Measurements on Micromachined 3C-SiC Thin Films". *IEEE T Electron Dev*, (1), 1997; 1997.
- [49] W. Wesch. "Silicon Carbide: Synthesis and Processing". *Nucl. Instrum. Methods Phys. Res. , Sect. B*, 1996.
- [50] P. H. Yih, V. Saxena and A. J. Steckl. "A Review of SiC Reactive Ion Etching in Fluorinated Plasmas". *Phys. Stat. Sol. B*, (1), 1997.
- [51] M. Kothandaraman, D. Alok and B. Baliga, "Reactive Ion Etching of Trenches in 6H-SiC," *J Electron Mater*, vol. 25, pp. 875-878, 1996.
- [52] M. C. Pochet, "Characterization of the Field Emission Properties of Carbon Nanotubes Formed on Silicon Carbide Substrates by Surface Decomposition," 2006.
- [53] X. H. Liang, S. Z. Deng, N. S. Xu, J. Chen, N. Y. Huang and J. C. She. "Noncatastrophic and Catastrophic Vacuum Breakdowns of Carbon Nanotube Film Under Direct Current Conditions". *J. Appl. Phys.*, (6), 2007.
- [54] B. Bhushan, Ed., *Springer Handbook of Nanotechnology*. New York: Springer, 2010.
- [55] M. O'Connell, *Carbon Nanotubes: Properties and Applications*. Boca Raton, FL: CRC Press, 2006.
- [56] T. Guo, P. Nikolaev, A. Thess, D. T. Colbert and R. E. Smalley. "Catalytic Growth of Single-Walled Nanotubes by Laser Vaporization". *Chemical Physics Letters*, (1-2), 1995.
- [57] M. Chhowalla, K. B. K. Teo, C. Ducati, N. L. Rupesinghe, G. A. J. Amaratunga, A. C. Ferrari, D. Roy, J. Robertson and W. I. Milne. "Growth Process Conditions of Vertically Aligned Carbon Nanotubes using Plasma Enhanced Chemical Vapor Deposition". *J. Appl. Phys.*, (10), 2001.
- [58] Geckeler K. E. and Rosenberg E., *Functional Nanomaterials*. June 20, 2006: American Scientific Publishers, 2006.

<b>REPORT DOCUMENTATION PAGE</b>			<i>Form Approved OMB No. 074-0188</i>		
<p>The public reporting burden for this collection of information is estimated to average 1 hour per response, including the time for reviewing instructions, searching existing data sources, gathering and maintaining the data needed, and completing and reviewing the collection of information. Send comments regarding this burden estimate or any other aspect of the collection of information, including suggestions for reducing this burden to Department of Defense, Washington Headquarters Services, Directorate for Information Operations and Reports (0704-0188), 1215 Jefferson Davis Highway, Suite 1204, Arlington, VA 22202-4302. Respondents should be aware that notwithstanding any other provision of law, no person shall be subject to a penalty for failing to comply with a collection of information if it does not display a currently valid OMB control number.</p> <p><b>PLEASE DO NOT RETURN YOUR FORM TO THE ABOVE ADDRESS.</b></p>					
<b>1. REPORT DATE</b> (DD-MM-YYYY) 22-03-2012		<b>2. REPORT TYPE</b> Master's Thesis		<b>3. DATES COVERED</b> (From - To) September 2010 - March 2012	
<b>TITLE AND SUBTITLE</b>  Field Emission of Thermally Grown Carbon Nanostructures on Silicon Carbide			<b>5a. CONTRACT NUMBER</b>		
			<b>5b. GRANT NUMBER</b>		
			<b>5c. PROGRAM ELEMENT NUMBER</b>		
<b>6. AUTHOR(S)</b>  Campbell, Jonathon M., Captain, USAF			<b>5d. PROJECT NUMBER</b> N/A		
			<b>5e. TASK NUMBER</b>		
			<b>5f. WORK UNIT NUMBER</b>		
<b>7. PERFORMING ORGANIZATION NAME(S) AND ADDRESS(S)</b> Air Force Institute of Technology Graduate School of Engineering and Management (AFIT/EN) 2950 Hobson Way, Building 640 WPAFB OH 45433-8865			<b>8. PERFORMING ORGANIZATION REPORT NUMBER</b>  AFIT/GE/ENG/12-06		
<b>9. SPONSORING/MONITORING AGENCY NAME(S) AND ADDRESS(ES)</b> Air Force Research Laboratory, Materials and Manufacturing Directorate Attn: Dr. John J. Boeckl 3005 Hobson Way, Bldg 651 WPAFB OH 45433-7707 DSN: 785-4474 x3219 john.boeckl@wpafb.af.mil			<b>10. SPONSOR/MONITOR'S ACRONYM(S)</b> AFRL/RXPS		
			<b>11. SPONSOR/MONITOR'S REPORT NUMBER(S)</b>		
<b>12. DISTRIBUTION/AVAILABILITY STATEMENT</b> APPROVED FOR PUBLIC RELEASE; DISTRIBUTION UNLIMITED.					
<b>13. SUPPLEMENTARY NOTES</b> This material is declared a work of the U.S. Government and is not subject to copyright protection in the United States.					
<b>14. ABSTRACT</b>  CNTs are known to be excellent field emitter due to their unique physical and electrical properties. Because of their semi-metallic nature, CNT do not suffer the thermal runaway found in metallic emitters, and their near one-dimension shape make them an ideal emission sources. CNTs growth by thermal decomposition of silicon carbide does not utilize a catalyst, therefore relatively defect free. One drawback to this method, however is that the CNT grow in a very dense carpet. This very dense CNT carpet comes under the affect of field emission screening effects which dampen the field emission. In this thesis, silicon carbide samples are patterned to create elevated emission sites in an attempt to minimize the field emission screening effect. Patterning is accomplished by using standard photolithography methods to implement a masking nickel layer on the silicon carbide. Pillars are created by etching the unmasked area of the silicon carbide in a reactive ion etcher. CNT growth is accomplished in a thermal furnace of varying times based on the selected face of the silicon carbide. Field emission testing to obtain turn-on voltage, field enhancement factor, and current densities is accomplished using a standard vacuum tube diode test configuration, while selected samples are subjected to stability testing over varying times. Although the samples tested did not conclusively demonstrate improved field emission characteristics when compared to values found in the literature for other bundled or pillared CNT, the data collected from similar samples in this work shows that a patterned CNT film can outperform a non-patterned film. From the measured CNT data, the lowest turn-on electric field is found to be 2.5 V/ $\mu\text{m}$ (taken at 1 $\mu\text{A}/\text{cm}^2$ ), and the highest field enhancement factor is of 8007. The variability in performance between samples can be attributed to differences in the emission surfaces as the result of: sample processing; the presence of impurities or amorphous carbon; and damage to the emitter surface due to microarcing.					
<b>15. SUBJECT TERMS</b> Field emission, carbon nanotubes, silicon carbide, surface decomposition					
<b>16. SECURITY CLASSIFICATION OF:</b>			<b>17. LIMITATION OF ABSTRACT</b>  UU	<b>18. NUMBER OF PAGES</b>  182	<b>19a. NAME OF RESPONSIBLE PERSON</b> Michael C. Pochet, Maj, USAF
<b>a. REPORT</b>  U	<b>b. ABSTRACT</b>  U	<b>c. THIS PAGE</b>  U			<b>19b. TELEPHONE NUMBER</b> (Include area code) (937) 785-3636, ext 4393 (michael.pochet@afit.edu)

Standard Form 298 (Rev. 8-98)  
Prescribed by ANSI Std. Z39-18